

# EuO and Gd-doped EuO thin films: epitaxial growth and properties

Inaugural - Dissertation  
zur  
Erlangung des Doktorgrades  
der Mathematisch-Naturwissenschaftlichen Fakultät  
der Universität zu Köln

vorgelegt von  
Ronny Sutarto  
aus Bandung, Indonesien

Köln 2009

Berichtstater:

Prof. Dr. L. H. Tjeng

Prof. Dr. C. M. Schneider

Tag der mündlichen Prüfung: 6. Juli 2009

# Contents

|          |   |           |
|----------|---|-----------|
| <b>1</b> | <b>Introduction</b>   | <b>1</b>  |
| 1.1      | Review of EuO and Gd-doped EuO properties . . . . .                     | 2         |
| 1.1.1    | EuO Growth . . . . .  | 3         |
| 1.1.2    | Magnetic properties . . . . .   | 5         |
| 1.1.3    | Transport properties . . . . .  | 10        |
| 1.1.4    | Optical properties . . . . .  | 11        |
| 1.1.5    | Electronic structure . . . . .  | 11        |
| 1.2      | Motivation and Scope . . . . .  | 12        |
| <b>2</b> | <b>Experimental methods</b>   | <b>15</b> |
| 2.1      | EuO thin film growth by means of molecular beam epitaxy (MBE) . . . . . | 15        |
| 2.1.1    | General considerations of MBE . . . . .                                 | 15        |
| 2.1.2    | Mini-MBE set-up . . . . .   | 19        |
| 2.1.3    | Substrate preparation . . . . .   | 20        |
| 2.1.4    | Fabrication of EuO thin film . . . . .                                  | 21        |
| 2.1.5    | Capping EuO thin film . . . . .   | 21        |
| 2.2      | <i>In-situ</i> characterization . . . . .                               | 22        |
| 2.2.1    | RHEED . . . . .   | 22        |
| 2.2.2    | LEED . . . . .  | 25        |
| 2.2.3    | XPS . . . . .   | 26        |
| 2.3      | <i>Ex-situ</i> characterization . . . . .                               | 27        |
| 2.3.1    | XAS . . . . .   | 27        |
| 2.3.2    | XRR . . . . .   | 29        |
| 2.3.3    | SQUID magnetometer . . . . .  | 29        |

---

|          |   |           |
|----------|---|-----------|
| <b>3</b> | <b>Initial stages of EuO growth on YSZ (001)</b>      | <b>31</b> |
| 3.1      | Introduction . . . . .                                | 31        |
| 3.2      | Experimental . . . . .                                | 32        |
| 3.3      | Results: RHEED and LEED . . . . .                     | 32        |
| 3.4      | Results: XPS . . . . .                                | 35        |
| 3.5      | Conclusions . . . . .                                 | 39        |
| <b>4</b> | <b>Sustained growth of EuO on YSZ (001)</b>           | <b>41</b> |
| 4.1      | Introduction . . . . .                                | 41        |
| 4.2      | Results: RHEED and LEED . . . . .                     | 41        |
| 4.3      | Results: thickness . . . . .                          | 44        |
| 4.4      | Results: magnetic properties . . . . .                | 46        |
| 4.5      | Results: XAS . . . . .                                | 47        |
| 4.6      | Conclusions . . . . .                                 | 48        |
| <b>5</b> | <b>Gd-doped EuO thin films on YSZ (001)</b>           | <b>49</b> |
| 5.1      | Introduction . . . . .                                | 49        |
| 5.2      | Experimental . . . . .                                | 50        |
| 5.3      | Results: RHEED and LEED . . . . .                     | 51        |
| 5.4      | Results: stoichiometry and Gd concentration . . . . . | 54        |
| 5.5      | Results: magnetic properties . . . . .                | 58        |
| 5.6      | Discussion . . . . .                                  | 61        |
| 5.7      | Conclusions . . . . .                                 | 65        |
| <b>6</b> | <b>SXMCD study on Gd-doped EuO thin films</b>         | <b>67</b> |
| 6.1      | Introduction . . . . .                                | 67        |
| 6.2      | Experimental . . . . .                                | 68        |
| 6.3      | Spin moments of Gd and Eu . . . . .                   | 68        |
| 6.4      | Conclusions . . . . .                                 | 70        |
| <b>7</b> | <b>Epitaxial growth of EuO on MgO</b>                 | <b>73</b> |
| 7.1      | Introduction . . . . .                                | 73        |
| 7.2      | Experimental . . . . .                                | 73        |
| 7.3      | Results . . . . .                                     | 74        |
| 7.4      | Conclusions . . . . .                                 | 76        |
|          | <b>Summary</b>  | <b>77</b> |
|          | <b>Zusammenfassung</b>                                | <b>79</b> |

|                         |            |
|-------------------------|------------|
| <b>Acknowledgments</b>  | <b>93</b>  |
| <b>Publications</b>     | <b>97</b>  |
| <b>Erklärung</b>        | <b>99</b>  |
| <b>Curriculum vitae</b> | <b>101</b> |



# Chapter 1

## Introduction

The new concept of electronics to add the spin degree of freedom of the electron to the standard charge-based microelectronics has emerged in the recent years. This so-called spin-based electronics, also dubbed as magnetoelectronics or spintronics, offers potential advantages such as non-volatility, increased data processing speed, reduced electrical power consumption, and increased integration densities [1]. Materials exhibiting a relatively high spin polarization are the key component for spintronics. Among all promising candidates, ferromagnetic semiconductors and half-metallic ferromagnets are considered to stand at the front row. The reason for using ferromagnetic semiconductor lies in its compatibility with conventional semiconductor devices and semiconductor processing techniques. Much attention has been heavily focused towards a broad range of diluted magnetic semiconductor (DMS) compounds, such as Mn-doped GaAs [2], Cr-doped ZnTe [3], and Mn-doped Ge [4]. Here the ferromagnetic properties are the result of incorporating magnetic dopants in the semiconductor hosts. On the other hand, the reason for employing half-metallic ferromagnets is that they are characterized by a finite density of states at the Fermi level  $E_F$  for electrons with majority spin, and an existence of a energy gap at  $E_F$  for electrons with minority spin, therefore giving the expectation to produce a fully spin polarized electrical current. Heussler alloys (e.g., NiMnSb, Co<sub>2</sub>MnSi), and oxides like Fe<sub>3</sub>O<sub>4</sub>, La<sub>0.7</sub>Sr<sub>0.3</sub>MnO<sub>3</sub>, and CrO<sub>2</sub> belong to this category. The last three compounds are claimed to have spin polarization of 80% [5], 96% [6], and 97% [7], respectively.

Due to its unique properties, the family of europium monoxide (EuO)

based materials has been also recently investigated for spintronic-related research. Stoichiometric EuO is a paramagnetic semiconductor with a band gap of 1.2 eV at room temperature [8, 9] and becomes ferromagnetic below a Curie temperature  $T_C$  of 69 K [10]. Here the magnetism originates from the  $\text{Eu}^{2+}$  ions. In the ferromagnetic state, there exists a spin splitting of the conduction band [11–13], resulting in a decrease and increase of the spin-up and spin-down band-gap, respectively. The spin splitting is large, i.e. 0.6 eV [14]. These properties make EuO to be a model compound for spin-filter tunneling experiments [15, 16]. Furthermore, upon electron-doping (for example by gadolinium or lanthanum), the transition temperature can be enhanced and the conductivity can be tuned to match to that of a conventional semiconductor. It was indeed demonstrated recently that doped EuO can be fabricated epitaxially on Si and GaN, proving its potential for spintronic applications [17]. Another interesting property is exhibited by Eu-rich EuO. Its semiconducting behavior alters into a metallic one at the magnetic transition temperature. In effect, the semiconductor turns into a half-metal. Therefore, Eu-rich EuO can also be used as a model for spin-injector materials. The bottom line is that EuO-related materials are ideal compounds for both fundamental and applied spintronic research. However, one needs to realize that to grow EuO in thin form is not trivial since Eu is more easily oxidized into higher oxidation state. Uncontrolled stoichiometry gives rise many defective physical properties, which are listed more detail in Section 1.2. Therefore, it is crucial to establish an appropriate procedure to grow high quality EuO thin films and to understand the growth mechanism. We will start the next subsection with a brief background information about EuO and Gd-doped EuO properties from the existing literatures.

## 1.1 Review of EuO and Gd-doped EuO properties

The successful effort to stabilize EuO in solid solution with SrO was first reported by Brauer in 1953 [18]. Since then, methods for preparing EuO were developed, but interest to investigate the properties of EuO was not apparent. It is in fact the discovery of ferromagnetism in EuO by Matthias *et al.* in 1961 [19] that generated the tremendous attention on this material. EuO in either bulk or thin film form were intensively investigated for its



structural, magnetic, electrical, and optical properties. A review on these investigations can be found in References [20–23].

### 1.1.1 EuO Growth

EuO crystallizes in the rocksalt structure with a lattice constant of 5.144 Å at room temperature [24]. To produce bulk EuO single crystals, very high temperatures of about 1800°C and an accurate starting composition were indispensable [25–27]. A slight deviation from the required conditions resulted in the formation of either Eu vacancies, oxygen vacancies, Eu clusters, Eu<sub>3</sub>O<sub>4</sub>, or Eu<sub>2</sub>O<sub>3</sub> phases. Due to this delicate crystallization path for achieving single-phase EuO, alternative synthesis routes for preparing EuO in thin film form were also pursued.

An attempt to grow EuO thin films was first reported by Ahn and Suits in 1967 [28]. Three different vacuum deposition techniques were employed, namely heating bulk EuO using an electron beam, simultaneous evaporation of Eu and Eu<sub>2</sub>O<sub>3</sub>, and reactive evaporation of Eu in oxygen atmosphere. They found that the magnetization of EuO films at 4.2 K is approximately 15% below that of bulk EuO. In the following years other deposition techniques were introduced and developed for fabricating not only EuO but also doped EuO thin films. Initially, co-evaporation of Eu and Eu<sub>2</sub>O<sub>3</sub> technique was mostly used, but then reactive evaporation of Eu metal in oxygen atmosphere was the preferential method for the film deposition. The substrate was generally heated at relatively low temperatures (< 500°C). The list of deposition conditions for undoped and doped EuO thin films until the year 1975 are summarized in Table 1.1. It is noted that all those depositions were done under technical vacuum conditions: the pressure during the deposition was mostly in the range of 10<sup>-6</sup>–10<sup>-5</sup> Torr. Comparing to the present-day knowledge of ultra-high vacuum, that pressure range may not be sufficient to avoid the presence of water or hydrocarbons in the films. Also, the substrates used were generally glass and fused quartz so that only polycrystalline films were obtained. All of these characteristics define the first period of EuO thin film growth.

Thin film preparation technologies, particularly molecular beam epitaxy (MBE) under ultra-high vacuum (UHV) conditions, have developed enormously since then. It enables the preparation of thin films in much cleaner environment. Moreover, modern analysis methods based on synchrotron radiation sources have become ready for use. So after almost two decades

Table 1.1: Deposition conditions for undoped and doped EuO thin films until 1975.

| Year | Works by                        | Deposition techniques   | $P$ during growth (Torr)             |
|------|---------------------------------|---|--------------------------------------|
| 1967 | Ahn <i>et al.</i> [28]          | – Heating bulk EuO using an electron beam<br>– Simultaneous evaporation of Eu and $\text{Eu}_2\text{O}_3$<br>– Evaporation of Eu in oxygen atmosphere | $10^{-6}$ – $10^{-5}$                |
| 1968 | Ahn <i>et al.</i> [29]          | Simultaneous evaporation of Eu, $\text{Eu}_2\text{O}_3$ , and rare earth oxides of either Gd, La, Nd, Ho, or Y  | $10^{-5}$                            |
| 1970 | Lee <i>et al.</i> [31]          | Rf sputtering into EuO target in Argon atmosphere   | not indicated                        |
| 1970 | Ahn [32]                        | Simultaneous evaporation of Eu, $\text{Eu}_2\text{O}_3$ , and Fe  | $1 \times 10^{-5}$                   |
| 1971 | Lee <i>et al.</i> [33]          | Simultaneous evaporation of Eu, $\text{Eu}_2\text{O}_3$ without/with Ag or Cu   | $\leq 8 \times 10^{-6}$              |
| 1971 | Ahn <i>et al.</i> [34]          | Simultaneous evaporation of Eu, $\text{Eu}_2\text{O}_3$ without/with Fe   | $\leq 2 \times 10^{-5}$              |
| 1971 | Suits <i>et al.</i> [36]        | Simultaneous evaporation of Eu and $\text{Eu}_2\text{O}_3$  | $\sim 10^{-6}$                       |
| 1971 | Paparoditis <i>et al.</i> [38]  | Reactive evaporation of Eu metal in oxygen atmosphere   | $\sim 10^{-5}$                       |
| 1972 | Ahn [39]                        | Simultaneous evaporation of Eu, mixture of $\text{Eu}_2\text{O}_3$ and $\text{Gd}_2\text{O}_3$ , and Fe   | $\leq 4 \times 10^{-7}$              |
| 1973 | Llinares <i>et al.</i> [40, 41] | Reactive evaporation of Eu metal in oxygen atmosphere   | not indicated                        |
| 1974 | Massenet <i>et al.</i> [42]     | – Oxidation on evaporated Eu metal on substrate<br>– Reactive evaporation of Eu metal in oxygen atmosphere  | $3 \times 10^{-7}$<br>$\sim 10^{-5}$ |
| 1975 | Llinares <i>et al.</i> [43]     | Reactive evaporation of Eu metal in oxygen atmosphere   | not indicated                        |

of pause, a strong renewed interest in EuO thin film research has emerged, triggered by these advances in preparation and analysis methods.

MBE-assisted EuO growth is in principle similar to the reactive evaporation of Eu metal in oxygen atmosphere described above, however here the system usually operates at a base pressure of low  $10^{-10}$ – $10^{-9}$  mbar. Epitaxy, single crystallinity, and stoichiometry of EuO film depends critically on growth conditions, namely substrate selection, substrate temperature  $T_S$ , oxygen pressure  $P_{O_x}$ , and Eu flux rate  $\Phi_{Eu}$ . Table 1.2 shows the MBE growth parameters from recent EuO studies.

Based on those studies, it is noted that epitaxial and single crystalline EuO films can be achieved using yttria-stabilized cubic zirconia (YSZ), MgO, BaO-buffered  $\text{SrTiO}_3$ , BaO-buffered Si,  $\text{YAlO}_3$ , SrO-buffered Si, and SrO-buffered GaN substrates, whereas polycrystalline EuO films were obtained when using  $\text{Al}_2\text{O}_3$ , bare  $\text{SrTiO}_3$ , or quartz glass substrates. Nevertheless, stoichiometry is still a serious problem. Several studies reported that  $\text{Eu}^{3+}$  contaminants are partially present in the films. It is not indicated clearly in those works how the growth parameters were controlled or checked. Remarkably, Steeneken and Tjeng *et al.* has developed a EuO growth method [14, 54] that ensures the film stoichiometry without requiring a precise control of the relative supply rate of oxygen and europium.

The method works based on two basic conditions. First, the Eu flux rate is set higher as compared to the oxygen flux, i.e. higher than needed

Table 1.2: MBE growth parameters from recent EuO studies.

| Year | Works by                        | Substrates                         | $T_S$<br>(°C) | Oxygen pressure<br>(Torr)                   | Eu flux rate<br>( $\text{cm}^{-2}\text{s}^{-1}$ ) |
|------|---------------------------------|------------------------------------|---------------|---|---|
| 1994 | Roesler <i>et al.</i> [44, 45]  | $\text{Al}_2\text{O}_3$ , YSZ      | 300           | not indicated                               | not indicated                                     |
| 1995 | Kawaguchi <i>et al.</i> [47]    | $\text{CaF}_2$ , MgO               | 300           | $10^{-9}$ – $10^{-8}$                       | not indicated                                     |
| 1997 | Sohma <i>et al.</i> [50]        | MgO, polyimide film                | 100–300       | $2$ – $3 \times 10^{-9}$                    | not indicated                                     |
| 2000 | Iwata <i>et al.</i> [52]        | BaO-buffered $\text{SrTiO}_3$      | 300           | $1.4 \times 10^{-8}$ – $1.4 \times 10^{-7}$ | $9.6$ – $10 \times 10^{13}$                       |
| 2000 | Iwata <i>et al.</i> [53]        | MgO                                | 300           | $4.6 \times 10^{-9}$ – $4.8 \times 10^{-8}$ | $2.8 \times 10^{13}$                              |
|      |                                 | $\text{SrTiO}_3$                   | 300           | $2.6 \times 10^{-9}$                        | $1.5$ – $2.1 \times 10^{13}$                      |
| 2002 | Steeneken <i>et al.</i> [14]    | Cr-covered $\text{Al}_2\text{O}_3$ | 280           | $1 \times 10^{-8}$ mbar                     | $\approx 3 \text{ \AA}/\text{min}$                |
| 2002 | Steeneken [54]                  | MgO                                | 300–400       | $1 \times 10^{-8}$ mbar                     | $1.2 \times 10^{13}$                              |
|      |                                 | YSZ                                | 300–550       | $1$ – $4 \times 10^{-8}$ mbar               | $1.2$ – $1.5 \times 10^{13}$                      |
|      |                                 | $\text{Al}_2\text{O}_3$            | 300–350       | $1 \times 10^{-8}$ mbar                     | $1.2$ – $1.3 \times 10^{13}$                      |
| 2003 | Lettieri <i>et al.</i> [55]     | BaO-buffered Si                    | 400–450       | $1$ – $2 \times 10^{-8}$                    | not indicated                                     |
| 2004 | Matsumoto <i>et al.</i> [56]    | quartz glass                       | 300           | $\sim 10^{-7}$                              | not indicated                                     |
| 2004 | Holroyd <i>et al.</i> [57]      | $\text{Al}_2\text{O}_3$ , YSZ      | 300           | not indicated                               | not indicated                                     |
| 2004 | Santos <i>et al.</i> [58]       | quartz, Si                         | R.T.          | $1 \times 10^{-6}$                          | not indicated                                     |
| 2006 | Ott <i>et al.</i> [59]          | MgO, $\text{Al}_2\text{O}_3$       | 350           | $6 \times 10^{-8}$                          | $\approx 11 \text{ \AA}/\text{min}$               |
| 2006 | Negusse <i>et al.</i> [60]      | Si                                 | not indicated | not indicated                               | not indicated                                     |
| 2007 | Lee <i>et al.</i> [61]          | MgO                                | 400           | $2 \times 10^{-8}$                          | not indicated                                     |
| 2007 | Schmehl <i>et al.</i> [17]      | $\text{YAlO}_3$ , Si, GaN          | 300–380       | $1.5$ – $4.5 \times 10^{-9}$                | not indicated                                     |
| 2008 | van der Laan <i>et al.</i> [62] | SrO-buffered Si                    | not indicated | $3 \times 10^{-9}$                          | not indicated                                     |
| 2008 | Ulbricht <i>et al.</i> [63]     | $\text{YAlO}_3$                    | 590           | $2.5 \times 10^{-10}$ – $1 \times 10^{-8}$  | $1.1 \times 10^{14}$                              |
| 2008 | Panguluri <i>et al.</i> [64]    | Si                                 | not indicated | $1 \times 10^{-7}$ mbar                     | not indicated                                     |
| 2008 | Miyazaki <i>et al.</i> [65]     | BaO-buffered $\text{SrTiO}_3$      | 350           | $8 \times 10^{-8}$ mbar                     | not indicated                                     |
| 2008 | Santos <i>et al.</i> [16]       | Si/SiO <sub>2</sub>                | not indicated | $3 \times 10^{-7}$                          | not indicated                                     |
| 2008 | Kimura <i>et al.</i> [66]       | BaO-buffered $\text{SrTiO}_3$      | 350           | $8 \times 10^{-8}$ mbar                     | not indicated                                     |
| 2009 | Arenholz <i>et al.</i> [67]     | SrO-buffered Si                    | not indicated | $3 \times 10^{-9}$                          | not indicated                                     |
| 2009 | Müller <i>et al.</i> [68]       | Si/SiO <sub>2</sub>                | R.T.          | $1$ – $2 \times 10^{-7}$                    | not indicated                                     |

R.T. denotes room temperature.

for obtaining Eu:O in a 1:1 ratio. A Eu-rich situation is then set during growth, and so the formation of  $\text{Eu}^{3+}$  species in the film can be prevented. However, this situation may also lead to the presence of Eu metal clusters. Therefore another condition is required, namely to keep the substrate at a sufficiently high temperature. During growth the excess of Eu metal will be re-evaporated back into the vacuum. Hence, the stoichiometry of EuO film then can be always maintained. Using this so-called Eu-distillation condition, the growth rate of the EuO film is determined by the oxygen pressure. We will employ this method to grow our EuO thin films, the results of which are presented in Chapters 3 and 4.

### 1.1.2 Magnetic properties

EuO is one of the very rare ferromagnetic semiconductor [10, 19]. In fact, ferromagnetic semiconductors are so rare that the very existence of ferromagnetism in insulators was even severely disputed in the mid fifties [21].

In a first approach to describe the ferromagnetism in EuO, one could start with an early model developed by Piere Weiss in 1907 [70]. The model considers only interactions between a local magnetic moment and an effective macroscopic field generated by the remainder of the crystal. For EuO case, one can think of a  $\text{Eu}^{2+}$  ion which carries a spin moment of  $7/2 \mu_B$  interacting with the effective field generated by the average net magnetic moment of the EuO crystal. It is noticed that the spontaneous magnetization of EuO follows a classical Brillouin function derived from the Weiss molecular (mean) field model [22, 70], which is expressed by

$$M = M(0)B_S \left( \frac{3S}{S+1} \frac{M}{M(0)} \frac{T_c}{T} \right), \quad (1.1)$$

where

$$B_S(x) = \frac{2S+1}{2S} \coth \left( \frac{2S+1}{2S} x \right) - \frac{1}{2S} \coth \left( \frac{1}{2S} x \right) \quad (1.2)$$

denotes the Brillouin function,  $M(0)$  the saturation magnetization at zero temperature, and  $S$  spin angular momentum. For EuO,  $S = 7/2$  and  $T_c = 69$  K. The expression of the reduced magnetization  $\sigma$  close to the zero temperature and the transition temperature [70] are,

$$\sigma = \frac{M(T)}{M(0)} = 1 - \frac{1}{S} \exp \left( -\frac{3S}{S+1} \frac{T_c}{T} \right), \quad (1.3)$$

and

$$\sigma \propto (T_c - T)^\beta, \quad \text{with } \beta = 1/2, \quad (1.4)$$

respectively, where  $\beta$  is one of the critical magnetic exponents in the ordered phase. However, it was found experimentally that the low temperature dependence was following more a  $T^{3/2}$  function, rather than a  $\exp(-C/T)$ , and that the critical exponent  $\beta$  was about 0.36 [71, 72], rather than 0.50.

To provide better description on those limits, the Heisenberg model is widely applied. The Heisenberg model suggests that spontaneous magnetization arises from exchange interactions between spin moments of neighboring atoms. For EuO, one can imagine that a localized  $4f$  moment of a  $\text{Eu}^{2+}$  ion interacts with  $4f$  moments of its nearest neighbors. Since the  $\text{Eu}^{2+}$  ions with the spectroscopic ground state of  $^8\text{S}_{7/2}$  are in a spherical symmetry

(*s*-type orbital), the exchange interactions are essentially isotropic, and can be described by the effective Hamiltonian,

$$H = - \sum_{i,j} J_{\text{ex}} \mathbf{S}_i \cdot \mathbf{S}_j, \quad (1.5)$$

where  $J_{\text{ex}}$  is the exchange integral related to the overlap of the charge distributions of the atoms at sites  $i$ , and  $j$  with spin moments of  $S_i$  and  $S_j$ , respectively. For a Heisenberg ferromagnet, parallel spin alignment is favored for a positive exchange integral  $J_{\text{ex}}$ . At zero temperature the ferromagnet is in its ground state with all spins fully aligned. Above zero temperature, the Heisenberg model describes the existence of low-lying excited states in the form of spin-waves. The reduced magnetization [73, 74] is then expressed by

$$\sigma = \frac{M(T)}{M(0)} = 1 - \frac{0.0587}{SQ} \left( \frac{k_B T}{2J_{\text{ex}} S} \right)^{3/2}, \quad (1.6)$$

where  $Q$  is 1, 2, 4 for simple cubic, body-centered cubic, and face-centered cubic, respectively, and  $k_B$  the Boltzmann constant. This equation is also known as the Bloch  $T^{3/2}$  law and describes the experimental finding very well.

Furthermore, the three-dimensional (3D) Heisenberg model is also able to account for the reduced magnetization just below the magnetic phase transition [75], which is given by

$$\sigma \propto (T_c - T)^\beta, \text{ with } \beta = 0.36. \quad (1.7)$$

Experimental values of the power law  $\beta$  for ferromagnet compounds vary between 0.30 and 0.38 [75], whereas  $\beta$  for EuO is 0.37 [71, 72]. Moreover, the Heisenberg model not only gives a good description of the magnetic properties of EuO at the very low temperature and in the vicinity of  $T_C$ , but also is able to reproduce the Brillouin-like shape for the temperature-dependent magnetization of EuO as shown by the mean field theory in Eq. 1.1. Hence, EuO is considered to be a clear realization of the 3D Heisenberg ferromagnet.

It is noted that there is no exact solution for the Heisenberg model in Eq. 1.5. Hence, as a first simplification, this model is limited to the *f*-*f* interaction of Eu nearest neighbors  $J_1$  and Eu next-nearest neighbors  $J_2$

[76]. Based on the Kasuya model [77], the Eu nearest neighbor exchange interaction  $J_1$  is due to a virtual excitation of a  $4f$  electron to a  $5d$  band which in turn interacts with the  $4f$  spin moment on the Eu nearest neighbors. This exchange leads to a ferromagnetic coupling. It was determined experimentally that the strength of  $J_1$  is  $5.22\text{--}5.39 \times 10^{-5}$  eV [78–80].

The origin of the Eu next-nearest neighbor exchange interaction  $J_2$  is more complex. Here oxygen  $2p$  bands are also involved to create various competing exchange paths between two next-nearest neighbor Eu ions. The main exchange mechanisms include the Kramers-Anderson superexchange giving rise to an antiferromagnetic coupling, and other mechanisms involving the  $5d$  band as intermediate states leading to a ferromagnetic coupling. The net  $J_2$  exchange from both contributions is ferromagnetic, however its strength is much smaller as compared to  $J_1$ . The experimental value of  $J_2$  is determined to be  $1.03\text{--}1.09 \times 10^{-5}$  eV [78–80]. In short, since the exchange integral  $J_1$  is more dominant, it is sufficient to attribute the ferromagnetic ordering in EuO to the spin-parallel interaction between nearest neighbors of Eu.

It is known that the Curie temperature of EuO can be substantially enhanced by chemical doping [21, 22, 29, 81] and pressure [82, 83]. For chemical doping, Gd is the mostly used from other rare-earth ions. The reason is that the magnetic system is fully preserved due to similar  $S = 7/2$  character of  $\text{Gd}^{3+}$ , and yet, Gd also donates an extra electron. Based on the model proposed by Kasuya and Yanase [21, 23, 84], the donor electron is trapped at the Gd site and polarizes neighboring  $\text{Eu}^{2+}$  ions via the Gd  $5d$ –Eu  $4f$  exchange interaction, thus creating a giant spin molecule or bound magnetic polaron. This additional exchange interaction is responsible for the increase in the Curie temperature  $\Delta T_C$ , which can be expressed as

$$k_B \Delta T_C = 2 \sum_{d,f} J_{df} \mathbf{s}_d \cdot \mathbf{S}_f, \quad (1.8)$$

where  $J_{df}$  is exchange constant between donor electrons with spin  $s_d$  and  $\text{Eu}^{2+}$  ions with spin  $S_f$ , and the summation runs over the number of donor electrons  $d$  as well as the number of neighboring  $\text{Eu}^{2+}$  ions  $f$ . Since the number of donor electrons equals to the Gd concentration  $x$ , the above equation can be approximately re-expressed as

$$k_B \Delta T_C \simeq x \left( 2 \sum_f J_{df} \mathbf{s} \cdot \mathbf{S}_f \right), \quad (1.9)$$

where  $s$  is the average spin  $s_d$  and the summation is only for the number of neighboring  $\text{Eu}^{2+}$  ions. It is noted that the last term on the right hand side is proportional to the exchange energy of the spin-splitting of the conduction band  $\Delta_{ex}$  and is appreciably reduced with increasing Gd doping [21]. In the case of low Gd doping, the first term ( $x$ ) is more dominant than the decrease of  $\Delta_{ex}$ , resulting in an enhancement of  $T_C$ . In contrast, for high Gd doping concentrations, the decrease of  $\Delta_{ex}$  is more dominant, leading to a decrease of  $T_C$  again. Thus, there exists an optimum Gd concentration for which  $T_C$  is maximal.

In this model,  $T_C$  changes continuously as a function of Gd concentration. Magneto-optical measurements on Gd-doped EuO single crystal by Schoenes and Wachter seemed to confirm this prediction [13]. On the other hand, Samokhvalov *et al.* showed that there is a threshold of the Gd concentration below which the  $T_C$  stays at its original value of 69 K. The threshold is at around 1.0–1.5% [85, 86]. Only for values higher than 1.5%, Samokhvalov could find an increase of  $T_C$ . This result was explained by a theoretical model proposed by Mauger *et al.* [22, 87, 88]. This model predicts that a bound "magnetic" polaron exists at low Gd doping without enhancing  $T_C$ . A sharp increase of  $T_C$  only occurs at a critical Gd concentration of about 1.3%, associated with the onset of indirect exchange interactions mediated by the then free donor electrons. At higher Gd concentrations,  $T_C$  decreases again after it reaches a maximum value at the optimum Gd doping level of about 7%. Here the ferromagnetic order becomes unstable due to a spiral arrangement along the [111] direction. In short, both the Kasuya–Yanase and the Mauger models predict the decrease of  $T_C$  at high Gd concentrations, however, with different physical mechanisms. At low Gd concentrations, both models describe the presence of bound magnetic polarons, but with different physical consequences, namely the non-existence versus existence of a Gd threshold for  $T_C$  to become enhanced. Recent mean field theoretical models [89, 90] obviously find that a small amount of Gd doping enhances  $T_C$  directly. To resolve this debate, magnetization measurements on high quality Gd-doped EuO samples with accurate Gd concentrations are required.

### 1.1.3 Transport properties

Stoichiometric EuO is a semiconductor with a band gap of 1.2 eV at room temperature. The band gap is reduced to about 0.95 eV at 20 K [8, 9, 11–13], as a result of the spin–splitting of the conduction band in the ferromagnetic state. The transport properties are highly sensitive to oxygen stoichiometry, pressure, illumination of light, and chemical doping. In Eu-rich EuO, a metal–to–insulator transition (MIT) occurs where the change in resistivity can exceed 10 orders of magnitude depending on the oxygen stoichiometry [91–94]. It is the largest resistivity change ever observed in nature. Upon applied magnetic field, colossal magnetoresistance (CMR) effect was revealed, where the resistivity reduces up to 8 orders of magnitude and the MIT shifts considerably to higher temperatures. It is also noted that the donor level due to the presence of oxygen vacancies is deep ( $\sim 0.28$  eV) at room temperature [21]. To describe the metal–to–insulator transition in Eu-rich EuO, several theoretical models have been proposed and it can be referred to as the He model [96], the bound magnetic polaron (BMP) model [97], and the ferromagnetic Kondo lattice (FKL) model [98].

By applying high pressure, the resistivity of EuO at room temperature strongly reduces together with the decrease of the band gap. Up to 25 GPa, the band gap still persist, but it is very narrow [83]. A huge change of resistivity of more than 10 orders of magnitude at around 200 K was observed by exerting quasi–hydrostatic pressure up to 250 kbar [82]. A MIT in stoichiometric EuO can also be induced by illumination of light [14, 95], i.e. the conductivity in the dark shows only semiconducting behavior, whereas conductivity with light exhibits a MIT.

Concerning the transport properties of Gd–doped EuO, however, there has been no common conclusion reached so far. Some authors observed a MIT [56, 91, 92, 99–101], which were described by the BMP model [22, 97] used for Eu-rich EuO. However, Schoenes and Wachter [13] claimed that there is no MIT. Their 1% Gd–doped EuO sample remains semiconducting below  $T_C$ . The donor level is rather shallow at about 17 meV. They stated further that the presence of oxygen vacancies in the other Gd–doped samples is likely responsible for the MIT. The absence of a MIT in lightly Gd–doped EuO was also asserted by Tsuda *et al.* [23]. However, these authors also claimed that for higher Gd–doping, i.e. when the doped electrons form a band, the transport behavior for Eu–rich EuO and Gd–doped EuO are very similar. This issue needs to be clarified; our preliminary results



indicate that Gd-doped EuO shows no MIT for low Gd concentrations.

#### 1.1.4 Optical properties

Spectacular optical properties were also exhibited by EuO-based materials. Using optical absorption measurements, it was discovered that the absorption edge in EuO shows a large red shift with decreasing temperature [8, 11]. In Gd-doped EuO, the red shift of the absorption edge decreases with increasing Gd concentrations, suggesting a decrease of the exchange splitting of the conduction band [21]. The refractive index  $n$  of EuO at the absorption edge also changes with temperature. It has a value of 2.25 at room temperature [102] and increases with lower temperatures. The increase is sharp around  $T_C$ . The low temperature value for  $n$  is about 2.45 [103].

In addition, large magneto-optical Kerr and Faraday effects were exhibited by EuO and Gd-doped EuO. For example, a polar Kerr rotation of 7.1 degrees in a EuO single crystal was observed at a photon energy ( $h\nu$ ) of 1.4 eV and a temperature of 10 K [104], and a specific Faraday rotation of  $5 \times 10^5$  degree  $\text{cm}^{-1}$  in EuO film was found at  $h\nu \sim 1.9$  eV and  $T = 5$  K [28]. Furthermore, Gd-doped EuO film also displayed a large longitudinal Kerr rotation of about 4 degrees at  $h\nu \sim 2.1$  eV and  $T = 6$  K [29]. More discussion about optical properties of EuO and Gd-doped EuO can be found in Ref. [21, 22, 105].

#### 1.1.5 Electronic structure

The electronic structure of EuO has been well studied using modern electron spectroscopies [54, 61]. The typical valence band spectra of EuO consist of a  $\text{Eu}^{2+}$   $4f$  band at  $\sim 2$  eV binding energy and a O  $2p$  band at 4–7 eV binding energy. If  $\text{Eu}^{3+}$  contaminants are present, then the valence band spectra become very different, i.e. the  $\text{Eu}^{2+}$   $4f$  intensity is reduced and a  $\text{Eu}^{3+}$   $4f$  multiplet structure appears at 6–12 eV binding energies. If, on the other hand, Eu metal is present, then the spectral features appear at the Fermi level.

The typical conduction band spectra are comprised of Eu  $5d$ – $6s$  band. The bottom of conduction band, mainly a Eu  $5d_{t_{2g}}$  band, is situated 1.2 eV above the top of the Eu  $4f$  valence band. The Eu  $5d_{e_g}$  band is located 3–4 eV above the Eu  $5d_{t_{2g}}$  band due to crystal field splitting [102, 104]. The description given above is for EuO above the Curie temperature. Be-

low  $T_C$ , the conduction bands for spin-up and spin-down split due to the indirect exchange interaction between Eu  $4f$  and Eu  $5d$  moments. This spin-splitting is 0.6 eV [14]. The band gap for spin-up is then reduced to  $\sim 0.9$  eV, while the band gap for spin-down is increased to  $\sim 1.5$  eV.

## 1.2 Motivation and Scope

There is a strong renewed interest in EuO in the last decade. Many thin film research groups attempted to utilize those spectacular properties for device applications. Yet it also becomes clear that the quality of the EuO thin film are often questionable. Most of the reported studies showed the presence of  $\text{Eu}^{3+}$  contaminants, oxygen vacancies, or even Eu metal clusters in their films [16, 44, 45, 53, 57, 60, 62, 67]. There is clearly a difficulty in controlling the EuO stoichiometry, leading to serious consequences for the properties. Several studies [48, 50, 55, 64] indeed revealed that the saturation magnetic moments is only 3.5–5.5  $\mu_B$  per Eu ion, far away from the expected 7  $\mu_B$ .

Another intriguing aspect with regard to EuO thin films is about the growth itself. One of the earliest studies reported that EuO film can be grown epitaxially on a lattice-matched substrate, e.g. yttria-stabilized cubic zirconia (YSZ) [44, 45]. Surprisingly, epitaxial EuO growth was also observed on MgO substrates [14, 47, 50, 53, 61] despite of the very large lattice mismatch of about 20%. Moreover, many studies also reported epitaxy of EuO using other substrates [17, 52, 55, 61–63, 65–67]. Yet, there is no report in the literature for a sustained layer-by-layer growth of EuO thin films.

Many studies reported that thick capping layers of more than 1000 Å were needed to protect the film from deterioration under ambient conditions, and some of them showed that such thicknesses were even not leak-tight. One may infer that most of those films must have a significant film or surface roughness. Therefore, achieving EuO layer-by-layer could be very important to obtain very smooth film surfaces so that leak-tight capping layers can be fabricated.

The first part of our goal is therefore to grow a high quality single-crystalline EuO thin film in an epitaxial and layer-by-layer manner with excellent stoichiometry and proper ferromagnetic properties by means of the MBE-distillation technique. We have chosen yttria-stabilized cubic

zirconia (YSZ) as substrate, despite the claim in the literature that the EuO stoichiometry on YSZ can not be controlled [17, 54] due to the fact that YSZ acts as an oxygen source [118]. We will show in Chapter 3 that we do have achieved full control of the growth process. We will use these results as a firm basis for Gd-doped EuO studies, as the second part of this thesis work.

For doping dependence studies, Gd-doped EuO is considered to be a prime example. The magnetic system is expected to be undisturbed since Gd has a  $4f^7$  character with the  $^8S_{7/2}$  ground state, similar to  $\text{Eu}^{2+}$ . Also the structural change is negligible since Gd and Eu have rather similar atomic radii. It is commonly accepted that an extra electron provided by Gd doping will enhance the Curie temperature  $T_C$ . However, many studies in the past reported optimum  $T_C$  values which vary appreciably from 115 K to 170 K [13, 29, 56, 59, 81, 85, 86, 88, 100, 122–124]. Moreover, the temperature-dependent magnetization curves differ significantly from the Brillouin-like function, expected for a Heisenberg system. Whether or not a critical Gd concentration exists for an increase in  $T_C$  is also not clear. [13, 56, 85, 86, 122–124].

A possible cause for these uncertainties is the problem of stoichiometry [13, 23]. For example, if  $\text{Eu}^{3+}$  contaminants co-exist together with Gd doping, the extra electron of the Gd may be used to convert the  $\text{Eu}^{3+}$  into  $\text{Eu}^{2+}$  ion so that in the end the system has no effective extra electron. Thus, in this case, the  $T_C$  can not increase. On the other hand, if oxygen vacancies are unintentionally introduced in the Gd-doped film, one could get extra exchange paths by which the  $T_C$  can be increased. The shape of the temperature-dependent magnetization could then also show many curvatures [56]. Another important remark is that the actual Gd concentrations in the films were not even known accurately [23].

To solve the problem of controlling the stoichiometry, we will use the Eu-distillation process for growing high quality Gd-doped EuO films. We will investigate whether this procedure allows for a film growth free from any possible contaminants and yet ensures a layer-by-layer growth as well. Our objective is then to establish the magnetic properties of the true high quality Gd-doped EuO films as a function of well defined Gd-concentrations.

Chapter 2 describes briefly the experimental methods used for this thesis work. Molecular beam epitaxy (MBE) technique will be introduced first, and it will be followed by *in-situ* and *ex-situ* analyzing techniques employed

for structural, chemical, magnetic, and electronic characterization of EuO and Gd-doped EuO films.

In Chapters 3 and 4 we present our experimental study on MBE-assisted EuO film growth on YSZ substrate using the Eu-distillation process. We will discuss epitaxy and stoichiometry during both the initial (Chapter 3) and sustained stages (Chapter 4) of growth. A proof of a sustained layer-by-layer EuO growth will also be given.

Chapter 5 describes the results of our Gd-doped EuO film growth study on YSZ substrates. We will show that the presence of Gd even helps to stabilize the layer-by-layer growth mode. A reliable method based on x-ray absorption spectroscopy (XAS) to determine the stoichiometry and the actual Gd concentrations of the films is also presented. Finally, we will discuss the magnetic properties of the well-defined Gd-doped EuO films.

Our soft x-ray magnetic circular dichroism (SXMCD) study on Gd-doped EuO film is reported in Chapter 6. Here the main discussion is to resolve the magnetic coupling between Gd and Eu spins. We will show that Gd and Eu spins are aligned parallel. Finally, Chapter 7 is dedicated to the epitaxial growth of EuO on MgO.

## Chapter 2

# Experimental methods

In the first part of this chapter we will start with an introduction to the basic principles of molecular beam epitaxy (MBE) as one of the most fundamental technique for growing thin films. It will be then followed by a description of our specific oxide MBE facility, dubbed as Mini-MBE, which was used for growing the EuO and Gd-doped thin films. Subsequently, we will briefly describe the preparation of substrates, the fabrication of the films, and the capping the films for *ex-situ* characterization.

In the second part of this chapter we will introduce analyzing techniques which were utilized to characterize the films. Reflection high-energy electron diffraction (RHEED), low-energy electron diffraction (LEED), and x-ray photoemission spectroscopy (XPS) will be described first as the main techniques for *in-situ* characterization. Then it will be followed by x-ray absorption spectroscopy (XAS), x-ray reflectivity (XRR), and superconducting quantum interference device (SQUID) magnetometer for *ex-situ* characterization. We will include in each subsection description of our experimental set-ups as well as their important specifications.

## 2.1 EuO thin film growth by means of molecular beam epitaxy (MBE)

### 2.1.1 General considerations of MBE

The molecular beam epitaxy (MBE) technique has developed into its maturation stage after its invention in the early 1960s. It has proven to be

one of the most important and versatile tools for growing semiconductor, metal, insulator, or superconductor thin films, both at the research and the industrial level. MBE under ultra-high vacuum (UHV) environment offers notably a production of high quality single-crystalline thin films in an epitaxial manner with monolayer (ML) control. A detailed description and thorough explanation about the fundamental and current status of MBE as well as UHV-related technologies can be found in the books written by Herman and Sitter [106], Ohring [107], and Prutton [108].

The MBE growth process can be divided into three steps. The first step is the production of molecular beams. "Molecular" beams that essentially consist of atoms in gaseous state are generated by heating up a solid material source at a certain temperature. The uniformity and stability of the molecular beam flux determines the uniformity of the film thickness and its composition. It is necessary therefore to choose an appropriate effusion cell with an accurate temperature control, as well as to specify a proper geometry between the source and the substrate.

The next step is the transport of molecular beams to the substrate. After sublimation of the solid source, the mass flow of molecular beams traverses to the substrate. However, on the route to the substrate, the molecular beams may suffer scattering with molecules of the residual gas if the pressure in the chamber is not sufficiently low, which in turn may degrade the directionality and uniformity of the beam nature of the mass flow. To avoid this undesired scattering process, an admissible value of the total pressure of the residual gas has to be ensured. It is derived that the total pressure of the residual gas in the chamber in the range of  $10^{-3}$ – $10^{-4}$  mbar [106] is adequate to create rather long mean free paths of the beams, so that the uniformity of the mass transport can be maintained. Nevertheless, UHV conditions in the  $10^{-9}$ – $10^{-11}$  mbar range are highly required in order to keep the purity of chemical composition in every layer of the film, or in other words, to produce a film free from any contaminants.

The last step for the growth process in MBE is the deposition of the molecular beams onto the substrate. The underlying physical and chemical process occurring on the substrate surface may vary from one case to another. Some of elementary processes will be briefly discussed as follows. The molecules or atoms first arrive on the surface. If the surface substrate is atomically rough, the deposited atoms (adatoms) are incorporated directly at the position where they arrived. In this case the atomic migration on

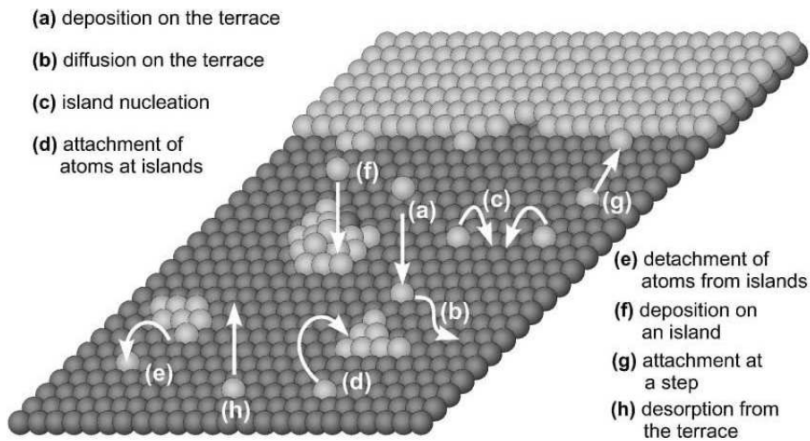


Figure 2.1: Variation of surface elementary process in molecular beam epitaxy. This picture is retrieved from Ref. [109].

the surface is negligible. However, in normal MBE growth, atomically flat surfaces are employed, i.e. surfaces having smooth and large terraces with only monoatomic steps. On such surfaces, the absorbed atoms or molecules can meet other adatoms to nucleate into two-dimensional adatom clusters as illustrated in Fig. 2.1. It is also possible that the atoms propagate along the surface until they find a step edge. If they are on an upper terrace, they are preferentially reflected back at the step edge due to Ehrlich–Schwoebel (ES) step edge barrier. Conversely, if they are on a lower terrace, depending whether the step edge is atomically rough or smooth, they can be either attached (or detached) at the step edge or can further migrate along the step to find a kink, respectively. Another important process that often occurs is thermal desorption of the atoms on the terrace back to vacuum, especially when the substrate temperature is high enough. We will show in Chapters 3 and 4 that this process plays a dominant role in producing epitaxial and stoichiometric EuO thin films.

Classically, there are three basic modes of thin film growth, namely the three-dimensional (3D) island (or known as Volmer–Weber), the layer-by-layer (or Frank–Van der Merwe), and the layer-plus-island (or Stranski–Krastanov). Island growth happens when adatoms are more strongly bound to each other than to the substrate so that they successively coalesce to form

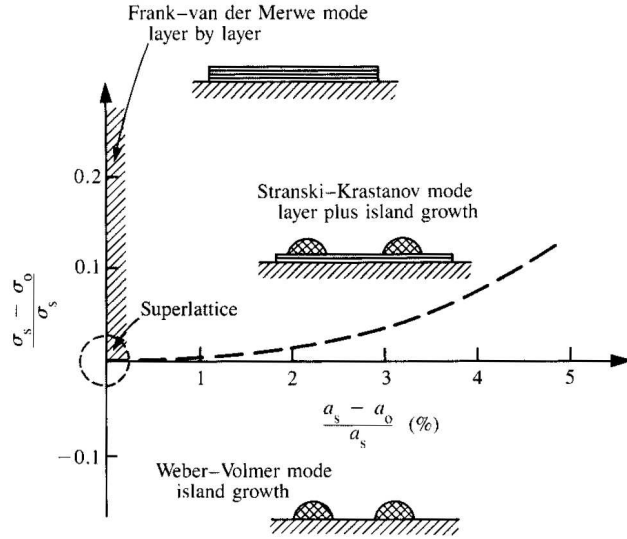


Figure 2.2: Schematic diagram to illustrate stability regimes of the three basic thin film growth. Surface energy difference between film  $\sigma_o$  and substrate  $\sigma_s$  is plotted as a function of lattice misfit.  $a_o$  and  $a_s$  denote the lattice parameters of the film and the substrate, respectively. This picture is retrieved from Ref. [110].

films consisting 3D islands. They tend to agglomerate as they grow since the surface energy of the film  $\sigma_o$  is greater than that of the substrate  $\sigma_s$ . As schematically illustrated in Fig. 2.2, island growth even occurs when there is no lattice misfit between the film and the substrate. Moreover, its range of dominance expands when the lattice misfit is larger. The diametrically opposed situation occurs during a layer-by-layer growth. Here adatoms are more strongly bound to the substrate or underlayer than to each other, providing for the formation of a two-dimensional (2D) layer. During the layer-by-layer growth the wetting of adatoms on the substrate is significant since its surface energy is less than that of the substrate. Remarkably, the layer growth is possible when there is a slight lattice misfit, indicating that the strained-layer epitaxy is also feasible. In between these two modes, the layer plus island growth mechanism exists. In this intermediate case, a formation of one or more layers is favorable in the initial stages, however island growth becomes dominant in the subsequent stages. The dashed line depicted in Fig. 2.2 denotes the separation between the island and the



layer-plus-island growth.

### 2.1.2 Mini-MBE set-up

The preparation of EuO thin films is carried out in the so-called oxide Mini-MBE chamber. The main body of the chamber has a cylindrical shape which consists of three circles of flanges. The first circle is the place where deposition of EuO thin films occurs. It has flanges for two effusion cells, a reflection high-energy electron diffraction (RHEED) gun and an Al-coated phosphor screen, as well as a water cooled Sycon-100/MF quartz crystal microbalance thickness monitor. The Eu effusion cell is located exactly perpendicular to the sample surface at the growth position, whereas the Gd effusion cell is at an angle of  $40^\circ$  away from the normal of the sample surface. The Gd effusion cell has an external water cooling system to reduce the heat load towards the chamber. The RHEED gun and Al-coated phosphor screen are situated parallel to the sample surface. The specification of the RHEED gun will be described later. The quartz crystal thickness monitor is located at the top flange. It can be moved to the growth position, monitoring accurately the actual molecular beam fluxes prior and after each film deposition.

In the second circle, there are two parking lots to store samples and a wobble stick. The third circle is equipped with a heating stage, a leak valve with a nozzle directed towards the heating stage, and a wobble stick. The heating stage is used for annealing substrates up to  $600^\circ\text{C}$ . Supply of molecular oxygen is introduced to the chamber via the leak valve for annealing and also growing EuO films. The wobble stick is utilized for transferring the substrate or the film from and to three different places, namely the load lock system located at the top flange separated via a valve, the heating stage, and the manipulator.

The manipulator has three degrees of freedom and can be resistively heated up to  $400^\circ\text{C}$ . It is used to bring the annealed substrate to the growth position and optimize its position during RHEED monitoring. After growth, it is also used to transfer the film to an additional chamber next to the main body, where an MKS quadrupole mass-spectrometer and a wobble stick are placed. The mass-spectrometer is important for monitoring the partial pressure of oxygen during EuO growth. The wobble stick is employed for transferring the film to another manipulator arm, which in turn brings the film to an *in-situ* characterization chamber for x-ray pho-

toelectron spectroscopy (XPS) and low-energy electron diffraction (LEED) analysis, and/or to an Al effusion cell chamber for capping the film.

The Mini-MBE operates under ultra high vacuum conditions, which is maintained by a cryopump. The base pressure is  $2 \times 10^{-10}$  mbar. To reduce mechanical low-frequency vibrations produced by the cryopump, a bellow-like vibration damper is mounted between the cryopump and the main body. A turbo pump is employed for pumping the load lock system and for regenerating the cryopump when necessary.

### 2.1.3 Substrate preparation

The substrates used for growing EuO thin films were yttria-stabilized cubic zirconia (YSZ) (100), MgO (100) and Al<sub>2</sub>O<sub>3</sub> (1 $\bar{1}$ 02). Prior to introducing it to the load lock system of the Mini-MBE chamber, a substrate was mounted on a stainless steel sample holder by clamping it with stainless steel foils on both side edges. To improve the thermal contact and the temperature uniformity of the substrate, it was necessary to insert a golden foil between the substrate and the sample holder. Epi-polished single crystals YSZ substrates were purchased from SurfaceNet GmbH. The YSZ substrate is basically a ZrO<sub>2</sub> which is doped by a 9.5% Y<sub>2</sub>O<sub>3</sub> in order to have a stable cubic structure with a calcium-fluorite type and a lattice constant of 5.142 Å [111, 112]. The YSZ substrates were annealed at 600°C for at least 2 hours in an oxygen atmosphere of  $5 \times 10^{-7}$  mbar. MgO substrate has a rocksalt crystal structure with a lattice constant of 4.21 Å [24]. It was cleaved *ex-situ* along the (100) planes from single crystal blocks sold by TBL-Kelpin and then annealed for at least 1 hour at 600°C in an oxygen atmosphere of  $1 \times 10^{-7}$  mbar. These two substrates were used for experiments, the results of which are presented in Chapter 3 and 4. For results presented in Chapter 5, epi-polished single crystal of Al<sub>2</sub>O<sub>3</sub> (1 $\bar{1}$ 02) and MgO (100) were used as substrates. Al<sub>2</sub>O<sub>3</sub> substrate has a hexagonal structure with  $a = 4.763$  Å and  $c = 13.003$  Å [24]. The Al<sub>2</sub>O<sub>3</sub> and MgO substrates were annealed in an oxygen atmosphere of  $1 \times 10^{-7}$  mbar at 600°C and 450°C, respectively. These annealing procedures led to atomically clean and well-ordered surfaces as indicated by RHEED and LEED patterns.

#### 2.1.4 Fabrication of EuO thin film

Prior to each growth, a high purity Eu metal in a boron–nitride (BN) crucible from an EPI effusion cell was heated up until a constant flux rate was reached. The Eu flux rate was kept at about 8 Å/min, unless it is stated otherwise. Oxygen was then supplied through a leak valve and kept a desired and stable oxygen atmosphere as monitored by the ion gauge and mass–spectrometer. To fulfill the Eu–distillation condition [54], we set the Eu flux rate higher than the oxygen one, and we set the substrate temperature at 400°C, unless stated otherwise. Immediately after the shutter of the Eu effusion cell was opened, Eu atomic beam was sublimated on the heated substrate under the oxygen atmosphere to form EuO film. During growth, particularly at the initial stages of growth, RHEED intensity oscillations were recorded. The growth was terminated by closing first the oxygen leak valve, and then the Eu shutter after 30 seconds, and finally lowering the sample temperature down. At the end, the film was transferred to the XPS and LEED chamber for further chemical composition and structural characterization. The Eu flux rate was checked again immediately after the film growth.

For Gd–doped EuO thin film growth, all the growth procedures are similar as described above, except that a high purity Gd metal was co–evaporated from a separate effusion cell, i.e. a commercial Luxel RADAK I Knudsen cell with Molybdenum–inserted Al<sub>2</sub>O<sub>3</sub> crucible.

#### 2.1.5 Capping EuO thin film

Since EuO and Gd–doped EuO thin films are highly sensitive to air, they need to be protected before they can be taken out of vacuum. For this purpose, aluminum was used as a protective capping layer. The deposition of Al onto the film was performed at room temperature. The Al–capped samples were then ready to be further characterized using *ex-situ* analysis methods, namely x–ray absorption spectroscopy (XAS), x–ray reflectivity (XRR), and superconducting quantum interference device (SQUID) measurements. From XRR analysis, it was revealed that the thicknesses of the Al capping layer was about 20–40 Å.

## 2.2 *In-situ* characterization

### 2.2.1 RHEED

Reflection high-energy electron diffraction (RHEED) is one of the standard surface-sensitive techniques that allows one to characterize the surface structure and to monitor the growth process in an *in-situ* and real-time manner. The high-energy electron beam, which is generated by an electron gun in the range of 10–30 kV, impinges upon the film surface at a grazing angle of less than  $3^\circ$ . The elastic and forward electron scattering gives rise to a diffraction pattern that is observable on a fluorescent screen. The penetration depth of the electron beam in the film is very limited, less than 10 Å, due to the low incident angle geometry. Thus, the information about the quality and crystallographic nature of the outermost atomic layers can be well revealed by the RHEED technique.

In RHEED, the interaction of the electron beam is essentially with a two-dimensional (2D) atomic layer. There is no periodic atomic arrangement or translational symmetry in the third dimension. As a consequence, a reciprocal space representation of the film surface is in the form of reciprocal lattice rods perpendicular to the surface plane, and not reciprocal lattice points as in the three-dimensional (3D) case. Here, only two out of three Laue diffraction conditions are satisfied. The diffraction occurs at the points where each of the lattice rods intersect with the Ewald sphere. On the other hand, due to high electron energy, the radius of Ewald sphere is very large as compared to the reciprocal lattice rods constant. The Ewald sphere therefore intersects the lattice rods almost along their lengths. The resulting RHEED pattern consists of long and equally spaced streaks, normal to the shadow edge of the film. The distance between the streaks corresponds to the in-plane lattice constant of the film.

The relation between the RHEED pattern and the flatness of the single-crystalline film surface is illustrated in Fig. 2.3. If the film surface is perfectly flat, the RHEED pattern shows sharp and long streaky pattern as shown in the bottom of the Fig. 2.3. The diffraction from a rather rough surface results in the RHEED pattern comprising streaks with modulated intensities (or elongated spots). This is illustrated in the middle panel. If the surface is completely rough, many electrons scatter in different directions through reflection and transmission due to surface asperities and 3D islands, resulting in the transmission-like RHEED pattern. The top

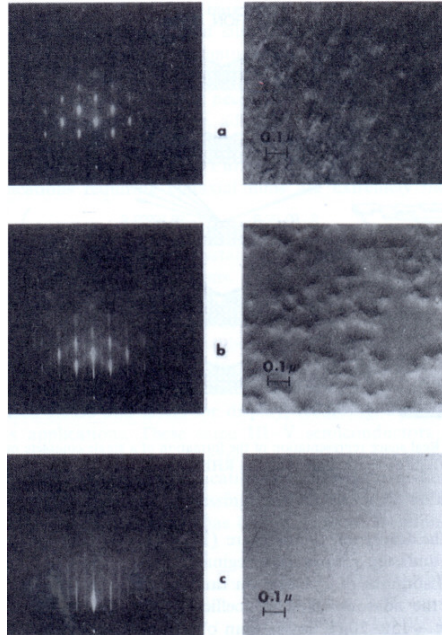


Figure 2.3: RHEED patterns and corresponding electron micrograph of similar GaAs surface with different preparation and growth conditions. This picture is retrieved from Ref. [107]. It basically illustrates the relation between the RHEED pattern and the flatness of the surface.

panel of Fig. 2.3 depicts such RHEED pattern, where spots are arranged orderly. Moreover, a polycrystalline and an amorphous surface give only diffuse background with concentric rings feature or no diffraction pattern at all.

RHEED technique also offers the possibility to monitor the intensity of diffraction patterns in a real-time manner during growth. Typically, the RHEED intensity of the specularly reflected electron beam oscillates in a form of sine-like wave as a function of time, which corresponds to a layer-by-layer growth. In this growth mode, new adatoms nucleates two-dimensionally to form a complete layer before the next one starts. The RHEED oscillation period therefore indicates precisely the duration needed for the formation of a complete single layer. One approach based on the dynamical or multiple scattering process explained that the origin of the RHEED oscillations is related to the fact that the step density due

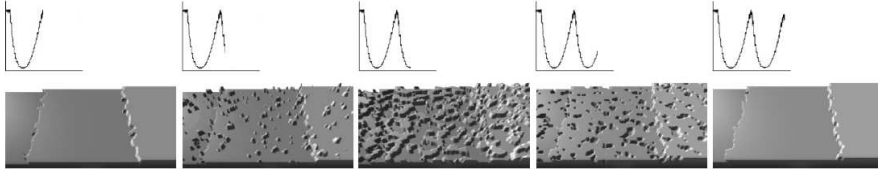


Figure 2.4: The correspondence between RHEED intensity oscillations and the morphology of film surface for an ideal two-dimensional (2D) nucleation layer-by-layer growth. This picture is retrieved from Ref. [113].

to the 2D nucleation varies periodically [114]. The step density itself is the cause for the diffuse scattering. Thus, a maximum RHEED intensity occurs when the step density is minimum, namely at the initial smooth surface and the complete growing layer. Reversely, a minimum intensity occurs at the maximum step density when the growing layer is half complete. This is schematically shown in Fig. 2.4.

It is also possible that the surface grows in a layer-by-layer mode, and yet the RHEED oscillations are absent. Contrary to the step density model described above, the origin of this phenomenon is attributed to the fact that new adatoms do not nucleate directly at the position where they came, but they all propagate to nucleate at the step edge of the terrace. In this step-flow model, the step density is always constant and no RHEED oscillation is expected. Nevertheless, the RHEED pattern still shows streaky features. In short, the layer-by-layer growth mode based on either 2D nucleation or step-flow process is highly desired to realize a smooth film surface.

On the other hand, the absence of RHEED oscillations may also be due to 3D islands nucleation growth. In this growth mode, the diffraction intensity due to multiple transmission and reflection processes is more dominant. The intensity from a pure specular reflection process is somewhat hidden in this case. As a result, a RHEED oscillation is not observable. The corresponding RHEED pattern shows many spots, indicating the roughness of the film surface. Although both 3D islands and 2D step-flow growth mode reveal no RHEED oscillations, one can still discriminate them by evaluating their RHEED patterns, whether they are indicated by spots or by streaks. All in all, RHEED is a powerful tool to study the surface or interface morphology and its evolution together with the mechanism of growth.

Our RHEED apparatus is the EK-35-R RHEED type from STAIB Instruments. The RHEED electron gun is normally operated at accelerating

voltage of 20 kV and filament current of 1.5 A. The electron beam can be moved horizontally and vertically using the deflection unit system in either remote or local mode. The best beam shape and focus are adjusted by the grid and focus function. An Al-coated phosphor screen is located at the opposite side of the electron gun to detect the RHEED pattern. To get rid of the concentric rings pattern arising from part of the primary beam that does not hit a sample but arrives at the screen, a moveable beam shutter is mounted between the sample and the screen. The RHEED pattern can be recorded as an image and also as a video using a CCD camera which is interfaced to a computer. A commercial EE-2000 program is then used to analyze the recorded RHEED pattern in more detail.

### 2.2.2 LEED

Low-energy electron diffraction (LEED) is also a surface-sensitive technique that can deliver information about surface structure and surface lattice symmetry. A low-energy electron beam of less than 1000 V is incident perpendicularly upon the film surface and only penetrates a few angstroms below the surface. The elastically back-scattered electrons give rise to a diffraction pattern that is detected using a fluorescent hemispherical screen.

Since the electron beam energy is low, the radius of Ewald sphere is quite comparable to the reciprocal lattice rods constant. Therefore, instead of along its length, the Ewald sphere will intersect only the lattice rods at particular points that fulfill Laue diffraction condition. The resulting LEED pattern consists of an ordered arrangement of spots. The distance between the spots provides direct information about the in-plane lattice constant of the surface.

Our LEED apparatus is the Rear View LEED with T191 Electronics from Thermo Vacuum Generators Scientific. The LEED electron gun is normally operated at filament current of 2.6 A. The distance between the electron gun and the sample is 4–6 cm. At several particular electron beam energy, clear and sharp LEED spots are obtained by adjusting the retarding mesh voltage and the emission current of the electron gun. The LEED patterns are recorded as images using a CCD camera which is interfaced to a computer. The recorded LEED patterns are further analyzed using the commercial EE-2000 program.

### 2.2.3 XPS

X-ray photoelectron spectroscopy (XPS) is a powerful analysis technique in surface physics that can provide valuable information about the electronic structure and the chemical composition of the film. Mono-energetic soft x-rays, which are generated by an x-ray tube, irradiate the sample with a penetration depth of 1–10  $\mu\text{m}$ . The probing depth of this technique, however, is limited by the inelastic mean free path of the photoelectrons. The electron escape depth is typically of 5–20  $\text{\AA}$ . The electrons that escape from the sample into vacuum are measured by an electron energy analyzer with respect to their kinetic energy.

Since the kinetic energy of the photoelectrons depends on the binding energy of electron in the solid, the photoemission spectrum can be reformulated as a function of their binding energies using the energy conservation expression,  $E_B = h\nu - E_{kin} - \phi_a$ , where  $E_B$  denotes the binding energy,  $h\nu$  the energy of the incoming x-rays, and  $\phi_a$  the work function of electron analyzer. The spectrum commonly comprises sharp peaks which come from photoelectrons with negligible energy loss, and a background feature which comes from photoelectrons suffering energy losses due to inelastic scattering with others electrons inside the solid. The photoelectron spectrum is often also accompanied by Auger electron peaks. Auger electrons are emitted with the kinetic energies that are gained via the decay process of an electron from a higher energy level into the core hole that was created by the incoming x-rays. Unlike the photoemission peaks, the kinetic energy of the Auger lines is independent of the energy of the x-ray source.

In a one electron framework where electron–electron interactions are neglected, it is commonly accepted that the photoemission spectrum is interpreted as the occupied density of states (DOS) of the sample. However, to describe the spectrum in a many body picture, the term DOS is not valid anymore. One rather needs to interpret it as an excitation spectrum of all accessible one–electron removal final states starting from the ground states (The sample is usually assumed to be at 0 K). The binding energy is therefore defined as the difference between the total energies of the excited final state and the ground state. Since the binding energies of particularly core electrons are specific for each element, the photoemission spectra can then also be used for determining the chemical composition. Thus XPS is also commonly referred to as Electron Spectroscopy for Chemical Analysis (ESCA).



Our ultra-high vacuum photoemission chamber is made of  $\mu$ -metal, allowing to perform experiments free from the disturbance of external stray magnetic fields. The x-ray source consists of an electron gun, a water-cooled Al anode, and a Vacuum Generators twin crystal monochromator. The generated electrons are accelerated up to 10 kV and focused on the water-cooled Al anode. The anode emits its characteristic x-ray spectral lines together with a continuous background. It is then monochromatized by Bragg refraction at two separately adjustable quartz crystals for the Al  $K_\alpha$  line at 1486.6 eV. The monochromatized x-ray is finally focused onto the sample. Photoelectrons are collected using the Gammadata Scienta SES-100 electron energy analyzer unit. It consists of an electron-lens system, a hemispherical deflection analyzer, and a micro-channel plate (MCP) with phosphor screen as a detector unit.

The electron-lens system is used to focus the photoelectrons onto the analyzer entrance slit, and to decelerate (or accelerate) their kinetic energies in order to be matched with a selected energy scanning range. At the hemispherical analyzer, an electrostatic field within two concentric hemispheres with radii of 110 mm and 190 mm is established to only allow photoelectrons of a given energy (the so-called pass energy) to arrive at the detector slits and onto the MCP detector itself. The MCP serves as an electron multiplier with a gain of the order of  $10^6$ . These electrons then arrive at the phosphor screen, where light flashes are emitted and subsequently recorded by a CCD Camera. The position of the light flash is related to the kinetic energy of the photoelectron. The detection unit is connected to a computer and controlled via the SES software. The recorded spectra can be further analyzed using the IGOR 4.1 software.

## 2.3 *Ex-situ* characterization

### 2.3.1 XAS

Soft x-ray absorption spectroscopy (XAS) has been developed in the late 1980s, and by now it has proven to be a very powerful tool to study the local electronic structure of transition metal and rare-earth compounds. Intense and tunable x-ray beams provided by a synchrotron radiation facility are absorbed in a sample. This absorption promotes an electron from a core level to an unoccupied one above the Fermi level, and as a result, a hole is left behind at the core. As the excited atom is energetically unstable,

it will relax through either radiative or non-radiative decay. The radiative decay in the form of photon occurs when an energetic electron refills back the core hole. The absorption intensity is proportional to the number of photons created by de-excitation of the electrons into the core holes. This absorption detection method is known as the fluorescent yield (FY) mode. The probing depth of this method is in the order of 1000 Å.

The non-radiative decay occurs when the energy gain due to the refilling of the core hole by the energetic electron, is transferred by an Auger process to another electron, which then escapes from the sample surface. The charge loss of this secondary electron will be neutralized by the drain current since the sample is connected to the ground. The current is measured by a pico-amperemeter and is proportional to the absorption intensity. This detection method is known as the total electron yield (TEY) mode. The probing depth of this method is 40–100 Å depending on the material.

The most interesting x-ray absorption (XA) spectra are realized in the region of  $K$  edge ( $1s \rightarrow 2p$  transition),  $L_{2,3}$  edges ( $2p \rightarrow 3d$ ), and  $M_{4,5}$  edges ( $3d \rightarrow 4f$ ) for the  $2p$  compounds (C, N, O, and F), transition metal, and rare earth ions, respectively, since these transitions are dipole allowed and they have much higher absorption cross section as compared to other transitions. The x-ray absorption spectrum is characterized by some typical features. Take an example of  $M_{4,5}$  edges spectrum. It has two groups of peaks which are assigned to two possible final core states with the hole spin parallel or antiparallel to its orbital angular momentum, i.e. in this case is  $3d_{3/2}$  ( $M_4$ ) and  $3d_{5/2}$  ( $M_5$ ). The energy separation between those levels corresponds to the  $3d$  core hole spin-orbit splitting. The  $M_5$  and  $M_4$  edges are actually excitonic excitations and are always accompanied by the continuum edge-jumps due to transition to non-bonding final states. Each individual group shows multiplet structure that is originated from the intra-atomic interaction between the excited  $4f$  electron and all other  $4f$  electrons, and from the  $3d$  hole created and all  $4f$  electrons, as well as the inter-atomic interaction between the rare earth cation and the neighboring anions. This is characteristic for a certain valency.

The soft XAS measurements were carried out at the National Synchrotron Radiation Research Center (NSRRC) in Taiwan using the DRAGON monochromator [115, 116]. The overall photon energy resolution at the Eu and Gd  $M_{4,5}$  edges was around 0.6 eV. The spectra were recorded using the TEY method.

### 2.3.2 XRR

X-ray reflectivity (XRR) is a powerful method for studying the structure of thin films and multi-layered films. It is very suitable for determining the thickness of poly-crystalline or single crystalline films, and extracting information about the roughness of the surface and the interfaces. A collimated monochromatic x-ray beam, which are generated by an x-ray tube, irradiates the film at very low angles ( $0 < \theta < 4^\circ$ ) with respect to the film plane. The diffracted x-rays are collected in the detector at angle  $2\theta$  with respect to the incident beam after experiencing multiple reflection and refraction at the different interfaces in the film.

A typical XRR profile comprises a maximum intensity at a critical incident angle. This critical angle exists since the refractive index of a material for x-rays is less than unity. Therefore below the critical angle, x-rays experience a total external reflection. The critical incident angle is directly related to the average electron density. Above the critical angle, the XRR profile shows interference fringes, the period of which indicates the total thickness of the film. The decay of XRR intensity is related to the roughness of the surface of the film, and of the interface with the substrate.

Our XRR measurements were accomplished using a Siemens D5000 diffractometer. The x-ray tube contains a water-cooled Cu anode plate, which is used to generate the x-ray beam with a wavelength of 1.54 Å (Cu- $K_\alpha$  radiation). The emission current and the accelerating voltage are normally operated at 10–30 mA and 30–40 kV, respectively. The x-ray beams are collimated by a knife-edge slit system and the  $K_\beta$  photons are filtered out. The sample is located at a 4-circle goniometer which allows one to rotate and translate it precisely. A scintillation counter as a detector is employed to collect the diffracted x-ray beam. To avoid saturation of the diffracted beam, several slits and filter are placed in front of the detector. The sample alignment and measurement is controlled via a computer. The recorded XRR data were further analyzed using a Parrat32 software.

### 2.3.3 SQUID magnetometer

Superconducting quantum interference device (SQUID) magnetometer is the most sensitive instrument, available nowadays, for characterizing the magnetic moment of a sample over a broad range of temperature and applied magnetic field. In principle, a measurement is performed in the

SQUID magnetometer by first moving the sample along the symmetry axis of superconducting detection coils and a magnet. Due to its movement, the magnetic moment of the sample induces an electric current in the detection coils. A change of magnetic flux in these coils changes the persistent current in the detection circuit. Hence, the change of the current in the circuit produces variation of output voltage in the SQUID, which is essentially proportional to the magnetic moment of the sample.

A SQUID magnetometer is built by several main components such as a superconducting magnet, detection coils, the SQUID itself, and a superconducting magnetic shield. The superconducting magnet is a superconducting wire in the form of solenoid which must be kept at liquid helium temperature. It produces uniform magnetic fields that are used to magnetize the sample. The detection coils are basically a single superconducting wire in the form of three counterwound coils configured as a second-order gradiometer. This configuration eliminates spurious signals caused by the fluctuations of the large magnetic field from the superconducting magnet, and also reduces noise from nearby magnetic objects in the surrounding environment. The detection coils are placed at the center of the magnet and connected to the SQUID that is located in a magnetic shield below the magnet. The SQUID is the key component which has a function to convert the induced current to the voltage in an extremely sensitive manner. Its great sensitivity is described by measuring changes of magnetic field associated with one flux quantum. The superconducting magnet shield is used to protect the SQUID sensor from the fluctuations of external magnetic fields nearby the location of the magnetometer, and from the large magnetic field produced by the superconducting magnet.

Our SQUID magnetometer is a magnetic property measurement system (MPMS)–XL7 from Quantum Design. It allows to perform measurements between 1.9 to 400 K with a stability of  $\pm 0.5\%$  and under applied magnetic field up to 7 Tesla with an accuracy of 0.6 Tesla. All samples were measured using the reciprocating sample option (RSO), which has a sensitivity of about  $5 \times 10^{-8}$  EMU. The raw data in the form of a set of sample position-dependent voltage from SQUID sensor are collected using a MPMS MultiVu software. This raw data are then fitted using the iterative regression algorithm to extract the value of the magnetic moment.

## Chapter 3

# Initial stages of EuO growth on YSZ (001)

Results are published in:

R. Sutarto, S. G. Altendorf, B. Coloru, M. Moretti Sala, T. Haupricht, C. F. Chang, Z. Hu, C. Schüßler-Langeheine, N. Hollmann, H. Kierspel, H. H. Hsieh, H.-J. Lin, C. T. Chen, and L. H. Tjeng,  
Physical Review B **79**, 205318 (2009); arXiv:0902.0330.

### 3.1 Introduction

Remarkable in the recent EuO research [17, 44, 50, 52, 53, 55–58, 60–64, 117] is that control of the stoichiometry is nevertheless still a serious issue. Many studies reported that  $\text{Eu}^{3+}$  ions were present in their films and/or that the magnetic moment per formula unit was not close to the expected  $7 \mu_B$  for a  $4f^7$  system. It is not clear in what precision the relative supply rates of oxygen and europium were controlled in these works. We will show below that this control needs not to be precise as long as one is in the so-called Eu-distillation condition during growth.

Also layer-by-layer growth has – to our knowledge – never been mentioned, although epitaxy has been often reported. We therefore set out to do a renewed growth study. We have chosen for yttria-stabilized cubic zirconia (YSZ) as substrate [111, 112]: the lattice constant of YSZ is  $5.142 \text{ \AA}$ , practically identical to the  $5.144 \text{ \AA}$  value for EuO at room temperature [24],

and epitaxy has been reported already [17, 44, 54]. Yet, it was also claimed that control stoichiometry is extremely difficult [17, 54], related to the fact that YSZ acts as a source of oxygen [118] during the MBE growth process.

Below we will study the initial stages of EuO growth on YSZ (100), in particular, we will investigate what the influence is of the oxygen supplied by the YSZ on the chemical state and growth mode of EuO.

## 3.2 Experimental

The EuO films were grown in an ultra-high vacuum MBE facility with a base pressure of  $2 \times 10^{-10}$  mbar, maintained by a cryopump. High purity Eu metal from AMES Laboratory was evaporated from an EPI effusion cell with a BN crucible at temperatures between 460 and 525°C. Proper degassing of the Eu material (mostly hydrogen gas) ensured that during Eu evaporation the pressure was kept below  $3 \times 10^{-9}$  mbar. The Eu deposition rate (4–8 Å/minute) was calibrated using a quartz crystal monitor which was moved to the sample growth position prior and after each growth. Molecular oxygen was supplied through a leak valve, and its pressure ( $4\text{--}16 \times 10^{-8}$  mbar) was monitored using an ion-gauge and a mass-spectrometer. The growth was terminated by closing first the oxygen leak valve and then the Eu shutter after 30 seconds.

As substrates, we used epi-polished single crystals of YSZ from SurfaceNet GmbH. The surface normal of the substrates are all the (001). The lattice constant of YSZ is 5.142 Å, very close to the 5.144 Å value for EuO at room temperature. Prior to growth the substrates were annealed *in-situ* at  $T = 600^\circ\text{C}$  in an oxygen atmosphere of  $5 \times 10^{-7}$  mbar for at least 120 minutes in order to obtain clean and well-ordered substrate surfaces. The substrates were kept at  $T = 400^\circ\text{C}$  during growth.

## 3.3 Results: RHEED and LEED

Figure 3.1 (a) shows the RHEED photograph of the clean and annealed YSZ (001) before growth, and Figure 3.1 (b)–(e) the photographs after 10 minutes of EuO growth. The Eu flux rates were 8.1–8.2 Å/min for (b)–(d) and 4.2–4.3 Å/min for (e)–(f). The oxygen pressure in the chamber was  $4 \times 10^{-8}$  mbar for (b), and  $2 \times 10^{-8}$  mbar for (c) and (e). No oxygen was supplied into the chamber for (d) and (f). The YSZ substrate temperature

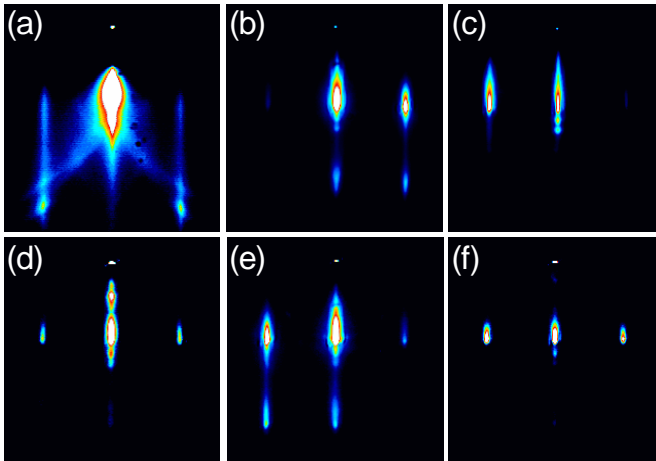


Figure 3.1: RHEED photographs of (a) clean and annealed YSZ (001), (b)–(d) EuO films on YSZ (001) after 10 minutes of growth at  $400^\circ\text{C}$  with  $8.1\text{--}8.2 \text{ \AA}/\text{min}$  Eu flux rates, and (e)–(f) with  $4.2\text{--}4.3 \text{ \AA}/\text{min}$  Eu flux rates. The oxygen pressure in the chamber was  $4 \times 10^{-8}$  mbar for (b), and  $2 \times 10^{-8}$  mbar for (c) and (e). No oxygen was supplied into the chamber for (d) and (f). The RHEED electron energy was 20 keV with the beam incident along the [100] direction.

was kept at  $T = 400^\circ\text{C}$  during growth. The important result is that the general features of the RHEED patterns did not change during growth and that they are very similar to those of the clean YSZ for all Eu and O growth conditions. The distance between the streaks of the EuO films is identical to that of the pure YSZ, confirming that the in-plane lattice constants of EuO and YSZ are very closely matched.

Figure 3.2 shows the time dependence of the RHEED intensity of the specularly reflected beam during the EuO growth. We can clearly observe oscillations which are indicative for a two-dimensional (2D) layer-by-layer or Frank-van der Merwe growth mode. Surprising is that there are only 5–6 oscillations for all deposition conditions as indicated in Fig. 3.2, and that these oscillations even exist in the absence of oxygen in the MBE chamber. It is important to note that the oscillation period does *not* depend on the oxygen pressure  $P_{\text{O}_x}$ , thus also in the case of no oxygen in the chamber. This indicates that the oxygen needed for the formation of EuO must also come from the YSZ substrate. The  $T = 400^\circ\text{C}$  substrate temperature apparently provides sufficient mobility for the oxygen ions to migrate to

Figure 3.2: RHEED intensity oscillations of the specularly reflected electron beam, recorded during the deposition of EuO films on YSZ (001) using oxygen pressures ( $P_{Ox}$ ) and Eu flux rates ( $\Phi_{Eu}$ ) as indicated. The corresponding RHEED photographs after 10 minutes of growth are displayed in Fig. 3.1 (b)–(f).

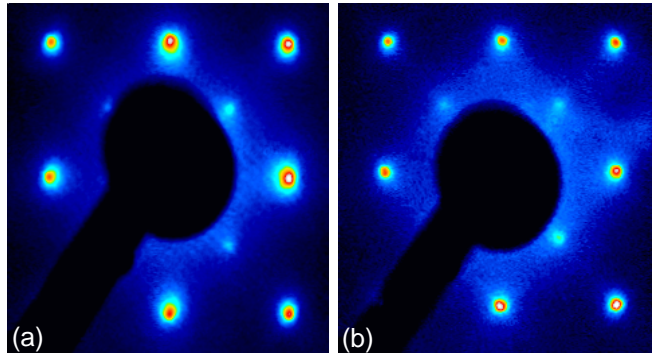
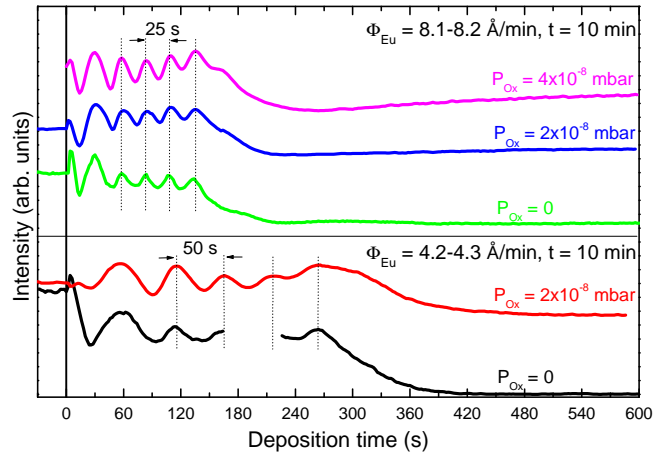


Figure 3.3: LEED photographs of epitaxial EuO films on YSZ substrate, grown for 10 minutes at 400°C in the absence of oxygen in the MBE chamber using (a) a 8.2 Å/min Eu flux rate and recorded at electron beam energy of 215 eV, and (b) a 4.3 Å/min Eu flux rate and recorded at electron beam energy of 213 eV.



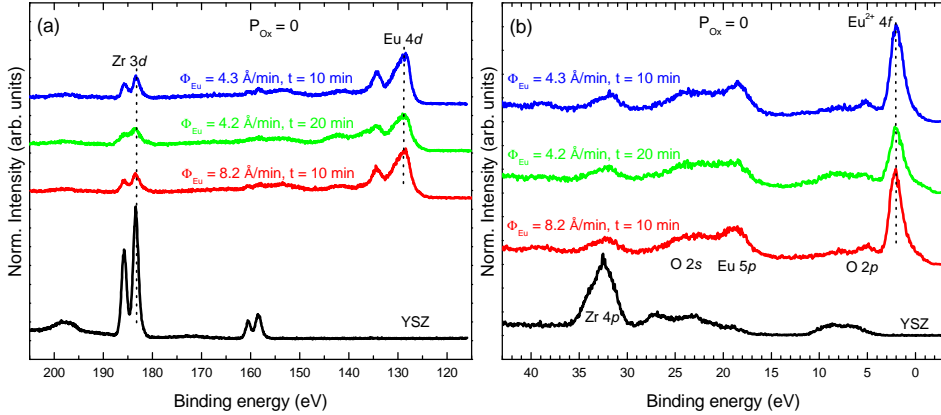


Figure 3.4: (a) Zr 3d – Eu 4d core level XPS spectra and (b) Zr 4p – O 2s – Eu 5p core level and O 2p – Eu 4f valence band XPS spectra of EuO films on YSZ (001), grown at 400°C in the absence of oxygen in the MBE chamber. The spectra were collected at normal emission. From top to bottom: EuO film after 10 minutes of growth using a 4.3 Å/min Eu flux rate, after 20 minutes using 4.2 Å/min, after 10 minutes using 8.2 Å/min, and clean YSZ substrate.

form at least 5 or 6 EuO layers. The oscillation period, which represents a formation of a new atomic single layer, is determined only by the Eu flux rate  $\Phi_{Eu}$ : reducing it by a factor of two, from 8.1–8.2 Å/min to 4.2–4.3 Å/min, doubles the period, from 25 to 50 seconds.

LEED photographs for all these films displayed a good single crystallinity. Figure 3.3 depicts examples for the case of no oxygen in the MBE chamber during growth. Also here we can observe a perfect (001) surface of the EuO rocksalt structure, consistent with the RHEED results. The LEED photographs were taken at electron beam energies of 213–215 eV since lower energies did not provide stable patterns due to charging.

### 3.4 Results: XPS

To investigate the implications of observing only 5–6 oscillations, we also carried out photoemission experiments on those films. Figure 3.4, left panel (a), shows the Zr 3d and Eu 4d core level XPS spectra which were collected at normal emission. It can be clearly seen that the Zr signal is reduced when comparing the clean YSZ (bottom curve – black) with the EuO–

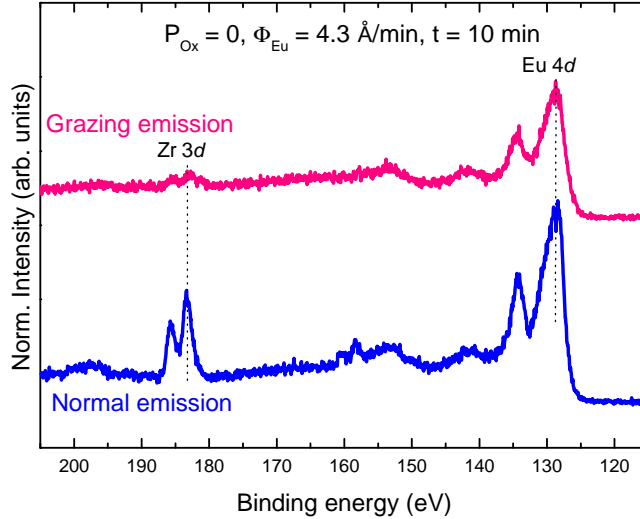


Figure 3.5: Take-off angle dependence of the Zr 3d – Eu 4d core level XPS spectra of a EuO film on YSZ (001). Top: grazing emission, i.e.  $\Theta = 70^\circ$  with respect to the surface normal. Bottom: normal emission. The film was grown at  $400^\circ\text{C}$  for 10 minutes with a  $4.3 \text{ \AA}/\text{min}$  Eu flux rate in the absence of oxygen in the MBE chamber.

covered YSZ (top three curves – blue, green and red). The EuO films here were grown without oxygen in the MBE chamber. Different Eu flux rate and total time of growth are indicated in the figure. It is remarkable that the EuO-covered YSZ spectra have very similar Zr signals, and also equal Eu intensity, despite the fact that the total amount of Eu-exposure is twice as large in the two middle curves (green and red) than in the top one (blue). This indicates that in the absence of oxygen in the MBE chamber, the growth of EuO is limited to 5–6 monolayers only and that the rest of the deposited Eu metal is re-evaporated back into the vacuum (the substrate temperature is  $400^\circ\text{C}$ ). In other words, the sticking coefficient for Eu after the completion of 5–6 monolayers is reduced to zero, suggesting that oxygen transport through EuO is much more difficult than in YSZ.

It is also important to investigate the chemical state of the Eu. Figure 3.4, right panel (b), depicts the O 2p and Eu 4f valence band spectra together with the Zr 4p, O 2s and Eu 5p core levels. The Eu 4f lineshape in all the films is very characteristic for a  $\text{Eu}^{2+}$  system. The multiplet structure typical for  $\text{Eu}^{3+}$  is not visible. One can also observe that the O

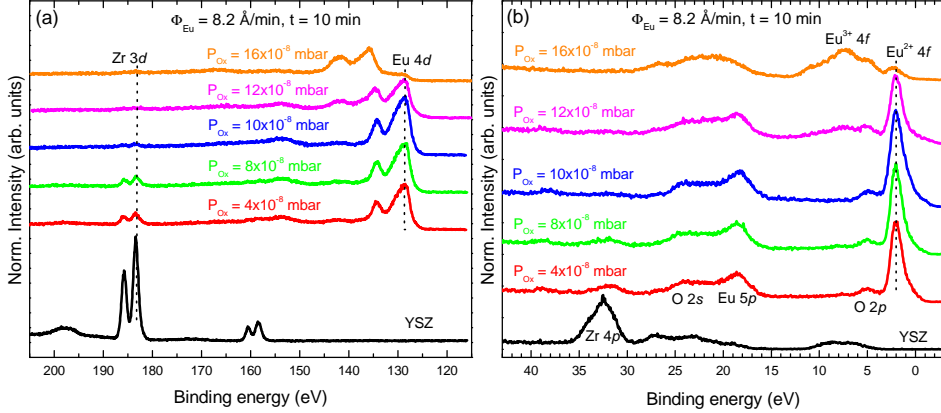


Figure 3.6: (a) Zr 3d – Eu 4d core level XPS spectra and (b) Zr 4p – O 2s – Eu 5p core level and O 2p – Eu 4f valence band XPS spectra of EuO films on YSZ (001), grown at 400°C with a 8.2 Å/min Eu flux rate for 10 minutes. The spectra were collected at normal emission. From top to bottom: EuO films grown under oxygen pressures of 16, 12, 10, 8, and  $4 \times 10^{-8}$  mbar, and clean YSZ substrate.

2p spectrum at 6–10 eV binding energy for YSZ is converted into the O 2p valence band at 4–7 eV typical for EuO [14]. All this demonstrates that only EuO has been formed, free from  $\text{Eu}_2\text{O}_3$  or  $\text{Eu}_3\text{O}_4$  contaminants. This also means that YSZ can only oxidize Eu into the 2+ state, and definitely not into the 3+.

We have also carried out take-off angle dependent XPS experiments on the films. Figure 3.5 shows the Zr 3d and Eu 4d core level XPS spectra of one of the EuO films of Fig. 3.5 (a) collected at grazing emission, i.e.  $\Theta = 70^\circ$  with respect to the surface normal, and at normal emission. One can clearly see that the Eu signal is not significantly reduced but the Zr signal has almost disappeared in the grazing emission geometry. Since grazing emission means more surface sensitivity, this result confirms not only that the EuO film is on top of the YSZ substrate with negligible intermixing of the cations, but also that the film is closed and flat.

Figure 3.6 depicts the Zr 3d and Eu 4d core level spectra (left panel), and the Zr 4p, O 2s and Eu 5p core level together with O 2p and Eu 4f valence band spectra (right panel) of EuO films grown with supply of oxygen in the MBE chamber. Various oxygen pressures have been used as indicated in the figure. The Eu flux rate and the deposition time are identical for these films. One can clearly observe that the Zr 3d signal is getting smaller

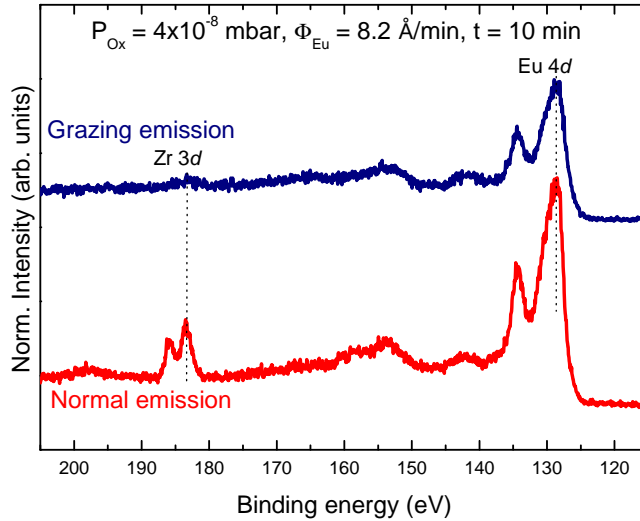


Figure 3.7: Take-off angle dependence of the Zr 3d – Eu 4d core level XPS spectra of a EuO film on YSZ (001). Top: grazing emission, i.e.  $\Theta = 70^\circ$  with respect to the surface normal. Bottom: normal emission. The film was grown at  $400^\circ\text{C}$  under a  $4 \times 10^{-8}$  mbar oxygen pressure and a  $8.2 \text{ \AA}/\text{min}$  Eu flux rate for 10 minutes.

when the oxygen pressure is increased, indicating that the thickness of the EuO film becomes larger. The lineshapes of the Eu 4d and Eu 4f levels are those of divalent Eu for pressures up to  $12 \times 10^{-8}$  mbar. For a pressure of  $12 \times 10^{-8}$  mbar or higher, however, the Eu 4d and Eu 4f spectral shapes start to change and show characteristics which indicate the presence of trivalent Eu. Apparently, for a Eu flux rate of  $8.2 \text{ \AA}/\text{min}$  and substrate temperature of  $400^\circ\text{C}$ ,  $10\text{--}12 \times 10^{-8}$  mbar is the critical oxygen pressure below which EuO films can be made on YSZ (001) free from any  $\text{Eu}_2\text{O}_3$  or  $\text{Eu}_3\text{O}_4$  type of impurity phases.

We have also measured the photoemission spectra of these EuO films under grazing take-off angle conditions. Again, the Eu 4d core level and Eu 4f valence band spectra are all 2+ as long as the oxygen pressures in the MBE chamber are below the critical  $10\text{--}12 \times 10^{-8}$  mbar value. One example is shown in Fig. 3.7, where an oxygen pressure of  $4 \times 10^{-8}$  mbar was used. This figure demonstrates that also the surface region of the films is free from  $\text{Eu}^{3+}$  species. It is interesting to compare the grazing with the normal emission spectra and also with the spectra displayed in Fig. 3.5.

One can clearly see from the Fig. 3.7 that the Zr 3d signal is very much suppressed in grazing emission, even more suppressed than in the grazing emission spectrum of Fig. 3.5. This shows that the EuO films grown with the supply of oxygen in the MBE chamber are thicker, a not so surprising and yet very consistent observation since without oxygen we have found that the EuO film growth is limited to 5–6 monolayers.

### 3.5 Conclusions

The following picture can now be drawn about the initial stages of growth of EuO film on YSZ (001). In case there is no oxygen in the MBE chamber, YSZ is supplying all the oxygen required to form EuO. The film is perfectly free from  $\text{Eu}^{3+}$  species. In case oxygen is present in the MBE chamber, YSZ is supplying only the amount of oxygen that is needed to complete the formation of EuO. This also explains why the growth rate of the first 5–6 monolayers is determined only by the Eu flux rate and is totally independent of the supply of oxygen pressure in the MBE chamber, see Fig. 3.2. Important is that the pressure is kept below the critical value of  $10\text{--}12 \times 10^{-8}$  mbar as we will discuss in more detail in the next chapter.

Based on the comprehensive set of RHEED, LEED, and XPS data, including the RHEED intensity oscillations, we have now demonstrated that EuO thin films can be grown epitaxially in a layer-by-layer fashion with good control of its chemical state. The supply of oxygen from the YSZ does not do any harm, and in fact, it can be utilized as a welcoming method to calibrate the Eu flux rate accurately, e.g. the 8.1–8.2 Å/min from the quartz crystal monitor corresponds to the growth of 1 monolayer EuO per 25 seconds.



## Chapter 4

# Sustained growth of EuO on YSZ (001)

Results are published in:

R. Sutarto, S. G. Altendorf, B. Coloru, M. Moretti Sala, T. Haupricht, C. F. Chang, Z. Hu, C. Schüßler-Langeheine, N. Hollmann, H. Kierspel, H. H. Hsieh, H.-J. Lin, C. T. Chen, and L. H. Tjeng,

Physical Review B **79**, 205318 (2009); arXiv:0902.0330.

### 4.1 Introduction

Having shown that the initial stages of growth of EuO on YSZ (001) can be made quite perfect, we now investigate whether thicker EuO films can be prepared while keeping the epitaxy and especially, the layer-by-layer growth mode. We therefore have grown films for longer deposition times, e.g. between 100 and 200 minutes, using a series of finely intervalled pressures for the oxygen, e.g. 4, 8, 10, 12, and  $16 \times 10^{-8}$  mbar. The Eu flux rates were kept at 8.0–8.3 Å/min. The resulting thickness of the films varies between roughly 300 and 800 Å as will be discussed later.

### 4.2 Results: RHEED and LEED

The RHEED and LEED results are plotted in Fig. 4.1. One can clearly see that excellent epitaxial growth has been achieved for (a) 4, (b) 8, and (c)

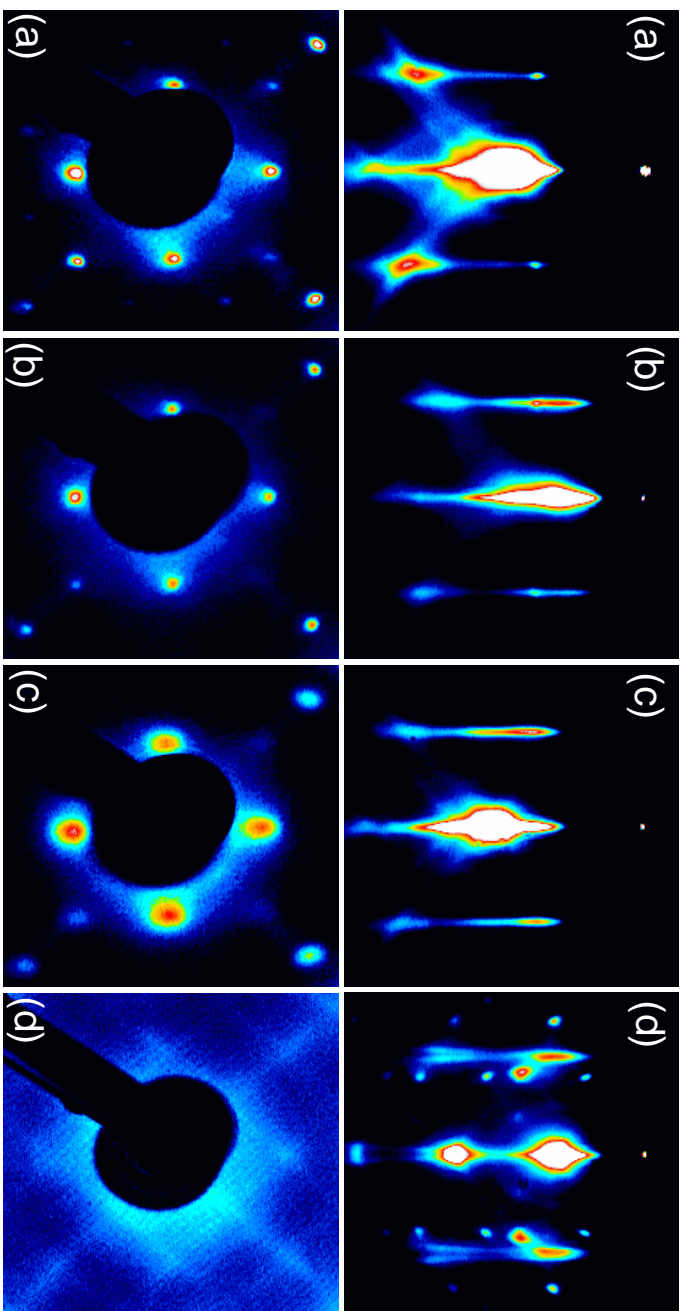


Figure 4.1: Top panels: RHEED photographs of *EuO* films on *YSZ* (001) grown at 400°C with 8.0–8.3 Å/min *Eu* flux rates under oxygen pressures of – from left to right – (a) 4, (b) 8, (c) 10, and (d)  $12 \times 10^{-8}$  mbar. The deposition times were 200, 200, 100, and 100 minutes, respectively. The RHEED electron energy was 20 keV with the beam incident along the [100] direction. Bottom panels: corresponding LEED photographs. The LEED electron energies were 369 eV, 368 eV, 370 eV, and 266 eV, respectively.



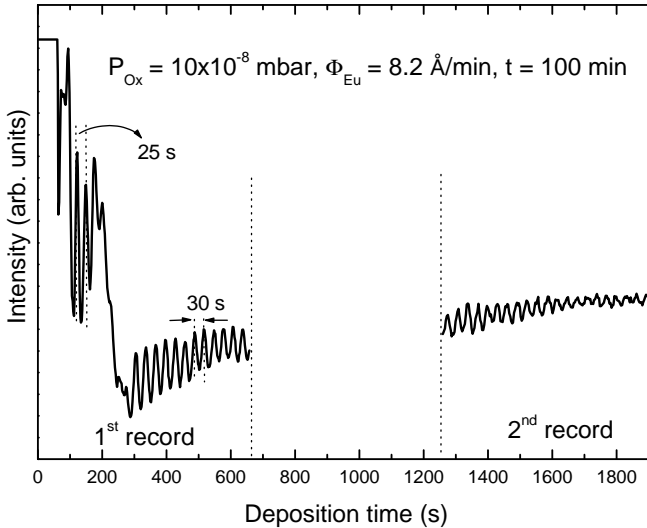


Figure 4.2: RHEED intensity oscillations of the specularly reflected electron beam, recorded during deposition of a EuO film on YSZ (001) grown at 400°C using a  $10 \times 10^{-8}$  mbar oxygen pressure and a  $8.2 \text{ \AA}/\text{min}$  Eu flux rate.

$10 \times 10^{-8}$  mbar oxygen pressures. For  $12 \times 10^{-8}$  mbar (d) or higher pressures, however, the appearance of additional spots in the RHEED indicates that the surface structure starts to change, and the absence of a pattern in the LEED even suggests appreciable surface roughness. The LEED photographs were taken at electron beam energies of 368–370 eV since lower energies did not provide stable patterns due to charging.

As discussed in the previous chapter, the initial 5–6 oscillations of the specular reflected RHEED beam intensity are a unique feature for the initial stages of EuO growth on the YSZ (001). These initial oscillations do always occur, i.e. independent of the oxygen pressure in the MBE chamber, unless the pressure exceeds a critical value above which trivalent Eu species are formed. Remarkable is that no more oscillations can be observed beyond these 5–6 when growing thicker films. This is the case for a wide range of oxygen pressures. There is one exception: for a pressure of  $10 \times 10^{-8}$  mbar, we were able to see further RHEED intensity oscillations. Figure 4.2 shows that the initial 5–6 oscillations are then followed by at least 50 more oscillations. To our knowledge, this is the first time that RHEED intensity oscillations have been observed during the sustained growth of EuO thin

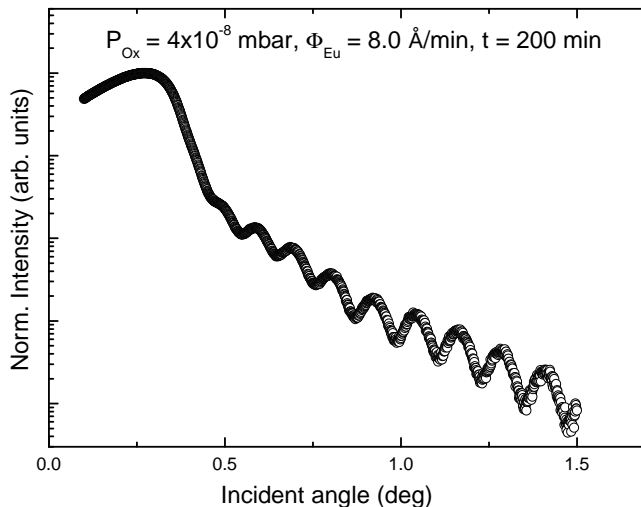


Figure 4.3: X-ray reflectivity (XRR) curve of epitaxial EuO film on YSZ (001) grown for 200 minutes at  $400^{\circ}\text{C}$  using a  $4 \times 10^{-8}$  mbar oxygen pressure and a  $8.0 \text{ \AA}/\text{min}$  Eu flux rate.

films. It demonstrates that a layer-by-layer growth mode for EuO is possible. Interestingly, the oscillation period during the sustained growth is similar and yet a little bit larger than during the initial stages of growth: 30 sec. against 25 sec. Apparently, the oxygen pressure must be close to and yet a little less than the critical value in order to maintain the layer-by-layer growth mode: while the Eu flux determines the growth rate in the initial stages, i.e.  $8.0\text{--}8.2 \text{ \AA}/\text{min}$  Eu flux corresponding to 25 sec. per EuO layer, it is the limited oxygen supply from the MBE environment which dictates the speed during the sustained growth, i.e. to 30 sec. per EuO layer.

### 4.3 Results: thickness

To elucidate further the growth process, we have measured the thickness of the films using *ex-situ* x-ray reflectivity (XRR) measurements. Since EuO deteriorates rapidly under ambient conditions, the films need to be capped. To this end, an aluminum layer with a thickness of  $20\text{--}40 \text{ \AA}$  has been evaporated on top of the EuO. This thickness turns out to be sufficient for the aluminum to be a good protective overlayer as will be discussed later.

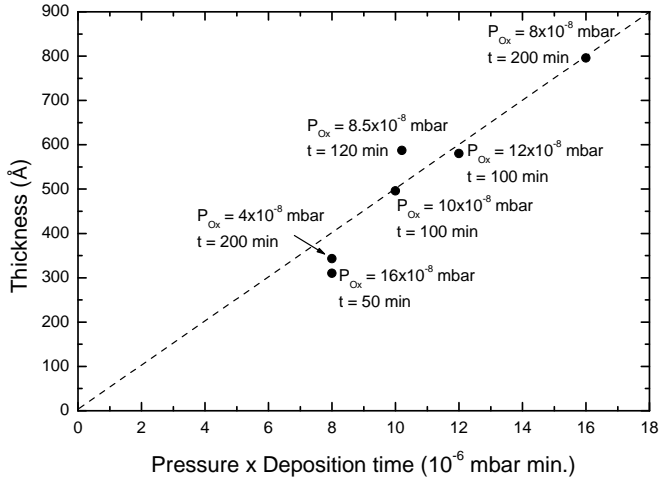


Figure 4.4: EuO film thickness, as determined from XRR measurements, versus the product of oxygen pressure and total deposition time.

Figure 4.3 exhibits the XRR profile of the EuO film which was grown at an oxygen pressure of  $4 \times 10^{-8}$  mbar for 200 minutes. The corresponding RHEED and LEED patterns of the EuO film are displayed in Fig. 4.1 (a). From the period of interference fringes, we deduce that the thickness of the EuO film is about 350 Å.

Thicknesses of the other films are also determined from their XRR profiles. The results are displayed in Fig. 4.4, where we plot the thickness against the product of oxygen pressure and total deposition time. For oxygen pressure up to  $12 \times 10^{-8}$  mbar we can observe a clear and direct linear relationship between them, strongly suggesting that the thickness is determined by the amount of oxygen incorporated. In other words, the growth is limited by the amount of oxygen made available. This in turn means that the Eu flux rate is higher than necessary and that the excess Eu must be re-evaporated into the vacuum. Figure 4.4 essentially confirms the distillation process needed to maintain good control of the stoichiometry as reported in our earlier studies by Steeneken and Tjeng *et al.* [14, 54, 59].

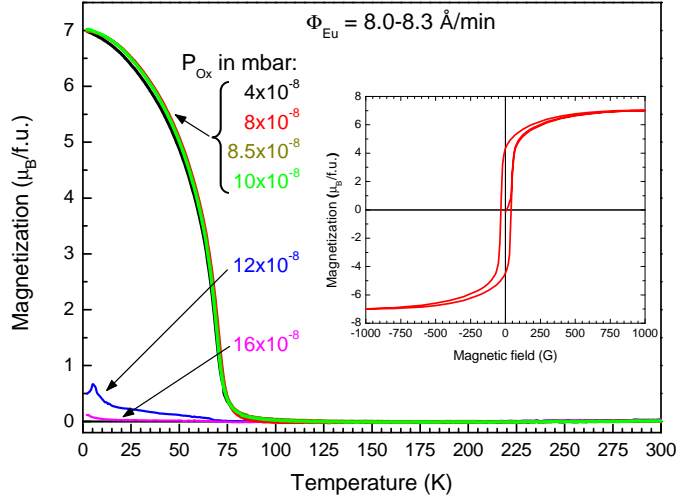


Figure 4.5: Temperature dependence of the magnetization of epitaxial EuO films on YSZ (001) grown at 400°C with 8.0–8.3 Å/min Eu flux rates under various oxygen pressures as indicated. The small magnetization contribution from the substrate has been subtracted. The applied magnetic field was 1000 Gauss. The inset shows the field dependence of the magnetization of epitaxial EuO on YSZ (001) at 5 K. The film was grown at 400°C with a 8.2 Å/min Eu flux rate and a  $8 \times 10^{-8}$  mbar oxygen pressure.

#### 4.4 Results: magnetic properties

We now investigate to what extent the growth conditions affect the magnetic properties of the EuO films using a SQUID magnetometer. The results are shown in Fig. 4.5. The films grown with 4, 8, 8.5, and  $10 \times 10^{-8}$  mbar oxygen pressures all have a Curie temperature of 69 K with a magnetic moment of  $7 \mu_B$  per formula unit as expected for a  $4f^7$  system. The inset shows the field dependence of the magnetization at 5 K for the film grown with a  $8 \times 10^{-8}$  mbar oxygen pressure. Here one can observe a hysteresis behavior with a saturation magnetization of  $7 \mu_B$ . These results are in agreement with the RHEED and LEED results as displayed in Fig. 4.1 (a) to (c), in the sense that the proper ferromagnetic properties are always maintained as long as good epitaxial growth is also achieved. On the other hand, films grown with 12 and  $16 \times 10^{-8}$  mbar have completely lost their ferromagnetic properties. It is remarkable that exceeding the  $10 \times 10^{-8}$  mbar value just a little bit causes such a dramatic change. This very abrupt change is also consistent with the RHEED and LEED results as displayed in Fig. 4.1 (d).

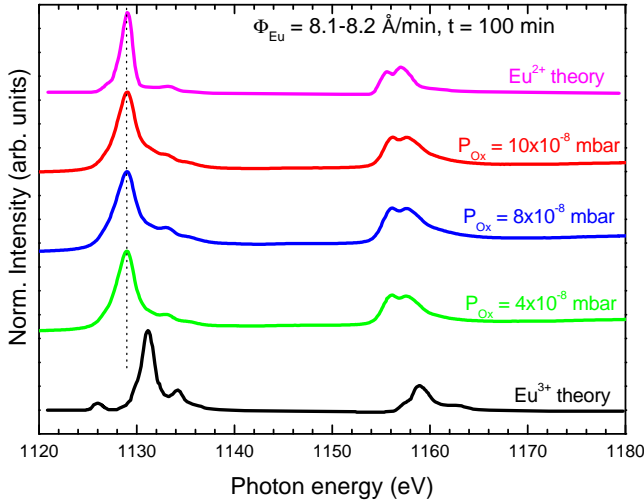


Figure 4.6: Eu  $M_{4,5}$  ( $3d \rightarrow 4f$ ) XAS spectra of EuO films grown epitaxially on YSZ (001) at 400°C with 8.1–8.2 Å/min Eu flux rates under various oxygen pressures as indicated. The films are capped with a 20–40 Å aluminum overlayer. Theoretical spectra of  $\text{Eu}^{2+}$  and  $\text{Eu}^{3+}$  are also shown, retrieved from Ref. [119].

Considerable film roughness start to develop for oxygen pressures higher than  $10 \times 10^{-8}$  mbar. We would like to infer that having only a  $T_C$  about 69 K is not a sufficient characteristic to conclude that the film is homogeneous and stoichiometric. One also needs to establish that the film has a full saturation magnetization of  $7 \mu_B$ . The measurement of the magnetic properties can therefore serve as a critical test for the growth conditions and in particular, the oxygen stoichiometry of the EuO films.

## 4.5 Results: XAS

We have also performed *ex-situ* soft x-ray absorption (XAS) measurements at the Eu  $M_{4,5}$  edges to examine the integrity of the EuO films after capping with the aluminum overlayer. Figure 4.6 depicts the XAS spectra together with the theoretical spectra for  $\text{Eu}^{2+}$  (top) and  $\text{Eu}^{3+}$  (bottom) [119, 120]. It is clear that the Eu spectra are very similar to the theoretical spectrum for  $\text{Eu}^{2+}$ , meaning that the EuO films with 4, 8, and  $10 \times 10^{-8}$  mbar oxygen pressures are completely free from  $\text{Eu}^{3+}$  species. This in turn implies that an aluminum overlayer as thin as 20–40 Å works well to protect the EuO

films against air, contrary to the claims made elsewhere that one needs very thick capping layers [17, 52, 53, 55–58, 60, 62, 63]. We attribute this to the fact that the epitaxial growth of EuO on YSZ (001) yields such a smooth film, so that a very thin aluminum film is sufficient to make a closed capping overlayer.

## 4.6 Conclusions

We conclude that the critical oxygen pressure is around  $10\text{--}12 \times 10^{-8}$  mbar for a 8.0–8.3 Å/min Eu flux rate. Only below this pressure one has the distillation process taking place so that good epitaxial growth can be achieved with the proper stoichiometry and ferromagnetic properties. Apparently, layer-by-layer growth can be obtained only if one is close to, but not exceeding, the critical pressure. Our results form the first evidence that layer-by-layer growth is possible for EuO thin films. The smoothness of the films as well as the complete absence of  $\text{Eu}^{3+}$  impurities form a good starting point for the fabrication of well-defined interfaces with other metals or oxide materials, thereby opening up new opportunities to study or even generate new phenomena related to interface physics.

## Chapter 5

# Gd-doped EuO thin films on YSZ (001)

Most part of this work is reported in:

R. Sutarto, S. G. Altendorf, B. Coloru, M. Moretti Sala, T. Haupricht, C. F. Chang, Z. Hu, C. Schüßler-Langeheine, N. Hollmann, H. Kierspel, J. A. Mydosh, H. H. Hsieh, H.-J. Lin, C. T. Chen, and L. H. Tjeng,  
arXiv:0903.1632; Submitted to Physical Review B.

### 5.1 Introduction

One of the eyes catching properties of EuO is that its Curie temperature of 69 K can be significantly enhanced by electron doping, for instance, by substituting the Eu with trivalent rare earths [22, 23]. Numerous studies have been carried out to characterize and optimize the doping induced magnetic properties. The results, however, vary appreciably. For Gd-doped EuO, for example, the reported optimum  $T_C$  value ranges from 115 K to 148 K [13, 29, 56, 81, 85, 86, 88, 100, 122–124]. and even up to 170 K [59]. The temperature dependence of the magnetization also differs from report to report, most of them showing very little resemblance to a Brillouin function as expected for a Heisenberg system. It is also not clear whether a threshold of the Gd concentration (if any) exists for  $T_C$  starts to increase [13, 56, 85, 86, 122–124]. It was asserted that much of these uncertainties is probably caused by problems with stoichiometry [13, 23]. Indeed, oxygen

deficiencies in Gd-free EuO samples already lead to enhancements of  $T_C$  up to 140–150 K [42, 56, 125]. In fact, it was also suggested that even the actual Gd concentration was not known accurately [23].

In the previous chapters, we have shown that the so-called Eu-distillation assisted molecular beam epitaxy (MBE) procedure is a key ingredient for successfully preparing single crystalline and highly stoichiometric EuO thin films on yttria-stabilized cubic zirconia (YSZ) substrates [126]. Our objective now is to use this procedure as a starting point for obtaining high quality Gd-doped EuO samples. In this study we will investigate in detail whether or not the Eu-distillation process indeed allows for the growth of Gd-doped films free from  $\text{Eu}^{3+}$  contaminants, oxygen vacancies, Eu metal clusters, and  $\text{Gd}_2\text{O}_3$  phases as well. Concerning the growth process itself, we would like to know whether the layer-by-layer growth mode observed for pure EuO on YSZ can also be maintained in the presence of Gd co-deposition. We will use soft x-ray absorption spectroscopy at the Eu and Gd  $M_{4,5}$  edges to obtain a reliable determination of the actual Gd concentration. Our goal is then to establish the magnetic properties of the Gd-doped EuO system using well defined films.

## 5.2 Experimental

The films were prepared by simultaneously depositing Eu and Gd metal on top of YSZ substrates under oxygen atmosphere. High purity Eu metal from AMES Laboratory was sublimated from an EPI effusion cell with a BN crucible at temperatures between 525 and 545°C. Gd metal from Smart-Elements Company was evaporated from a commercial Luxel Corporation RADAK-I Knudsen cell with a molybdenum-insert containing  $\text{Al}_2\text{O}_3$  crucible at temperatures between 1100 and 1350°C. Proper degassing of the Eu and Gd materials ensured that during the film deposition the background pressure was kept below  $5 \times 10^{-9}$  mbar. The Eu deposition rate of 8.1–8.2 Å/minute and the Gd rate of 0.006–0.8 Å/minute were calibrated using a quartz crystal monitor, which was moved to the sample growth position prior and after each growth. Molecular oxygen was supplied through a leak valve, and its pressure ( $4\text{--}10 \times 10^{-8}$  mbar) was monitored using an ion-gauge and a mass-spectrometer. Unless stated otherwise, the substrates were kept at  $T = 400^\circ\text{C}$  during growth and all films were grown for 100 minutes.



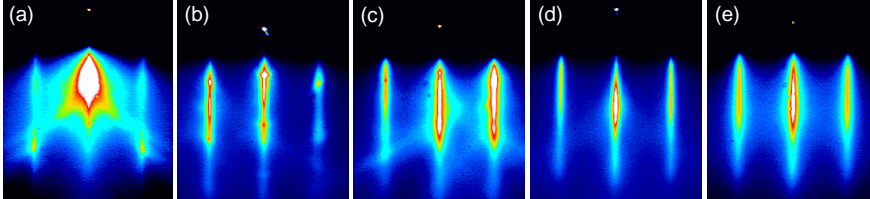


Figure 5.1: RHEED photographs of (a) clean and annealed YSZ (001), and Gd-doped EuO films with Gd concentrations of (b) 0.2%, (c) 2.0%, (d) 7.7%, and (e) 20%. The films were grown for 100 minutes using a 8.1–8.2 Å/min Eu flux rate and a  $8 \times 10^{-8}$  mbar oxygen pressure. The RHEED electron energy was 20 keV with the beam incident along the [100] direction.

The XAS measurements were performed at the Dragon beamline of the National Synchrotron Radiation Research Center (NSRRC) in Taiwan. The spectra were recorded using the total electron yield method and the photon energy resolution at the Eu and Gd  $M_{4,5}$  edges ( $h\nu \approx 1100$ – $1235$  eV) was set at  $\approx 0.6$  eV.

### 5.3 Results: RHEED and LEED

*In-situ* RHEED was employed to monitor the growth quality of Gd-doped EuO thin films. The RHEED photograph of the clean and annealed YSZ (001) before growth is displayed in Fig. 5.1 (a). Figure 5.1 (b)–(e) shows the photographs of Gd-doped EuO films grown with Gd concentrations of (b) 0.2%, (c) 2.0%, (d) 7.7%, and (e) 20%. The films were prepared at 400°C under an oxygen pressure of  $8 \times 10^{-8}$  mbar, a 8.1–8.2 Å/min Eu flux rate, and a Gd flux rate varying between 0.006 and 0.8 Å/min. We will describe later how the actual Gd concentration was determined using XAS at the Eu and Gd  $M_{4,5}$  edges.

The important result is that epitaxial growth of Gd-doped EuO films has been achieved for a wide range of Gd concentrations, even up to 20% doping. The distance between the streaks of the Gd-doped EuO films is always very similar to that of the YSZ substrate, confirming that the in-plane lattice parameters of Gd-doped EuO and YSZ are closely matched. The sharp streaks in the RHEED patterns after 100 minutes of growth can be taken as an indication for the smoothness of the film surface.

We were also looking for RHEED intensity oscillations during the growth

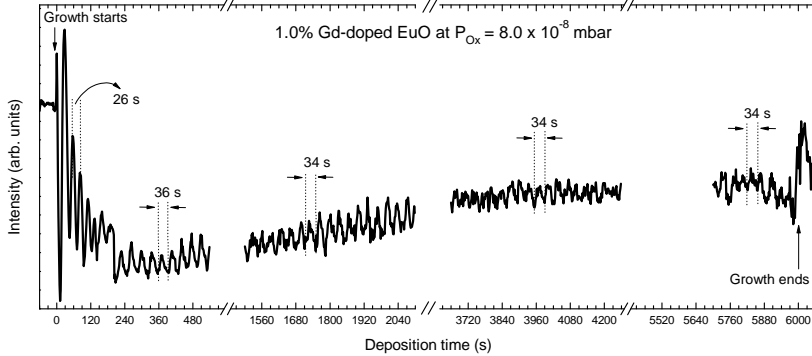


Figure 5.2: RHEED intensity oscillations of the specularly reflected electron beam, detected during deposition of a 1% Gd-doped EuO film on YSZ (001) grown using a 8.1–8.2 Å/min Eu flux rate and a  $8 \times 10^{-8}$  mbar oxygen pressure.

of the Gd-doped EuO films. Such oscillations then indicate the occurrence of a layer-by-layer growth mode, which is important to obtain high quality smooth films. In our previous study on undoped EuO films grown on YSZ (001), we always observed 5–6 oscillations after the start of the growth [126]. The oscillation period is determined by the Eu flux rate, and is independent of the oxygen pressure (provided that it does not exceed a certain critical value above which  $\text{Eu}^{3+}$  could be formed). We found that this is a unique feature for the growth on YSZ, and we were able to attribute this phenomenon to the fact that the YSZ substrate acts as a source for oxygen, which very remarkably, is capable in oxidizing Eu to  $\text{Eu}^{2+}$  but not to  $\text{Eu}^{3+}$  [126]. The period was about 25 seconds for an Eu flux rate of 8.1–8.2 Å/min [126]. Also here for the Gd-doped films we found 5–6 oscillations during the initial stages of growth. The period is approximately 26 seconds when the Gd concentration is very low, and decreases to 22 seconds for films containing 20% Gd, suggesting that the period is roughly inversely proportional to the sum of the Eu and Gd flux rates. These results provide a consistent picture in that the initial stages of growth are governed by the oxygen supply from the YSZ substrate.

With regard to sustained growth, we found in our previous study [126] that long lasting RHEED intensity oscillations can be observed for undoped EuO films on YSZ (001), provided that the oxygen pressure in the MBE chamber is close but not exceeding the critical value above which  $\text{Eu}^{3+}$  ions are formed. The oscillation time is then no longer determined by the

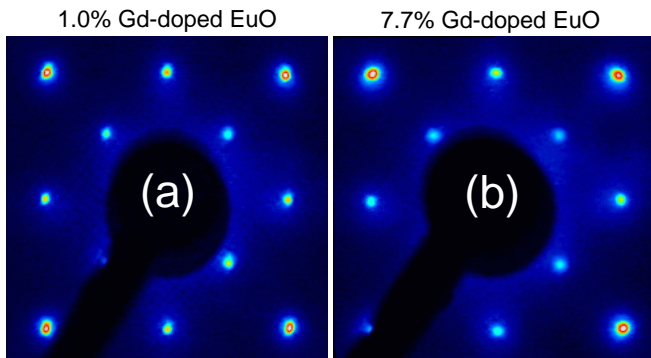


Figure 5.3: LEED photographs of epitaxial Gd-doped EuO films on YSZ (001), grown for 100 minutes using a 8.1–8.2 Å/min Eu flux rate and a  $8 \times 10^{-8}$  mbar oxygen pressure. The Gd concentration is (a) 1.0% and (b) 7.7%. The patterns were recorded at an electron beam energy of approx. 216 eV.

Eu flux rate, but by the oxygen pressure. The growth process therefore involves the re-evaporation of the excess Eu into the vacuum. Also here for the Gd-doped films we make use of this so-called Eu-distillation assisted growth process. Again, using oxygen pressures slightly lower than the critical value, we are able to observe prolonged oscillations. Figure 5.2 shows the time dependence of the RHEED intensity of the specularly reflected beam during the deposition of an 1.0% Gd-doped EuO film. The initial 5–6 oscillations with the periods of 26 seconds are followed by numerous oscillations with a period of about 34.5 seconds for the entire duration of growth. To the best of our knowledge, this is the first experimental evidence, which demonstrates that a Gd-doped EuO film can be prepared epitaxially in a layer-by-layer fashion.

We find those prolonged RHEED intensity oscillations to occur not only for the lowest Gd concentrations but also for concentrations as high as 8%. Although we have not carried out a systematic study, we have indications that the range of oxygen pressures for which the oscillations can be observed is larger for the Gd-doped EuO films than for the pure EuO. So it seems that the presence of Gd does help to stabilize the two-dimensional layer-by-layer growth mode. It is tempting to speculate that perhaps the Gd ions could act as non-mobile nucleation sites since the Gd vapor pressure is extremely low. Those nucleation sites then would increase the step density and make it oscillate for every formation of a new layer.

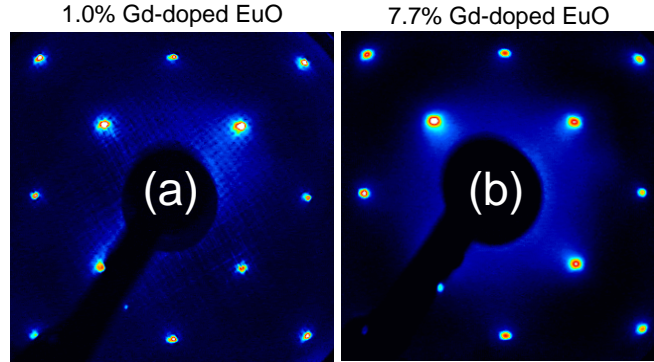


Figure 5.4: same as in Fig. 5.3, but recorded with an electron beam energy of approx. 98 eV.

To check the surface structure, LEED experiments were performed after the growth of Gd-doped EuO films was completed. Figure 5.3 depicts two examples of the LEED photographs of the films with Gd concentration of 7.7% for (a) and 1.0% for (b). The patterns were recorded at an electron beam energy of approximately 216 eV. Since these Gd-doped films are not as insulating as the pure EuO film [126] we were also able to record the LEED patterns at lower energies. Figure 5.4 shows the photographs taken at about 98 eV. Both Figs. 5.3 and 5.4 reveal a perfect (001) surface of the rocksalt structure, fully consistent with the RHEED results.

## 5.4 Results: stoichiometry and Gd concentration

We have investigated the stoichiometry and Gd concentration of the Gd-doped EuO films using *ex-situ* soft XAS measurements. XAS is an element-specific method that is very sensitive to chemical state of a probed ion [119, 120]. Since Gd-doped EuO films are highly susceptible towards further oxidation in air, we have capped the films with a protective aluminum layer of 20–40 Å before taking them out of the MBE system and subsequent transport to the synchrotron facility [126]. Figure 5.5 (a) and (b) depict the Eu and Gd  $M_{4,5}$  ( $3d \rightarrow 4f$ ) XAS spectra of a 11.3% Gd-doped EuO film and an undoped EuO film, respectively. Both films show identical line shapes in their Eu  $M_{4,5}$  spectra. Comparing to the theoretical spectra of  $\text{Eu}^{2+}$  and  $\text{Eu}^{3+}$  [119, 120], we can directly conclude that the experimental

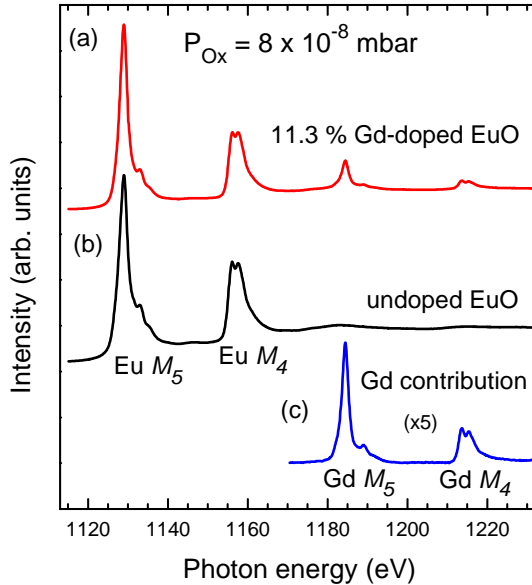


Figure 5.5: Eu and Gd  $M_{4,5}$  ( $3d \rightarrow 4f$ ) XAS spectra of (a) a 11.3% Gd-doped EuO film and (b) an undoped EuO film at 300 K. The net Gd  $M_{4,5}$  contribution (c) is obtained after subtracting the extended x-ray absorption fine structure (EXAFS) of the undoped EuO from the 11.3% Gd-doped EuO spectrum.

spectra represent exclusively  $\text{Eu}^{2+}$  ions. There are no extra peaks or shoulders which otherwise could indicate the presence of  $\text{Eu}^{3+}$  species [16, 64]. We have also carried out XAS measurements on films with other Gd concentrations, and can confirm that our films are completely free from  $\text{Eu}^{3+}$  contaminants.

The Gd  $M_{4,5}$  spectrum has all the characteristics of a  $3d^{10}4f^7 \rightarrow 3d^94f^8$  transition [119, 120, 127], similar to that of the  $\text{Eu}^{2+}$   $M_{4,5}$  one. Thus, having an identical  $4f$  configuration and very similar spectral line shapes as well as photo absorption cross sections, we can use the XAS as a simple and reliable method to deduce the Gd concentration in the films [59]. Figure 5.5 (c) shows the net contribution of the Gd spectrum after subtracting the extended x-ray absorption fine structure (EXAFS) of the undoped EuO (Fig. 5.5 (b)) from the Gd-doped EuO (Fig. 5.5 (a)) spectrum in the Gd  $M_{4,5}$  energy range. The Gd spectrum is displayed with a magnification of a factor of five for clarity. Now one can directly see that the Eu and Gd spectral line shapes are indeed identical. Furthermore, a Gd/Eu ratio is

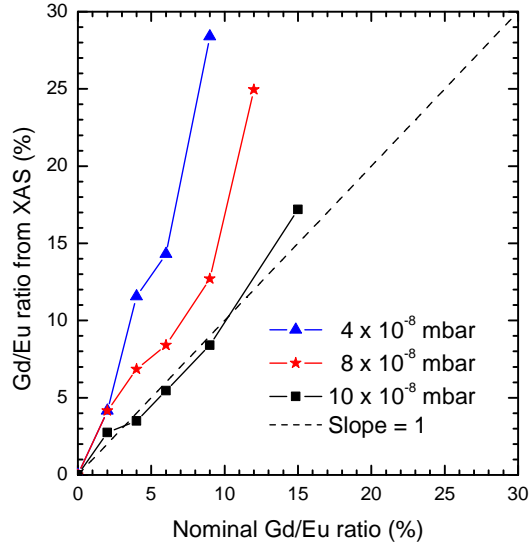


Figure 5.6: (color online) The actual Gd/Eu ratio in Gd-doped EuO films determined from the Eu and Gd  $M_{4,5}$  XAS spectra, versus the nominal ratio given by the relative flux rates. Various oxygen pressures used are indicated and the Eu flux rate was 8.1–8.2 Å/min in all cases. The dash line with slope = 1 serves as guide to the eyes.

obtained by dividing the integrated Gd  $M_5$  and Eu  $M_5$  intensities. In the example of Fig. 5.5, a Gd/Eu ratio of 12.7% is extracted, corresponding to a Gd concentration of  $x = 11.3\%$  in the  $\text{Eu}_{1-x}\text{Gd}_x\text{O}$  chemical formula.

We will now address the important issue concerning the relationship between the actual Gd/Eu ratio in the films as determined from the XAS experiments and the nominal Gd/Eu flux rate ratio during the preparation, as measured by the quartz crystal monitor. We have discovered the actual Gd/Eu ratio can deviate strongly from the nominal one depending on the oxygen pressure used and the flux of Gd deposited. Figure 5.6 displays an overview of our extensive investigation. One can clearly see that the deviation is largest for films grown under low oxygen pressures ( $4 \times 10^{-8}$  mbar) or films having the highest Gd concentrations. Only for films with not too high Gd concentrations and prepared with the oxygen pressure tuned close to the critical value ( $10 \times 10^{-8}$  mbar), one can find that the actual and nominal Gd/Eu ratios match. These observations can be well

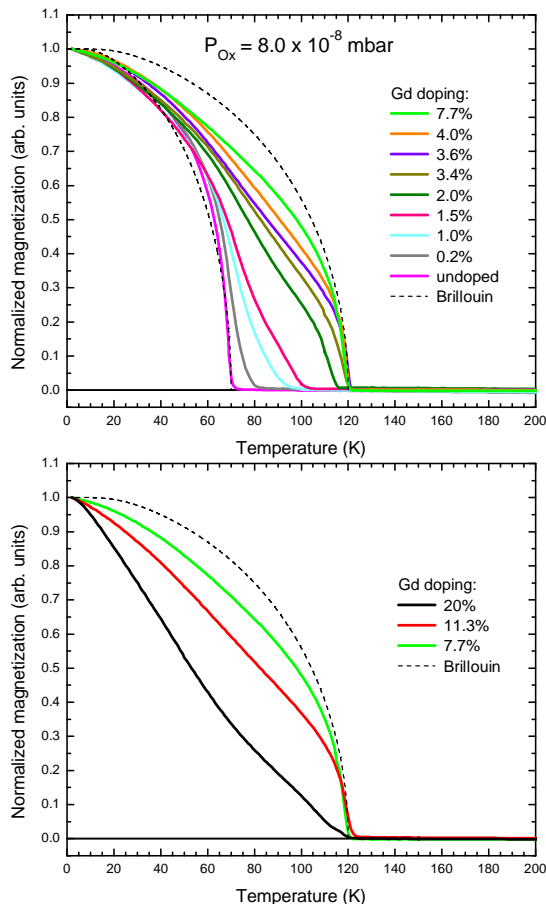


Figure 5.7: Temperature dependence of the normalized magnetization of epitaxial Gd-doped EuO films on YSZ (001) for various Gd concentrations: panel (a) from undoped to 7.7% and panel (b) from 7.7% to 20%. The applied magnetic field was 10 Gauss.

related to the fact that the growth rate is limited by the oxygen pressure. While the Eu can be readily re-evaporated into the vacuum from a substrate at a temperature of  $400^\circ\text{C}$ , the Gd can not since it has a much lower vapor pressure. When the sum of the Gd and Eu fluxes exceeds that of the oxygen, it will be the Eu which has to accommodate for the excess, and thus alter the Gd/Eu ratio.

The oxygen pressure dependence of the actual Gd/Eu ratio can also be

taken as yet another confirmation for the occurrence of the Eu–distillation process [126]. This distillation process is crucial to avoid the accidental formation of oxygen deficiencies during growth. The existence of a critical oxygen pressure and its value can also be directly deduced from the fact that there are data points which lie on the slope = 1 line in Fig. 5.6. Moreover, these data points taken at the critical oxygen pressure demonstrate that the XAS method is very consistent with the flux–rate method for the determination of the Gd/Eu ratio. This in turn adds to the credibility of the XAS as a reliable quantitative method to determine the actual Gd concentration in also other growth conditions.

## 5.5 Results: magnetic properties

After having shown that Gd–doped EuO films can be grown with excellent crystallinity and control of composition, we now focus our attention on their magnetic properties. Figure 5.7 depicts the normalized magnetization of a series of Gd–doped EuO films under an applied magnetic field of 10 Gauss. Starting with the undoped film, we observe that it has a  $T_C$  of 70 K, identical to that of bulk EuO. The shape of the magnetization curve also follows the standard Brillouin function quite well, typical for the undoped bulk EuO [22]. Upon Gd doping, the  $T_C$  increases but the shape of the magnetization curve deviates strongly from the Brillouin function. The  $T_C$  reaches a maximum of 125 K at 6.5% doping. For a Gd concentration of 7.7%, the magnetization curve comes again closer to the Brillouin function. The  $T_C$  is slightly lower, i.e. 121 K. Further doping with Gd up to 20% results in a complete departure of the magnetization curves from the Brillouin function, as displayed in Fig. 5.7 (b), but  $T_C$  remains  $\approx$  120 K.

The  $T_C$  dependence on the Gd concentration is presented in more detail in Fig. 5.8. We note that the Gd concentration is the actual concentration in the film as determined by the XAS method, and not the nominal one based on Gd/Eu flux rate ratios. An important result which can be read from Fig. 5.8 is that only a tiny amount of Gd concentration is needed to enhance directly the  $T_C$ . In this respect we cannot confirm the claim made in the past that the  $T_C$  starts only to increase if the Gd concentration exceeds a threshold value of about 1.2–1.5% [85, 86, 123]. It is not clear why the experimental findings are so different. We can only speculate that in those older studies perhaps not all of the inserted Gd were substitutional



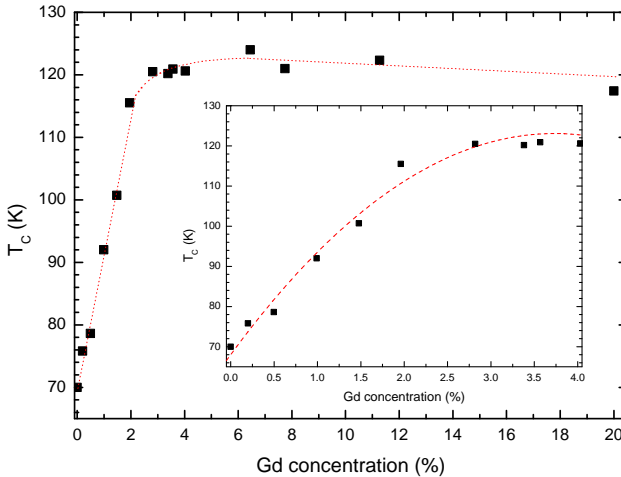


Figure 5.8: The Curie temperature of Gd-doped EuO films on YSZ (001) versus the Gd concentration. The inset is a close-up for the low Gd concentration range. Dashed lines serve as guide to the eyes.

to the Eu and that part of the Gd could be in the form of, for example,  $\text{Gd}_2\text{O}_3$ , and thus not contributing as dopants. In our case we have made the films under Eu-distillation conditions, i.e. shortage of oxygen, so that it is very unlikely that  $\text{Gd}_2\text{O}_3$  can be formed. In fact, some other studies were also not able to detect the existence of such a threshold value [13, 56].

Another important result of Fig. 5.8 is that the maximum value for  $T_C$  with Gd doping is 125 K. We cannot reproduce the higher values (e.g. 130–170 K) reported in the literature [29, 59, 81, 85, 86, 88, 100, 122, 123]. It was inferred that stoichiometry problems could add to an extra increase of  $T_C$  [13, 23]. In this respect it is interesting to note that indeed oxygen deficiencies in Gd-free EuO samples already lead to enhancements of  $T_C$  up to 140–150 K [42, 56, 125]. In our case we can exclude the presence of oxygen vacancies: the samples all were grown under Eu-distillation conditions, and under these conditions we have observed for the pure EuO films that they have the bulk  $T_C$  value of 69 K and that they remain semi-conducting and are in fact extremely insulating down to the lowest temperatures [126].

Our experimental finding of a smooth enhancement of  $T_C$  as a function of Gd concentration is in qualitative agreement with recent mean field theoretical models [89, 90]. Nevertheless, the magnetization curves deviate

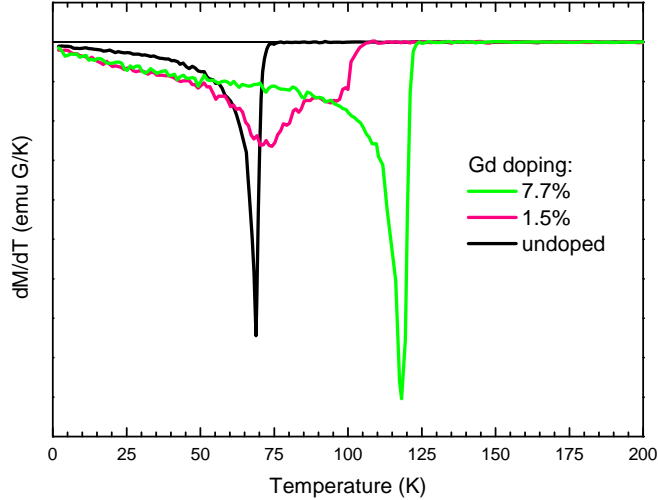


Figure 5.9: Temperature derivative of the magnetization as a function of temperature for the undoped EuO, the 1.5% Gd-doped EuO, and the 7.7% Gd-doped EuO films on YSZ (001).

strongly from the Brillouin function upon doping, with the 7.7% composition showing the smallest deviation. Such deviations could indicate the presence of phase separation. To investigate this phenomenon in more detail, we present in Fig. 5.9 the temperature derivative of the magnetization curves for the undoped EuO film and for the 1.5% and 7.7% Gd-doped EuO films. One can clearly see sharp features at 69 K for the undoped film and at about 120 K for the 7.7% composition, indicating their relative homogeneity and corresponding  $T_C$ 's. For the 1.5% sample, on the other hand, one can clearly distinguish two features. Not only there is a structure at approx. 100 K, marking the  $T_C$  of this film, but there is also a peak at roughly 73 K, which is close to the  $T_C$  of the undoped material.

To complete the investigation of the magnetic properties, we also have measured the magnetic field dependence of the magnetization for the undoped EuO and the 7.7% Gd-doped EuO films at 5 K. The results are shown in Fig. 5.10. One can clearly observe that the samples have very similar hysteresis curves. The remanence magnetization is about  $4.5 \mu_B$  and the coercive field is about 40 G. Moreover, they also showed the saturation magnetization of  $7 \mu_B$  per formula unit as expected for a  $4f^7$  system.

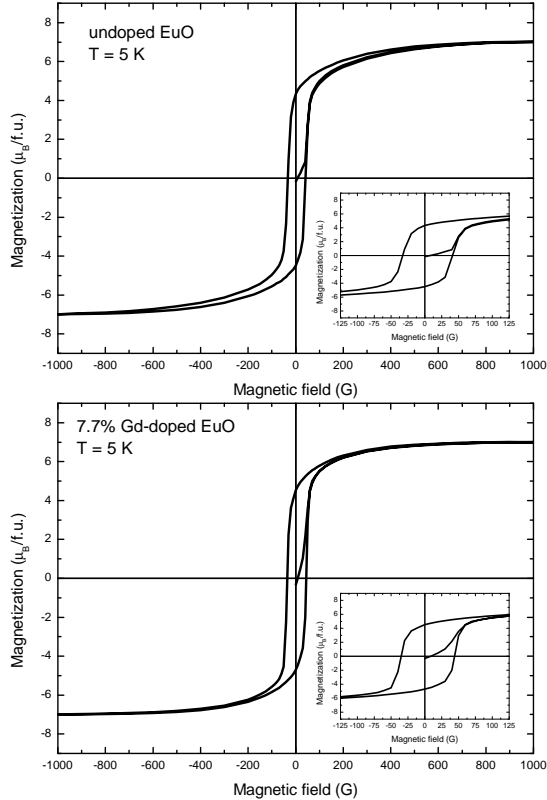


Figure 5.10: The magnetization as a function of the applied magnetic field of (a) the undoped EuO and (b) the 7.7% Gd-doped EuO films on YSZ (001) at 5 K. The insets are enlargement of the corresponding curves at low applied magnetic field.

## 5.6 Discussion

We now can draw the following picture. Substituting Eu by Gd results in doping the material with extra electrons, and these electrons mediate via the double exchange mechanism an enhanced ferromagnetic coupling between neighboring  $4f^7$  ions [22, 23, 89, 90]. Nevertheless, the small impurity potential present at each Gd site binds the extra electron, so that a bound magnetic polaron [22, 23] is formed which becomes practically ferromagnetic at about 125 K. The diameter of these bound polarons could be of order three nearest-neighbors distances. For low doping, they are separated by regions without Gd doping. In going from high to temperatures

lower than 125 K, each polaron starts to polarize the surrounding undoped regions. Lowering the temperature further, there will be a temperature at which a collective ferromagnetic long-range order is created. This is the  $T_C$  of the sample. In the low doping limit, nevertheless, a sizable volume fraction of the material does not feel sufficiently strong the polarizing effect of the paramagnetic clusters, with the result that this fraction starts to order magnetically only when the temperature is close to the  $T_C$  of the undoped material. Apparently, this is the case for the 1.5% film: the temperature derivative of the magnetization reveals not only the  $T_C$  of 100 K, but also another characteristic temperature at 73 K, see Fig. 5.9. For higher doping levels more and more of the volume fraction belongs to the paramagnetic cluster part and/or gets easily polarized by the clusters, with the consequence that the  $T_C$  increases further steadily. At 7.7% concentration one apparently has reached the situation in which the material is magnetically rather homogenous as suggested by the fact that the magnetization curve does not deviate too much from the Brillouin function. For even higher doping levels the magnetization starts to decrease, the cause of which is not clear at the moment.

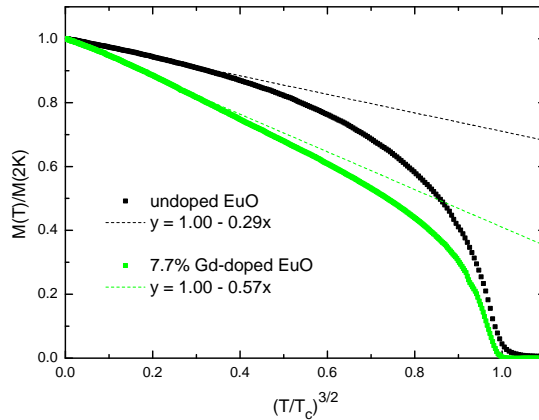


Figure 5.11: The reduced magnetization as a function of  $(T/T_C)^{3/2}$  of the undoped EuO and the 7.7% Gd-doped EuO films. The dashed lines are linear curve fitting to the data using Eq. 1.6.

In order to discuss further the magnetic properties, we have analyzed the magnetization data that of the undoped EuO and the 7.7% Gd-doped EuO films in more detail. The reduced magnetization as a function of  $(T/T_C)^{3/2}$

for both samples is depicted in Fig. 5.11. The low temperature behavior of both samples follows Bloch's  $T^{3/2}$  law based on Eq. 1.6, as indicated by the dashed lines. It suggests that spin waves in both systems are the low-lying elementary excitations. Yet, the spin waves in the Gd-doped EuO are apparently more susceptible to thermal excitations, indicated by a stronger decrease of the magnetization.

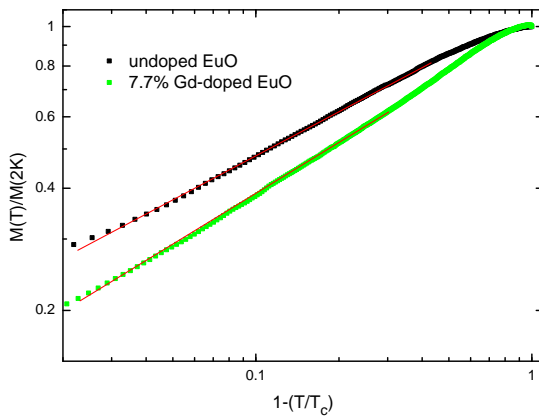


Figure 5.12: The log-log plot of the reduced magnetization as a function of  $1-(T/T_C)$  of the undoped EuO and the 7.7% Gd-doped EuO films. The straight lines are linear curve fitting just below  $T_C$  and the slope corresponds to the critical magnetic exponent  $\beta$ .

We can make an estimation for the value of exchange integral  $J_{ex}$  by linear curve fitting to the data using Eq. 1.6 with  $S = 7/2$  for the  $4f^7$  system,  $Q = 4$  for the rocksalt structure, as well as  $T_C$ s of 70 K and 121 K, respectively, for the undoped EuO and the 7.7% Gd-doped EuO films. In the case of the undoped EuO, the best slope is 0.29. We then obtained  $J_{ex}$  of  $(5.1 \pm 0.1) \times 10^{-5}$  eV, which is in a good agreement with the value of the Eu nearest neighbor exchange integral extracted from inelastic-neutron scattering and specific heat experiments [78–80]. It is noted that the simple expression in Eq. 1.6 only includes the nearest neighbor exchange interaction. Such is obviously not sufficient for the Gd-doped EuO case since an exchange interaction extending to second- and even third-nearest neighbors must also play an important role. Nevertheless, as a rough approach, the slope of 0.57 is derived using the similar expression for the 7.7% Gd-doped EuO. This corresponds to  $J_{ex}$  of  $(5.6 \pm 0.2) \times 10^{-5}$  eV which is rather low as

compared to the  $J$  value deduced from nuclear magnetic resonance (NMR) measurements, i.e.  $\sim 1 \times 10^{-4}$  eV for Gd doping of 2–4% [128]. Yet, it is noted that the latter value includes both the nearest  $J_1$  and next-nearest neighbor exchange integral  $J_2$ .

In addition, we have investigated the magnetization data just below  $T_C$  in terms of a power law,  $M(T) \sim (T_C - T)^\beta$ , where  $\beta$  denotes the critical magnetic exponent with the typical value of 0.36 for the three-dimensional (3D) Heisenberg model. The log-log plot of the reduced magnetization as a function of  $1 - (T/T_C)$  of both films is illustrated in Fig. 5.12. We find  $\beta$  of  $0.35 \pm 0.01$  for the undoped EuO film, which is similar to the bulk EuO [71]. Also for the 7.7% Gd-doped EuO film we extract a similar  $\beta$  value,  $0.37 \pm 0.01$ . This means that Gd-doped EuO behaves also as a Heisenberg ferromagnet.

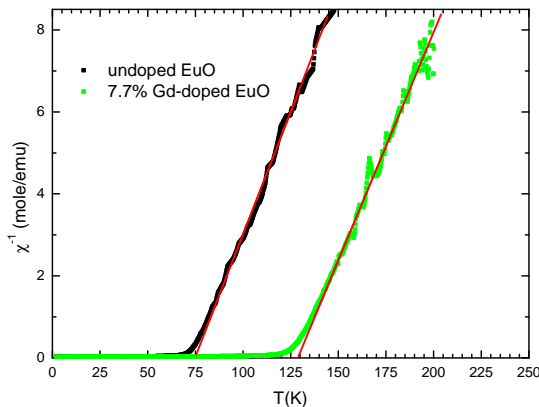


Figure 5.13: The temperature dependence of the reciprocal susceptibility of the undoped EuO and the 7.7% Gd-doped EuO films under an applied field of 1000 Gauss. The straight lines are linear curve fitting to the data using the Curie-Weiss law.

We have also tried to analyze the magnetic properties above  $T_C$ . Figure 5.13 depicts the temperature dependence of the reciprocal susceptibility of both films under an applied magnetic field of 1000 Gauss. The data are fitted using the Curie-Weiss law,  $\chi^{-1} = (T - \Theta)/C$ , where  $\chi$  is the susceptibility,  $\Theta$  the paramagnetic Curie temperature, and  $C = N_A \mu_{\text{eff}}^2 \mu_B^2 / (3k_B)$ , with  $N_A$  denoting the Avogadro number, and  $\mu_{\text{eff}}$  the effective magnetic moment. A paramagnetic Curie temperature  $\Theta$  of 74.3 K and 128.3 K are extracted for the undoped EuO and the Gd-doped EuO films, respectively.

These values are slightly larger, as expected for the critical fluctuations of the Heisenberg model with  $T_C$  of 70 K for the undoped EuO and 121 K for the 7.7% Gd-doped EuO. Also, we have derived the effective magnetic moment  $\mu_{\text{eff}}$  of 8.25 and 8.49  $\mu_B$  for the undoped EuO and the Gd-doped EuO film, respectively. These values are in fairly good agreement with the theoretical value for the  $\text{Eu}^{2+}$  ion with  $^8\text{S}_{7/2}$  ground state,  $\mu_{\text{eff}} = g\mu_B\sqrt{J(J+1)} = 7.94 \mu_B$ . These 4–7% discrepancies are attributed to the fact that the magnetization data collected at high temperature are very small and scattered. It was close to the lowest experimental limit of  $10^{-7}$ – $10^{-8}$  EMU. Also for this susceptibility analysis, the linear background subtraction was required. Its accuracy is reflected by these deviations.

## 5.7 Conclusions

We have succeeded in preparing high-quality Gd-doped EuO samples. The films on YSZ (001) are single-crystalline, and a layer-by-layer epitaxial growth has been observed for the first time. Thanks to the use of the Eu-distillation process during the growth, we were able to obtain films free from  $\text{Eu}^{3+}$  species, oxygen vacancies and  $\text{Gd}_2\text{O}_3$  contaminants. We have provided a reliable determination of the actual Gd concentration in the films by applying soft x-ray absorption spectroscopy at the Gd and Eu  $M_{4,5}$  edges. We found that the Curie temperatures increases steadily as a function of Gd concentration reaching a maximum of 125 K. A threshold behavior was not observed for concentrations as low as 0.2%. Both the undoped and the 7.7% Gd-doped EuO films reveal magnetic properties typical for a 3D,  $S = 7/2$ , Heisenberg ferromagnet. For intermediate Gd concentrations we find indications for phase separation to occur.





## Chapter 6

# SXMCD study on Gd-doped EuO thin films

Part of this work is published in:

H. Ott, S. J. Heise, R. Sutarto, Z. Hu, C. F. Chang, H. H. Hsieh, H.-J. Lin, C. T. Chen and L. H. Tjeng,  
Physical Review B **73**, 094407 (2006).

### 6.1 Introduction

It is well known that the Curie temperature of EuO can be strongly enhanced by Gd doping from 69 to 125 K [22, 56, 129]. However, an open question so far is whether the Gd spins in Gd-doped EuO are coupled to the neighboring Eu spins, and if so, whether they are parallel or antiparallel aligned. Until now little has been reported on this subject in literature. From the few studies carried out in the past it was interpreted from magnetization measurements that the Gd spins may be aligned antiparallel to the Eu spins in Gd-doped EuS films [130] and single crystals [131], as well as in Gd-doped EuO single crystal [13]. Now, with the soft-x-ray absorption spectroscopy (XAS), including the magnetic circular dichroism (XMCD), being developed into maturity over the last 15 years, the issue of spin alignment can be addressed in a straightforward manner.

## 6.2 Experimental

Gd-doped EuO films were grown *in-situ* by means of molecular beam epitaxy (MBE) technique. As substrates we used epi-polished single crystal  $\text{Al}_2\text{O}_3$  (1 $\bar{1}$ 02) and epi-polished MgO (100). The  $\text{Al}_2\text{O}_3$  and MgO substrates were annealed in an oxygen atmosphere of  $1 \times 10^{-7}$  mbar at 600°C and 450°C, respectively. The substrates were kept at  $T = 350^\circ\text{C}$  during growth. The grown samples were transferred to the *in-situ* XAS chamber.

The XAS and XMCD measurements were performed at the Dragon beamline of the National Synchrotron Radiation Research Center (NSRRC) in Taiwan. The spectra were recorded using the total electron yield method. The photon energy resolution at the Eu and Gd  $M_{4,5}$  edges ( $h\nu \approx 1100$ – $1250$  eV) was set at 0.6 eV, and the degree of circular polarization was  $\approx 80\%$ . The samples were measured with an angle of x-ray incidence of  $45^\circ$ . This angle is a compromise between a maximum projection of the photon spin on the sample magnetization (the in-plane easy axis requires grazing incidence) and the avoidance of saturation effects, which may occur if the photon incidence is too grazing, because the photon penetration depth becomes comparable to the electron escape depth. The samples were placed in a magnetic field of about 0.2 T using an *ex-situ* rotatable permanent magnet.

## 6.3 Spin moments of Gd and Eu

Figure 6.1 shows the Eu  $M_{4,5}$  XAS spectra of a 3.7% Gd-doped EuO sample recorded at 20 K using circularly polarized x-rays with the photon spin parallel and antiparallel to the magnetic field direction. We will show below how the actual Gd concentration was determined using XAS at the Eu and Gd  $M_{4,5}$  edges. The spectra look very similar to the theoretical spectra calculated for a  $3d^{10}4f^7 \rightarrow 3d^94f^8$  transition with  $\sigma^+$  and  $\sigma^-$  polarization, respectively [119, 120]. To look more in detail, the two experimental difference spectrum, i.e. the XMCD spectrum, is plotted by the lowest curve and it matches very nicely the theoretical XMCD spectrum for a  $\text{Eu}^{2+}$  ion [120]. The largest XMCD signals can be observed at 1129.1 eV, which is about 0.1 eV higher in energy than the maximum of the  $M_5$  white line, and at 1157.9 eV for the  $M_4$ . The experimental XMCD effect, defined as the difference divided by the sum, becomes 28% and  $-41\%$  for the  $M_5$  and the

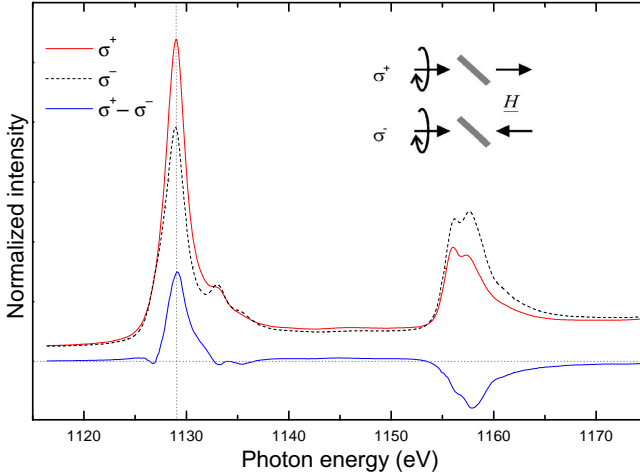


Figure 6.1: Eu  $M_{4,5}$  XAS spectra of a 3.7% Gd-doped EuO sample recorded at 20 K using circularly polarized x-rays applying with the photon spin parallel (solid line) and antiparallel (dashed line) to the magnetic field direction. The lowest curve shows the difference which is called the XMCD spectrum.

$M_4$  white lines, respectively. To extract these numbers, the angle of incidence and the degree of photon polarization have been taken into account. We will describe the XMCD effect at Gd edges later.

Figure 6.2 shows the XAS spectra of (a) Gd-doped and (b) undoped EuO films across the Eu and Gd  $M_{4,5}$  edges taken at 20 K using circularly polarized light. We will look first how the Gd spectrum of Gd-doped EuO film edges looks like. Since the intensity of the Gd contribution is relatively weak, we have magnified the Gd part of the spectra by a factor of ten. The Gd spectrum in Fig. 6.2 (a) has also all the characteristics of a  $3d^{10}4f^7 \rightarrow 3d^9 4f^8$  transition [119, 120, 127]. This is consistent with the fact that the Gd always has the well-known  $4f^7$  configuration. The fact that Eu and Gd have the identical  $4f$  configuration and very similar spectral line shapes facilitates the determination of the Gd concentration in the doped EuO films: we can simply deduce this from the ratio of the height of the main peaks of the Gd and Eu spectra, after subtracting the EXAFS structure of pure EuO in the Gd  $M_{4,5}$  energy range. This is a simple and reliable procedure. For the particular Gd-doped film shown in Fig. 6.2 (a) we find

that the Gd concentration is about 3.7%.

As illustrated in Fig. 6.1 and re-plotted in Fig. 6.2 (a), the XMCD effect in the Eu  $M_{4,5}$  edges can be clearly seen, with the  $M_5$  peak having larger intensity when the light is  $\sigma^+$  (solid line) instead of  $\sigma^-$  (dashed line). The XMCD effect for the Gd edges after magnifying the spectra by a factor of ten are also clearly visible, but we also observe that the background changes with the polarization of the light. We attribute this to the presence of the extended x-ray absorption fine structure (EXAFS) of the Eu edges, which are superimposed on the Gd spectra. As can be seen in Figure 6.2 (b), the Eu EXAFS of undoped EuO indeed carries an XMCD effect in the photon energy region of the Gd edge. To resolve this background problem, we subtract the spectrum of the undoped EuO from that of the Gd-doped EuO. The resulting net Gd contribution to the spectra is shown in Figure 6.2 (c), and the similarity of the Gd spectra with those of Eu is striking. Moreover, the Gd  $M_5$  peak with  $\sigma^+$  light lies also above that with  $\sigma^-$ , i.e. identical to the Eu case. Since the sign of the magnetic circular dichroism (MCD) is related to the orientation of the magnetic ions, this directly means that the Gd and Eu  $4f$  spins are aligned parallel. We have investigated the Gd  $4f$  spin alignment for various doping levels up to 11%, and found in all the cases that the Gd magnetic moment couples ferromagnetically to the magnetic moment of Eu.

## 6.4 Conclusions

Using XMCD measurements, the issue of spin alignment in Gd-doped EuO has been directly resolved. Contrary to the claims made from the past studies, we have determined that the Gd and Eu  $4f$  spins are aligned ferromagnetically for a wide range of Gd doping levels up to 11%.

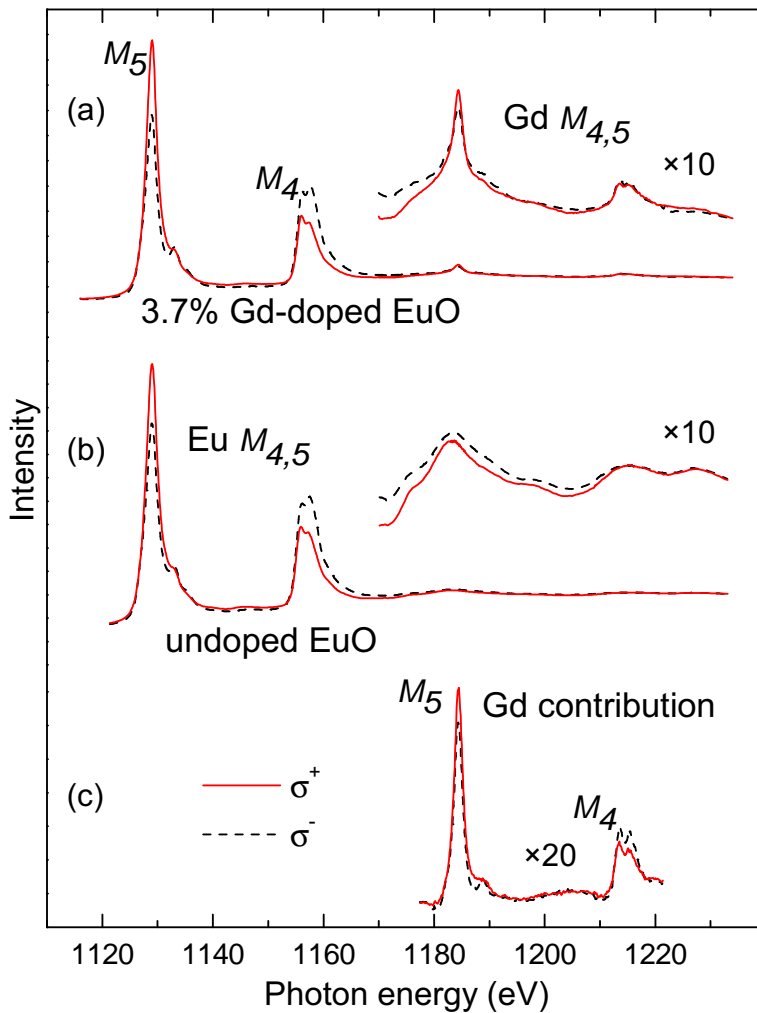


Figure 6.2: Eu and Gd  $M_{4,5}$  XAS spectra of (a) a 3.7% Gd-doped EuO sample and (b) an undoped EuO sample, recorded at 20 K using circularly polarized x-rays with the photon spin parallel and antiparallel to the magnetic field direction. (c) The net Gd  $M_{4,5}$  contribution, obtained by subtracting the EuO spectra from the 3.7% Gd-doped EuO.



## Chapter 7

# Epitaxial growth of EuO on MgO

Results are published in:

R. Sutarto, S. G. Altendorf, B. Coloru, M. Moretti Sala, T. Haupricht, C. F. Chang, Z. Hu, C. Schüßler-Langeheine, N. Hollmann, H. Kierspel, H. H. Hsieh, H.-J. Lin, C. T. Chen, and L. H. Tjeng,  
Physical Review B **79**, 205318 (2009); arXiv:0902.0330.

### 7.1 Introduction

Having understood the growth process of EuO on YSZ (001), and having found the recipe to obtain excellent epitaxial growth of EuO on YSZ (001), we now turn our attention to the preparation of EuO on MgO (001). MgO as a substrate for EuO is interesting since several studies [50, 53, 54, 61] have reported good epitaxial growth despite the very large lattice mismatch of about 20%.

### 7.2 Experimental

The EuO films were grown in an ultra-high vacuum MBE facility with a base pressure of  $2 \times 10^{-10}$  mbar. High purity Eu metal from AMES Laboratory was evaporated from an EPI effusion cell with a BN crucible

at temperatures between 520 and 525°C. The Eu deposition rate of 8.1–8.2 Å/minute was calibrated using a quartz crystal monitor. Molecular oxygen was supplied through a leak valve, and its pressure ( $4\text{--}16 \times 10^{-8}$  mbar) was monitored using an ion-gauge and a mass-spectrometer. The growth was terminated by closing first the oxygen leak valve and then the Eu shutter after 30 seconds. The deposition times were 100 minutes.

As substrates we used cleaved single crystals of MgO from TBL-Kelpin. The surface normal of the substrates are all the (001). The lattice constant of MgO is 4.21 Å[24]. Prior to growth the substrates were annealed *in-situ* at  $T = 600^\circ\text{C}$  in an oxygen atmosphere of  $1 \times 10^{-7}$  mbar for at least 60 minutes in order to obtain clean and well-ordered substrate surfaces. The substrates were kept at  $T = 400^\circ\text{C}$  during growth.

### 7.3 Results

The RHEED and LEED photographs of EuO films grown on MgO using different oxygen pressures are displayed in Fig. 7.1. EuO films with oxygen pressure below  $10 \times 10^{-8}$  mbar all show excellent epitaxial growth. The relationship between the distances of the MgO and EuO streaks is consistent with the ratio of their lattice constants of 1.22. On the other hand, a higher oxygen pressure creates additional spots in the RHEED image and even causes the LEED pattern to disappear. Like for the EuO on YSZ case (see Chapter 4), this indicates that  $10\text{--}12 \times 10^{-8}$  is the critical value for the oxygen pressure above which one no longer gets single-crystalline and stoichiometric EuO.

Our attempts to observe RHEED intensity oscillations of EuO films grown on MgO (001) were yet unsuccessful. The RHEED streaks and specular spot suddenly disappeared right after the deposition of EuO has been initiated. In approximately 30 seconds, new streak lines appear, whose spacing conforms to the EuO lattice parameter. However, the specular spot was never recovered. A more detailed growth study is required to determine the growth process of EuO on MgO (001).

To investigate the quality of these EuO films in terms their magnetic properties, we have performed SQUID measurement for films grown with oxygen pressures of 8, 10, and  $12 \times 10^{-8}$  mbar. The results are shown in Fig. 7.2. Similar to the EuO on YSZ case, the films which were grown below  $10 \times 10^{-8}$  mbar have a Curie temperature of 69 K with a magnetic



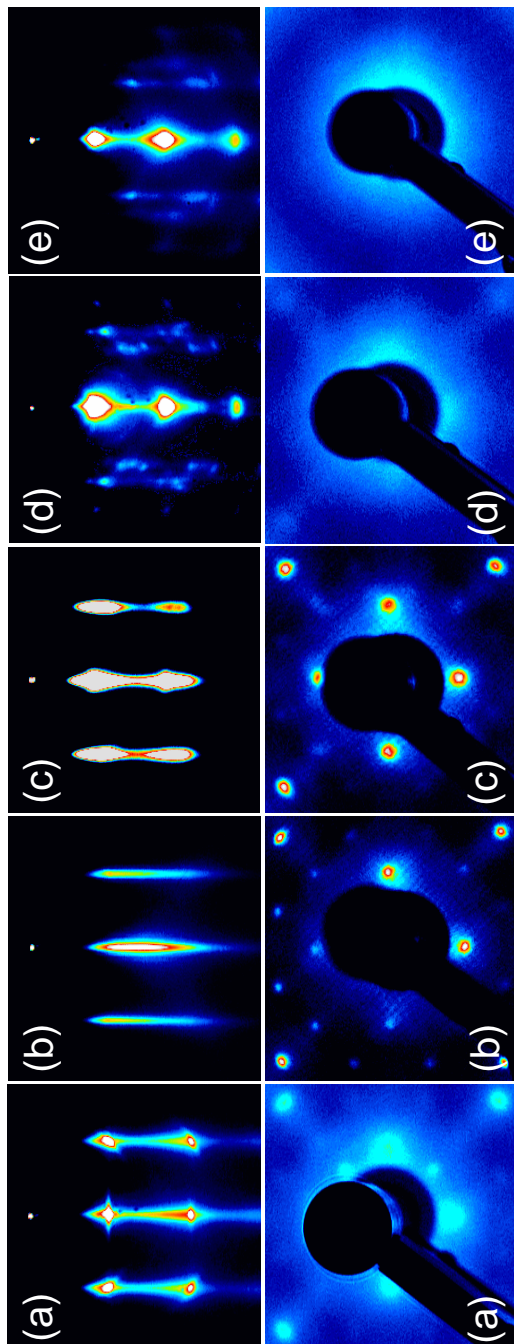


Figure 7.1: Top panels: RHEED photographs of EuO films on MgO (001) grown at 400°C with 8.1–8.2 Å/min Eu flux rates under oxygen pressures of – from left to right – (a) 4, (b) 8, (c) 10, (d) 12, and (e)  $16 \times 10^{-8}$  mbar. The deposition times were all 100 minutes. The RHEED electron energy was 20 keV with the beam incident along the [100] direction. Bottom panels: corresponding LEED photographs. The LEED electron energy was set at 360 eV.

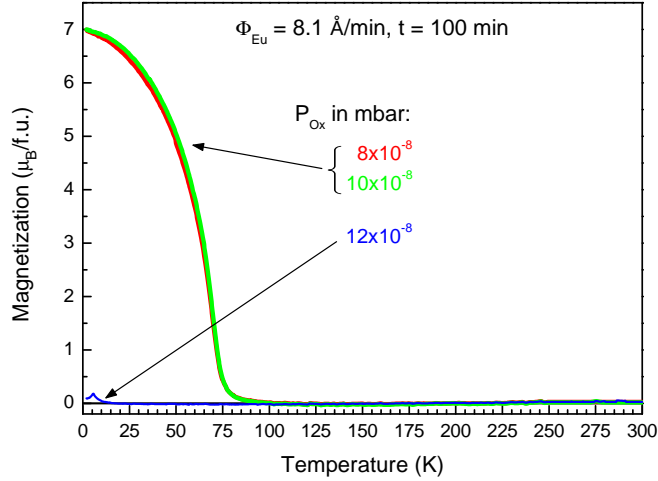


Figure 7.2: Temperature dependence of the magnetization of epitaxial EuO films on MgO (001) grown at 400°C with a 8.1 Å/min Eu flux rate under various oxygen pressures as indicated. The small magnetization contribution from the substrate has been subtracted. The applied magnetic field was 1000 Gauss.

moment close to  $7 \mu_B$  per formula unit. Conversely, the film grown under a higher oxygen pressure has completely lost its ferromagnetic character. The small peak at roughly 5 K indicates the typical anti-ferromagnetic ordering temperature of  $\text{Eu}_3\text{O}_4$  [121], meaning that the dramatic loss of the ferromagnetism for the growth using slightly above the critical oxygen pressure is due to the presence of  $\text{Eu}^{3+}$  species.

## 7.4 Conclusions

Good epitaxial EuO films with the proper ferromagnetic properties were achieved on MgO substrates as long as the Eu-distillation process took place. So far, an evidence for a layer-by-layer EuO growth on MgO has not yet been obtained.

# Summary

Europium oxide (EuO) based materials exhibit a wealth of spectacular phenomena, including half-metallic ferromagnetism, metal-insulator transition, colossal magneto-resistance, large magneto-optical Kerr effect, tunable ferromagnetic ordering temperatures, and large and long-lived photo-induced conductivity. These extraordinary properties make EuO an ideal candidate for implementation in device applications, in particular, for spintronics. Most of the work in the past has been carried out on bulk EuO, but for device applications it is preferred to have the EuO in thin film form. A flurry of studies have therefore emerged in the last decade in order to explore a wide variety of preparation routes and to investigate the properties of the resulting EuO thin films. A recent highlight is the demonstration that doped EuO films can be fabricated on Si and GaN, thereby exhibiting the expected spin-polarized transport effects [17].

Nevertheless, it is still far from a trivial task to prepare EuO thin films with well defined properties. For bulk EuO, it is already known that stoichiometry is the key issue, and that the presence of small amounts of defects or impurities quickly lead to very large deviations of the material properties. In fact, to make bulk EuO to be stoichiometric one needs temperatures as high as 1800°C. It is obvious that such high temperatures are not compatible with device engineering processes. The preparation of thin films must therefore involve much lower temperatures, preferably not higher than 400–500°C. The consequences are very dear. It turned out that many of the recent studies on EuO thin films are suffering from sample quality problems, due to the presence of, e.g., trivalent Eu species ( $\text{Eu}_3\text{O}_4$ ,  $\text{Eu}_2\text{O}_3$ ), oxygen vacancies, or even Eu metal clusters. Controlled doping of the EuO with trivalent rare-earth ions is also not trivial, since most often even the actual doping concentrations were not known. In fact, one could also question in this respect the quality of many of the doped EuO samples used in

the past bulk studies.

The focus of this thesis is on the preparation and the properties of high-quality single-crystalline EuO and Gd-doped EuO thin films. The so-called Eu-distillation-assisted molecular beam epitaxy (MBE) has been employed to achieve full control of the stoichiometry. The films have been epitaxially grown on yttria-stabilized cubic zirconia (YSZ) (001) substrates.

By a systematic variation of the oxygen deposition rates, we have been able to observe sustained oscillations in the intensity of the reflection high-electron energy diffraction (RHEED) pattern during growth. We thus have demonstrated that layer-by-layer growth has been achieved for the first time. We also have confirmed that YSZ indeed supplies oxygen during the initial stages of growth, yet the EuO stoichiometry can still be well maintained.

In the case of Gd-doped EuO films, the presence of Gd even helps to stabilize the layer-by-layer growth mode. It is important to achieve this growth mode, since it enables the preparation of films with very smooth and flat surfaces. This in turn facilitates the capping of the films with a thin Al overlayer in order to protect the films against degradation under ambient conditions. More important, the smoothness of the film will enable the preparation of high quality device structures.

By using *ex-situ* soft x-ray absorption spectroscopy (XAS) at the Eu and Gd  $M_{4,5}$  edges, we have confirmed that the films are completely free from  $\text{Eu}^{3+}$  contaminants, and we were able to determine reliably the actual Gd concentration. This actual Gd concentration could in fact significantly deviate from the nominal Gd/Eu evaporation ratio.

From magnetization and susceptibility measurements, we found the Curie temperature to increase smoothly as a function of doping from 69 K up to a maximum of 125 K, all with a saturation moment of  $7 \mu_B$ . A threshold behavior was not observed for Gd concentrations as low as 0.2 %. Analysis of the data also shows that the Gd-doped EuO films can well be described as a 3D,  $S = 7/2$ , Heisenberg ferromagnet. Using magneto circular dichroic soft x-ray measurements we also proved that the Gd magnetic moments couples ferromagnetically to that of Eu.

# Zusammenfassung

Auf Europiumoxid (EuO) basierende Materialien zeigen eine Vielzahl spektakulärer Phänomene. Zu diesen zählen ein halbmetallischer Ferromagnetismus, ein Metall–Isolator Übergang, ein kolossaler Magnetwiderstand, ein großer magneto–optischer Kerr–Effekt, abstimmbare ferromagnetische Ordnungstemperaturen und eine langlebige licht–induzierte elektrische Leitfähigkeit. Diese außergewöhnlichen Eigenschaften machen EuO zu einem idealen Kandidat für den Einsatz in technischen Anwendungen insbesondere im Bereich der Spintronics. In der Vergangenheit wurden die meisten Studien an Bulk–EuO durchgeführt. Für eine mögliche technische Anwendung wird jedoch EuO in Form von dünnen Filmen bevorzugt. Dies führte zu einer Vielzahl von Studien, die sich mit der Entwicklung von verschiedenen Herstellungsverfahren und der Erforschung der Eigenschaften der daraus resultierenden EuO–Filme beschäftigten. Jüngster Höhepunkt war die Demonstration, dass dotierte EuO–Filme auf Si und GaN hergestellt werden können und dabei die erwarteten spin–polarisierten Transporteffekte zeigen [17].

Dennoch ist es noch immer keine triviale Aufgabe, EuO–Filme mit gut definierten Eigenschaften herzustellen. Für Bulk–EuO ist bereits bekannt, dass die Stöchiometrie eine entscheidende Rolle spielt, und dass schon kleinste Mengen an Defekten oder Verunreinigungen leicht zu gravierenden Änderungen der Materialeigenschaften führen können. Die Herstellung von stöchiometrischem EuO in Bulk–Form erfordert Temperaturen von bis zu 1800°C. Es ist offensichtlich, dass solch hohe Temperaturen nicht mit den gängigen Prozessen zur Herstellung von Bauteilen vereinbar sind. Im Hinblick auf eine mögliche technische Anwendung sollte die Herstellung von dünnen Filmen daher mit deutlich niedrigeren Temperaturen verbunden sein und 400–500°C nicht überschreiten. Es stellte sich heraus, dass in vielen der jüngsten Studien über EuO–Filme eine unzureichende Proben-

qualität, hervorgerufen durch z.B. dreiwertiges Eu ( $\text{Eu}_3\text{O}_4$ ,  $\text{Eu}_2\text{O}_3$ ), Sauerstofffehlstellen oder sogar Eu–Metall–Cluster, die Ergebnisse verfälschte. Ein kontrolliertes Dotieren mit dreiwertigen Seltenerdionen ist ebenfalls nicht trivial, da häufig die tatsächlichen Dotierungskonzentrationen nicht bekannt sind. In dieser Hinsicht kann auch die Qualität der Gd–dotierten EuO–Proben in Bulk–Form älterer Studien hinterfragt werden.

Im Mittelpunkt dieser Doktorarbeit stehen die Herstellung und die Eigenschaften hochqualitativer dünner Filme von einkristallinem reinen und Gd–dotierten EuO. Hierzu wurde die Methode der Molekularstrahlepitaxie (MBE) in Kombination mit einer Eu–Destillation angewendet, um eine vollständige Kontrolle der Stoichiometrie zu ermöglichen. Die Filme wurden epitaktisch auf Yttria–stabilisierten kubischen Zirkonia (YSZ) (001)–Substraten gewachsen. Durch systematische Variation der Sauerstoffdepositionsrate waren wir in der Lage, fortwährende Oszillationen in der Intensität des Beugungsmusters hochenergetischer Elektronen in Reflexion (RHEED) während des Wachstums zu beobachten. Dadurch waren wir zum ersten Mal in der Lage, schichtweises, epitaktisches Wachstum für EuO nachzuweisen. Außerdem konnte bestätigt werden, dass die Stoichiometrie des EuO erhalten werden kann, obwohl YSZ während der initialen Wachstumsphase Sauerstoff absondert.

Bei Gd–dotierten EuO–Filmen helfen die Gd–Atome das Schicht–für–Schicht–Wachstum zu stabilisieren. Dieser Wachstumsmodus ermöglicht die Herstellung von Filmen mit sehr glatten und ebenen Oberflächen, so dass es nur einer dünnen Al–Schutzschicht bedarf, um das EuO vor einer Degradation unter Umgebungsbedingungen zu schützen. Das exzellente Schicht–für–Schicht–Wachstum ermöglicht außerdem die Herstellung qualitativ hochwertiger, mikro–strukturierter Bauteile.

Durch *ex-situ* Absorptionsspektroskopie mit weicher Röntgenstrahlung (XAS) an den Eu und Gd  $M_{4,5}$  Absorptionskanten konnten wir bestätigen, dass die Filme frei von  $\text{Eu}^{3+}$ –Verunreinigungen sind und darüber hinaus zuverlässig die tatsächliche Gd–Konzentration bestimmen. Diese tatsächliche Gd–Konzentration kann signifikant vom nominellen Gd/Eu–Verhältnis, das aus den Verdampfungsrate ermittelt wurde, abweichen.

Magnetisierungs– und Suszeptibilitätsmessungen zeigten ein kontinuierliches Ansteigen der Curie–Temperatur als Funktion der Gd–Dotierung von 69 K bis zu einem Maximalwert von 125 K. Für alle Filme wurde ein Sättigungsmoment von  $7 \mu_B$  bestimmt. Ein Schwellwertverhalten wurde

für Gd-Konzentrationen bis hinunter zu 0,2% nicht beobachtet. Eine Analyse der Daten ergibt zudem, dass die Gd-dotierten EuO-Filme gut als 3D-Heisenberg-Ferromagnete mit  $S = 7/2$  beschrieben werden können. Durch Messung des magnetischen zirkularen Dichroismus mit weicher Röntgenstrahlung (XMCD) konnten wir nachweisen, dass die magnetische Momente der Gd-Atome ferromagnetisch mit den magnetischen Momenten der Eu-Atome koppeln.





# References

- [1] S. A. Wolf, D. D. Awschalom, R. A. Buhrman, J. M. Daughton, S. von Molnár, M. L. Roukes, A. Y. Chtchelkanova, and D. M. Treger, *Science* **294**, 1488 (2001).
- [2] H. Ohno, A. Shen, F. Matsukura, A. Oiwa, A. Endo, S. Katsumoto, and Y. Iye, *Appl. Phys. Lett.* **69**, 363 (1996).
- [3] S. Kuroda, N. Nishizawa, K. Takita, M. Mitome, Y. Bando, K. Osuch, and T. Dietl, *Nat. Mater.* **6**, 440 (2007).
- [4] J.-S. Kang, G. Kim, S. C. Wi, S. S. Lee, S. Choi, S. Cho, S. W. Han, K. H. Kim, H. J. Song, H. J. Shin, A. Sekiyama, S. Kasai, S. Suga, and B. I. Min, *Phys. Rev. Lett.* **94**, 147202 (2005).
- [5] Yu. S. Dedkov, U. Rüdiger, and G. Güntherodt, *Phys. Rev. B* **65**, 064417 (2002).
- [6] B. Nadgorny, I. I. Mazin, M. Osofsky, R. J. Soulen, Jr., P. Brousard, R. M. Stroud, D. J. Singh, V. G. Harris, A. Arsenov, and Ya. Mukovskii, *Phys. Rev. B* **63**, 184433 (2001).
- [7] J. S. Parker, S. M. Watts, P. G. Ivanov, and P. Xiong, *Phys. Rev. Lett.* **88**, 196601 (2002).
- [8] P. Wachter, *Helv. Phys. Acta* **37**, 637 (1964).
- [9] M. J. Freiser, F. Holtzberg, S. Methfessel, G. D. Pettit, M. W. Shafer, and J. C. Suits, *Helv. Phys. Acta* **41**, 832 (1968).
- [10] T. R. McGuire and M. W. Shafer, *J. Appl. Phys.* **35**, 984 (1964).
- [11] G. Busch, P. Junod, and P. Wachter, *Phys. Lett.* **12**, 11 (1964).

- 
- [12] G. Busch and P. Wachter, *Phys. Kondens. Mater.* **5**, 232 (1966).
- [13] J. Schoenes and P. Wachter, *Phys. Rev. B* **9**, 3097 (1974).
- [14] P. G. Steeneken, L. H. Tjeng, I. Elfimov, G. A. Sawatzky, G. Ghiringhelli, N. B. Brookes, and D.-J. Huang, *Phys. Rev. Lett.* **88**, 047201 (2002).
- [15] J. S. Moodera, T. S. Santos, and T. Nagahama, *J. Phys.: Condens. Matter* **19**, 165202 (2007).
- [16] T. S. Santos, J. S. Moodera, K. V. Raman, E. Negusse, J. Holroyd, J. Dvorak, M. Liberati, Y. U. Idzerda, and E. Arenholz, *Phys. Rev. Lett.* **101**, 147201 (2008).
- [17] A. Schmehl, V. Vaithyanathan, A. Herrnberger, S. Thiel, C. Richter, M. Liberati, T. Heeg, M. Röckerath, L. F. Kourkoutis, S. Mühlbauer, P. Böni, D. A. Muller, Y. Barash, J. Schubert, Y. Idzerda, J. Mannhart, and D. G. Schlom, *Nature Mater.* **6**, 882 (2007).
- [18] G. Brauer, *Angew. Chem.* **65**, 261 (1953).
- [19] B. T. Matthias, R. M. Bozort, and J. H. Van Vleck, *Phys. Rev. Lett.* **7**, 160 (1961).
- [20] S. Methfessel and D. C. Mattis, *Encyclopedia of Physics*, edited by S. Flügge and H. P. J. Wijn (1968), vol 18/1, pp. 389–562.
- [21] P. Wachter, *Handbook on the Physics and Chemistry of Rare Earths*, edited by K. A. Gschneidner, Jr. and L. Eyring (1979), chap 19, pp. 507–574.
- [22] A. Mauger and C. Godart, *Phys. Rep.* **141**, 51 (1986).
- [23] N. Tsuda, K. Nasu, A. Yanase, and K. Siratori, *Electronic Conduction in Oxides*, Springer Series in Solid-State Sciences Vol. 94, Springer-Verlag, Berlin (1991), pp. 229–244.
- [24] V. E. Henrich and P. A. Cox, *The Surface Science of Metal Oxides*, Cambridge University Press, Cambridge, England (1994), table 2.2.
- [25] G. F. Guerci and M. W. Shafer, *J. Appl. Phys.* **37**, 1406 (1966).

- 
- [26] T. B. Reed and R. E. Fahey, *J. Crystal Growth* **8**, 337 (1971).
- [27] M. W. Shafer, J. B. Torrance, and T. Penney, *J. Phys. Chem. Solids* **33**, 2251 (1972).
- [28] K. Y. Ahn and J. C. Suits, *IEEE Trans. Magn.* **MAG-3**, 453 (1967).
- [29] K. Y. Ahn and T. R. McGuire, *J. Appl. Phys.* **39**, 5061 (1968).
- [30] K. Y. Ahn and M. W. Shafer, *J. Appl. Phys.* **41**, 1260 (1970).
- [31] K. Lee and J. C. Suits, *J. Appl. Phys.* **41**, 954 (1970).
- [32] K. Y. Ahn, *J. Appl. Phys.* **17**, 347 (1970).
- [33] K. Lee and J. C. Suits, *Phys. Lett.* **34A**, 141 (1971).
- [34] K. Y. Ahn, K. N. Tu, and W. Reuter, *J. Appl. Phys.* **42**, 1769 (1971).
- [35] T. R. McGuire, G. F. Petrich, B. L. Olson, V. L. Moruzzi, and K. Y. Ahn, *J. Appl. Phys.* **42**, 1775 (1971).
- [36] J. C. Suits, K. Lee, H. F. Winters, P. B. P. Phipps, and D. F. Kyser, *J. Appl. Phys.* **42**, 1777 (1971).
- [37] J. C. Suits and K. Lee, *J. Appl. Phys.* **42**, 3258 (1971).
- [38] C. Paparoditis, R. Suryanarayanan, C. Llinares, E. Monteil, and G. Bordure, *Solid State Commun.* **9**, 1871 (1971).
- [39] K. Y. Ahn, *J. Appl. Phys.* **43**, 231 (1972).
- [40] C. Llinares, E. Monteil, G. Bordure, and C. Paparoditis, *Solid State Commun.* **13**, 205 (1973).
- [41] C. Llinares, C. Duchemin, and G. Bordure, *Solid State Commun.* **13**, 785 (1973).
- [42] O. Massenet, Y. Capiomont, and N. V. Dang, *J. Appl. Phys.* **45**, 3593 (1974).
- [43] C. Llinares, L. Gousskov, C. Duchemin, and G. Bordure, *J. Phys. Chem. Solids* **36**, 567 (1975).

- 
- [44] G. M. Roesler, Jr., M. E. Filipkowski, P. R. Broussard, Y. U. Idzerda, M. S. Osofsky, and R. J. Soulen, Jr., in *Superconducting Superlattices and Multilayers*, edited by I. Bozovic, (SPIE Bellingham, 1994), Vol. 2517, pp. 285-290.
- [45] G. M. Roesler, Jr., Y. U. Idzerda, P. R. Broussard, and M. S. Osofsky, *J. Appl. Phys.* **75**, 10 (1994).
- [46] K. Kawaguchi, M. Sohma, *Thin Solid Film* **246**, 1 (1994).
- [47] K. Kawaguchi, M. Sohma, and Y. Oosawa, *J. Magn. Magn. Mater.* **148**, 80 (1995).
- [48] K. Kawaguchi, M. Sohma, and Y. Oosawa, *J. Magn. Magn. Mater.* **156**, 235 (1996).
- [49] T. J. Konno, N. Ogawa, K. Wakoh, K. Sumiyama, and K. Suzuki, *Jpn. J. Appl. Phys.* **35**, 6052 (1996).
- [50] M. Sohma, K. Kawaguchi, and Y. Oosawa, *J. Appl. Phys.* **81**, 5301 (1997).
- [51] T. J. Konno, K. Wakoh, K. Sumiyama, and K. Suzuki, *Jpn. J. Appl. Phys.* **37**, L787 (1998).
- [52] N. Iwata, T. Morishita, and K. Kohn, *J. Phys. Soc. Japan* **69**, 1745 (2000).
- [53] N. Iwata, G. Pindoria, T. Morishita, and K. Kohn, *J. Phys. Soc. Japan* **69**, 230 (2000).
- [54] P. G. Steeneken, *New Light on EuO thin films: Preparation, transport, magnetism, and spectroscopy of a ferromagnetic semiconductor*, Ph.D. thesis, University of Groningen, The Netherlands, 2002.
- [55] J. Lettieri, V. Vaithyanathan, S. K. Eah, J. Stephens, V. Sih, D. D. Awschalom, J. Levy, and D. G. Schlom, *Appl. Phys. Lett.* **83**, 975 (2003).
- [56] T. Matsumoto, K. Yamaguchi, M. Yuri, K. Kawaguchi, N. Koshizaki, and K. Yamada, *J. Phys.: Condens. Matter.* **16**, 6017 (2004).

- 
- [57] J. Holroyd, Y. U. Idzerda, and S. Stadler, *J. Appl. Phys.* **95**, 6571 (2004).
- [58] T. S. Santos and J. S. Moodera, *Phys. Rev. B* **69**, 241203(R) (2004).
- [59] H. Ott, S. J. Heise, R. Sutarto, Z. Hu, C. F. Chang, H. H. Hsieh, H.-J. Lin, C. T. Chen, and L. H. Tjeng, *Phys. Rev. B* **73**, 094407 (2006).
- [60] E. Negusse, J. Holroyd, M. Liberati, J. Dvorak, Y. U. Idzerda, T. S. Santos, J. S. Moodera, and E. Arenholz, *J. Appl. Phys.* **99**, 08E507 (2006).
- [61] H. Lee, J.-Y. Kim, K.-J. Rho, B.-G. Park, and J.-H. Park, *J. Appl. Phys.* **102**, 053903 (2007).
- [62] G. van der Laan, E. Arenholz, A. Schmehl, and D. G. Schlom, *Phys. Rev. Lett.* **100**, 067403 (2008).
- [63] R. W. Ulbricht, A. Schmehl, T. Heeg, J. Schubert, and D. G. Schlom, *Appl. Phys. Lett.* **93**, 102105 (2008).
- [64] R. P. Panguluri, T. S. Santos, E. Negusse, J. Dvorak, Y. Idzerda, J. S. Moodera, and B. Nadgorny, *Phys. Rev. B* **78**, 125307 (2008).
- [65] H. Miyazaki, T. Ito, S Ota, H. J. Im, S. Yagi, M. Kato, K. Soda, and S.-I. Kimura, *Physica B* **403**, 917 (2008).
- [66] S.-I. Kimura, T. Ito, H. Miyazaki, T. Mizuno, T. Iizuka, and T. Takahashi, *Phys. Rev. B* **78**, 052409 (2008).
- [67] E. Arenholz, A. Schmehl, D. G. Schlom, and G. van der Laan, *J. Appl. Phys.* **105**, 07E101 (2009).
- [68] M. Müller, G.-X. Miao, and J. S. Moodera, *J. Appl. Phys.* **105**, 07C917 (2009).
- [69] E. Negusse, J. Dvorak, J. S. Holroyd, M. Liberati, T. S. Santos, J. S. Moodera, E. Arenholz, and Y. U. Idzerda, *J. Appl. Phys.* **105**, 07C930 (2009).
- [70] J. S. Smart, *Effective Field Theories of Magnetism*, W. B. Saunders Company, London (1966), pp. 1–34.

- 
- [71] N. Menyuk, K. Dwight, and T. B. Reed, *Phys. Rev. B.* **3**, 1689 (1971).
- [72] C. C. Huang and J. T. Ho, *Phys. Rev. B.* **11**, 5255 (1975).
- [73] N. W. Ashcroft and N. D. Mermin, *Solid State Physics*, Saunders College Publishing, USA (1976), ch. 31–33.
- [74] C. Kittel, *Introduction to Solid State Physics*, John Wiley & Sons, Inc. (2005), ch. 14–15.
- [75] P. M. Chaikin and T. C. Lubensky, *Principles of Condensed Matter Physics*, Cambridge University Press (2000), table 5.4.2.
- [76] W. Nolting, *Phys. Stat. Sol. (b)* **96**, 11 (1979).
- [77] T. Kasuya, *IBM J. Res. Develop.* **14**, 214 (1970).
- [78] O. W. Dietrich, A. J. Henderson, Jr., and H. Meyer, *Phys. Rev. B.* **12**, 2844 (1975).
- [79] L. Passell, O. W. Dietrich, and J. Als-Nielsen, *Phys. Rev. B.* **14**, 4897 (1976).
- [80] H. A. Mook, *Phys. Rev. Lett.* **46**, 508 (1981).
- [81] M. W. Shafer and T. R. McGuire, *J. Appl. Phys.* **39**, 588 (1968).
- [82] D. DiMarzio, M. Croft, N. Sakai, and M. W. Shafer, *Phys. Rev. B* **35**, 8891 (1987).
- [83] M. M. Abd-Elmeguid and R. D. Taylor, *Phys. Rev. B* **42**, 1048 (1990).
- [84] T. Kasuya and A. Yanase, *Rev. Mod. Phys.* **40**, 684 (1968).
- [85] A. A. Samokhvalov, B. A. Gizhevskii, M. I. Simonova, and N. I. Solin, *Sov. Phys. Solid State* **14**, 230 (1972).
- [86] A. A. Samokhvalov, T. I. Arbuzova, M. I. Simonova, and L. D. Fal'kovskaya, *Sov. Phys. Solid State* **15**, 2459 (1974).
- [87] A. Mauger, *Phys. Stat. Sol. (b)* **84**, 761 (1977).
- [88] A. Mauger, C. Godart, M. Escorne, J. C. Achard, and J. P. Desfours, *J. Phys. (Paris)* **39**, 1125 (1978).

- 
- [89] N. J. C. Ingle and I. S. Elfimov, *Phys. Rev. B* **77**, 121202(R) (2008).
- [90] M. Arnold and J. Kroha, *Phys. Rev. Lett.* **100**, 046404 (2008).
- [91] M. R. Oliver, J. O. Dimmock, A. L. McWhorter, and T. B. Reed, *Phys. Rev. B* **5**, 1078 (1972).
- [92] Y. Shapira, S. Foner, and T. B. Reed, *Phys. Rev. B* **8**, 2299 (1973).
- [93] Y. Shapira, S. Foner, R. L. Aggarwal, and T. B. Reed, *Phys. Rev. B* **8**, 2316 (1973).
- [94] T. Penney, M. W. Shafer, and J. B. Torrance, *Phys. Rev. B* **5**, 3669 (1973).
- [95] J. P. Desfours, J. P. Nadai, M. Averous, and G. Godard, *Solid State Commun.* **20**, 691 (1976).
- [96] M. R. Oliver, J. A. Kafalas, J. O. Dimmock, and T. B. Reed, *Phys. Rev. Lett.* **24**, 1064 (1970).
- [97] J. B. Torrance, M. W. Shafer, and T. R. McGuire, *Phys. Rev. Lett.* **29**, 1168 (1972).
- [98] P. Sinjukow and W. Nolting, *Phys. Rev. B* **68**, 125107 (2003).
- [99] S. von Molnar and M. W. Shafer, *J. Appl. Phys.* **41**, 1093 (1970).
- [100] C. Godart, A. Mauger, J. P. Desfours, and J. C. Achard, *J. Phys. Colloq.* **41**, C5-205 (1980).
- [101] A. A. Samokhvalov, B. A. Gizhevskii, M. I. Simonova, N. M. Chebotayev, and L. D. Fal'kovskaya, *Sov. Phys. Solid State* **24**, 1103 (1982).
- [102] G. Güntherodt, P. Wachter, and D. M. Imboden, *Phys. Kondens. Mater.* **12**, 292 (1971).
- [103] P. Wachter, *Phys. Kondens. Mater.* **8**, 80 (1968).
- [104] H. Wang, J. Schoenes, and E. Kaldis, *Helv. Phys. Acta* **59**, 103 (1986).
- [105] G. Güntherodt, *Phys. Kondens. Mater.* **18**, 37 (1974).

- 
- [106] M. A. Herman and H. Sitter, *Molecular Beam Epitaxy*, Springer Series in Material Science Vol. 7, Second edition, (Springer Verlag, New York 1996).
- [107] M. Ohring, *Materials Science of Thin Films – Deposition and Structure*, Second edition, Academic Press, San Diego, 2002.
- [108] M. Prutton, *Surface Physics*, Oxford University Press, New York, 1983.
- [109] H. von Känel, Lecture notes on *Semiconductor Hetero- and Nanostructures*, Politecnico di Milano, Italy, 2005.
- [110] K. N. Tu, IBM. J. Res. Develop **34**, 868 (1990).
- [111] R. P. Ingel and D. Lewis III, J. Am. Ceram. Soc. **69**, 325 (1986).
- [112] M. Yashima, S. Sasaki, M. Kakihana, Y. Yamaguchi, H. Arashi, and M. Yoshimura, Acta Crystallogr., Sect. B: Struct. Sci **50**, 663 (1994).
- [113] M. Huijben, *Interface Engineering for Oxide Electronics: Tuning electronic properties by atomically controlled growth*, Ph.D. thesis, University of Twente, The Netherlands, 2006.
- [114] P. J. Dobson, B. A. Joyce, J. H. Neave, and J. Zhang, J. Crystal Growth **81**, 1 (1987).
- [115] C. T. Chen, Nucl. Instrum. Methods Phys. Res. **256**, 595 (1987).
- [116] C. T. Chen and F. Sette, Rev. Sci. Instrum. **60**, 1616 (1989).
- [117] S. Mühlbauer, P. Böni, R. Georgii, A. Schmehl, D. G. Schlom, and J. Mannhart, J. Phys.: Condens. Matter. **20**, 104230 (2008).
- [118] N. Q. Minh, J. Am. Ceram. Soc. **76**, 563 (1993).
- [119] B. T. Thole, G. van der Laan, J. C. Fuggle, G. A. Sawatzky, R. C. Karnatak, and J.-M. Esteve, Phys. Rev. B **32**, 5107 (1985).
- [120] J. B. Goedkoop, B. T. Thole, G. van der Laan, G. A. Sawatzky, F. M. F. de Groot, and J. C. Fuggle, Phys. Rev. B **37**, 2086 (1988).
- [121] L. Holmes and M. Schieber, J. Appl. Phys. **37**, 968 (1966).



- 
- [122] F. Meier, P. Zürcher, and E. Kaldis, *Phys. Rev. B* **19**, 4570 (1979).
- [123] A. Mauger, M. Escorne, C. Godart, J. P. Desfours, and J. C. Achard, *J. Phys. Colloq.* **41**, C5-263 (1980).
- [124] H. Rho, C. S. Snow, S. L. Cooper, Z. Fisk, A. Comment, and J.-Ph. Ansernet, *Phys. Rev. Lett.* **88**, 127401 (2002).
- [125] A. A. Samokhvalov, A. F. Gunichev, B. A. Gizhevskii, N. N. Loshkareva, N. M. Chebotaev, and N. A. Viglin, *Sov. Phys. Solid State* **20**, 519 (1978).
- [126] R. Sutarto, S. G. Altendorf, B. Coloru, M. Moretti Sala, T. Haupricht, C. F. Chang, Z. Hu, C. Schüßler-Langeheine, N. Hollmann, H. Kierspel, H. H. Hsieh, H.-J. Lin, C. T. Chen, and L. H. Tjeng, *Phys. Rev. B* **79**, 205318 (2009).
- [127] P. Rudolf, F. Sette, L. H. Tjeng, G. Meigs, and C. T. Chen, *J. Magn. Magn. Mater.* **109**, 109 (1992).
- [128] A. Comment, J.-Ph. Ansernet, C. P. Slichter, H. Rho, C. S. Snow, and S. L. Cooper, *Phys. Rev. B* **72**, 014428 (2005).
- [129] R. Sutarto, S. G. Altendorf, B. Coloru, M. Moretti Sala, T. Haupricht, C. F. Chang, Z. Hu, C. Schüßler-Langeheine, N. Hollmann, H. Kierspel, J. A. Mydosh, H. H. Hsieh, H.-J. Lin, C. T. Chen, and L. H. Tjeng, submitted to *Phys. Rev. B.*, arXiv:0903.1632.
- [130] T. R. McGuire and F. Holtzberg, in: *Magnetism and Magnetic Materials*, AIP Conf. Proc. No. 5, Vol. 2, (AIP, New York, 1971), pp. 855–859.
- [131] E. Bayer and W. Zinn, *Z. Angew. Phys.* **32**, 83 (1971).



# Acknowledgments

*When I am working on a problem, I never think about beauty.  
I think only of how to solve the problem.  
But when I have finished, if the solution is not beautiful,  
I know it is wrong.  
(R. Buckminster Fuller, 1895–1983.)*

Praise to all definite goodness and the ultimate nature of all phenomena!

It is my humbling honor to have been educated and trained in one of the best groups of physics that places an equal stress on both theoretical and experimental aspects. I would like to deeply thank to Prof. L. H. Tjeng (Hao) who was willing to accept me to work on the thin film projects. He has large number of intriguing physical subjects, and EuO thin film is only one part of them. His approaches to guide students toward physics and to help in solving physical and practical problems are always driven by his deep knowledge and concepts, huge curiosity, and broad technical experiences. Although it is always tough to work under his supervision (as most of people warned me), the positive lessons and messages can always be extracted. I am lucky enough to be one of his students. Moreover, I would like to deeply appreciate him for his encouragement toward my future career. Hao, toward your support and kindness during this period, I could only repay by formulating a good wish and pray for your successful and happier life in both physical and mental aspects. Hopefully your activities to help as many people as possible in understanding the nature of physical reality, runs without any obstacles.

I would like to acknowledge Prof. Claus M. Schneider as the referee of this dissertation. I enjoyed so much the discussion with him. Also, I thank to Prof. Rudolf Schierer and Dr. Joachim Hemberger as the chairman and assessor of the dissertation committee, respectively.

A cause needs to meet suitable contributing factors in order to give rise a corresponding result. Dr. Agung Nugroho (Institut Teknologi Bandung, Indonesia) was one of the first contributing factor so that my seed of Ph.D. work came into being. He informed me about the availability of Ph.D. work in Hao's group and kindly pushed me to follow up this opportunity. My special thanks go to you, terima kasih banyak, Pa Agung!

In the beginning months after my arrival in Cologne, I should definitely say many thanks to Frau Beate Neugebauer, Dr. Andrea Severing, and Dr. Bruno Roden who tirelessly help in dealing with all kind of the German bureaucracies.

Now comes to the main contributing factors, namely people who have shared time to work for EuO thin film projects. Many thanks to Stephan J. Heise, Holger Ott, and Chun Fu (Roger) Chang for explanations and discussions about our MBE chambers and thin film growth in general, as well as for working together on many test growth of EuO and iron oxide films. Especially, thank to Roger for the encouragement in my first year.

I would also like to express my gratitude to Tim Haupricht, Simone Altendorf, Marco Moretti (Sala), and Beatrice Coloru. My knowledge and experience are developed when sharing these projects with all of you. Likewise, my thank to Michael Zell, Christian Caspers, Sebastian Standop, and Ernesto Vidal for performing Mini-forschung on EuO projects and to Michel Donker from *Rijksuniversitaet Groningen* for his master project in 2 weeks visit.

Only growing thin film would mean nothing without characterization. My special thanks go to Thomas Koethe and Jan Gegner for their extra care to let the XPS chamber work well. In the same vein, my deep gratitude to Christian Schüßler-Langeheine for his extra effort in making the thin film x-ray diffractometer run again after rather long hibernation and for his teaching on x-ray reflectivity measurement. Not to mention, my appreciation to Zhiwei Hu and NSRRC team for the x-ray absorption measurement in Taiwan and Zhiwei's great help on analyzing the data. I am also grateful to Helena Hartmann, Nils Hollmann, Thomas Lorenz, Susanne Heijligen, and Harald Kierspel for magnetic measurement using VSM and SQUID magnetometer. In this particular case, I would like to say thanks to Prof. Daniil Khomskii and especially to Prof. John Mydosh: I learnt so much from them in analyzing and discussing the magnetization data.

I also enjoyed to share our daily tools and equipments in the home lab-

oratory with people from other thin film projects: Stefan Klein, Rainald Gierth, Jonas Weinen, and Ryan Wicks (University of British Columbia), as well as people from bulk-crystal, x-ray photoemission, and x-ray scattering projects: Dilek Madenci, Thomas Willers, Holger Roth, Sven Binder, Andreas Hendricks, David Regesch, Justina Schlappa, and Marcel Buchholz. Although not really work closely with, I am benefited so much after discussions about other compounds or experimental set-ups with Hua Wu, Maurits Haverkort, Tobias Burnus, Hidenori Fujiwara, and Hsueh-Hung Wu.

The group member has been expanding so much that my occupation at one of the desk in the room 314 was unstable. The reshuffle was unavoidable. The room 317 was my next transit, and after some times it was decayed and I was grounded in the room 315. To all of you sitting in those rooms during those respective time (I guess that I have mentioned all of your names above), many thanks for the conducive environment and pleasant moment. Particularly, thank to the chief of the high-quality joke from Osaka (moshi-moshi greeting for you)!

Due to different projects, my interactions with the rest of group member (old, new members, and guests) are not equally similar. However, I still would like to acknowledge them: Peter Körner, Phillip Hansmann, Christoph Trabant, Yi-Ying Chin, Akfiny Hasdy Aimon (Finy), Alexey Ushakov, Salvatore Altieri (CNR-INFN, Modena), Sergey Streltsov (Institute of Metal Physics, Russia), John Kaunang (ITB, Indonesia), Andrea Grömling, and Anke Riebe. No doubt, I also learnt from any of your activities.

Last but not least, I would express my gratitude to our very helpful technician Lucie Hamdan, electronic workshop people (Herr. Menz, Herr. Lehmann, and Herr. Lüttgen), as well as mechanic workshop people (Herr. Külzer, Herr. Towara, Herr. Hansmann, Herr. Jawadi, and the team). I am sorry for my lousy German language, otherwise I might have grabbed more your experiences. At least, now I recognize one or two Kölsch words from you.

In this occasion, I would also like to deeply thank to the Deutsche Forschungsgemeinschaft (DFG) through Sonderforschungsbereich (SFB) 608 for a financial support of this research. The German translation of the summary of this dissertation was complete by the great effort from Simone, Christian, Tim, and David. Finally, this simple work could not be accom-

plished without a wholehearted support from Rinpoche (France), dr. Ali Tjoa and his family (the Netherlands), group members of Institut Guepele and Ganden Ling in France and their affiliations in the Netherlands, Indonesia, Hongkong, and Malaysia, as well as from an Indonesian family who supplied the very first information about living in Cologne, Paula Rudati, Ph.D. and her family.

My last special thanks are conveyed to my wife Henny and the whole family in Indonesia and United States. Dear Henny, thank you for always caring and accompanying me throughout this time.

May whatever positive energy generated by this activity, contribute to a joyful state in the entire world.

*... These days, it is truism to say that education is vital,  
but it is important to remind ourselves of the larger purpose of education.  
After all, what good is the accumulation of knowledge  
if it does not lead to a happier life?  
(The Middle Way, the Dalai Lama, 2009.)*

# Publications

*Epitaxy, stoichiometry, and magnetic properties of Gd-doped EuO films on YSZ (001)*

R. Sutarto, S. G. Altendorf, B. Coloru, M. Moretti Sala, T. Haupricht, C. F. Chang, Z. Hu, C. Schüßler-Langeheine, N. Hollmann, H. Kierspel, J. A. Mydosh, H. H. Hsieh, H.-J. Lin, C. T. Chen, and L. H. Tjeng,  
Submitted to Physical Review B; arXiv:0903.1632.

*Epitaxial and layer-by-layer growth of EuO thin films on yttria-stabilized cubic zirconia (001) using MBE distillation*

R. Sutarto, S. G. Altendorf, B. Coloru, M. Moretti Sala, T. Haupricht, C. F. Chang, Z. Hu, C. Schüßler-Langeheine, N. Hollmann, H. Kierspel, H. H. Hsieh, H.-J. Lin, C. T. Chen, and L. H. Tjeng,  
Physical Review B **79**, 205318 (2009); arXiv:0902.0330.

*Magnetization-induced second-harmonic generation in epitaxial magnetite thin films Fe<sub>3</sub>O<sub>4</sub>/MgO(100)*

A. A. Rzhnevsky, B. B. Krichevstov, A. D. Rata, C. F. Chang, R. Sutarto, L. H. Tjeng, and C. M. Schneider,  
Journal of Applied Physics **99**, 08J702 (2006)

*Soft x-ray magnetic circular dichroism study on Gd-doped EuO thin films*

H. Ott, S. J. Heise, R. Sutarto, Z. Hu, C. F. Chang, H. H. Hsieh, H.-J. Lin, C. T. Chen and L. H. Tjeng,  
Physical Review B **73**, 094407 (2006)





# Erklärung

Ich versichere, dass ich die von mir vorgelegte Dissertation selbständig angefertigt, die benutzten Quellen und Hilfsmittel vollständig angegeben und die Stellen der Arbeit – einschließlich Tabellen, Karten und Abbildungen –, die anderen Werken im Wortlaut oder dem Sinn nach entnommen sind, in jedem Einzelfall als Entlehnung kenntlich gemacht habe; dass diese Dissertation noch keiner anderen Fakultät oder Universität zur Prüfung vorgelegen hat; dass sie – abgesehen von unten angegebenen Teilpublikationen – noch nicht veröffentlicht worden ist sowie, dass ich eine solche Veröffentlichung vor Abschluss des Promotionsverfahrens nicht vornehmen werde. Die Bestimmungen dieser Promotionsordnung sind mir bekannt. Die von mir vorgelegte Dissertation ist von Prof. Dr. L. H. Tjeng betreut worden.

Ronny Sutarto



# Curriculum vitae

- 3 February 1977 Born in Bandung – Indonesia
- 1983–1989 Elementary School "SD Bina Bakti" in Bandung
- 1989–1992 Junior High School "SMP Santo Aloysius" in Bandung
- 1992–1995 Senior High School "SMA Santo Aloysius" in Bandung
- 1995–2000 Institut Teknologi Bandung – Indonesia  
Bachelor thesis in the group of Prof. Tjia May On
- 2001–2003 *Rijksuniversitaet* Groningen – the Netherlands  
Master thesis in the group of Prof. Paul W. M. Blom
- 2004–2009 II. Physikalisches Institut, Universität zu Köln – Germany  
Ph.D. study in the group of Prof. Liu Hao Tjeng